

Washington University in St. Louis
Washington University Open Scholarship

All Theses and Dissertations (ETDs)

Summer 9-1-2014

Absolute Quantitation for MR Molecular Imaging of Angiogenesis

Matthew John Goette

Washington University in St. Louis

Follow this and additional works at: <https://openscholarship.wustl.edu/etd>

Recommended Citation

Goette, Matthew John, "Absolute Quantitation for MR Molecular Imaging of Angiogenesis" (2014). *All Theses and Dissertations (ETDs)*. 1304.

<https://openscholarship.wustl.edu/etd/1304>

This Dissertation is brought to you for free and open access by Washington University Open Scholarship. It has been accepted for inclusion in All Theses and Dissertations (ETDs) by an authorized administrator of Washington University Open Scholarship. For more information, please contact digital@wumail.wustl.edu.

WASHINGTON UNIVERSITY IN ST. LOUIS

School of Engineering & Applied Science

Department of Biomedical Engineering

Dissertation Examination Committee:

Samuel Wickline, Chair

Joseph Ackerman

Mark Anastasio

Shelton Caruthers

Frank Yin

Absolute Quantitation for MR Molecular Imaging of Angiogenesis

by

Matthew John Goette

A dissertation presented to the
Graduate School of Arts and Sciences
of Washington University in
partial fulfillment of the
requirements for the degree
of Doctor of Philosophy

August 2014

St. Louis, Missouri

© 2014, Matthew John Goette

Table of Contents

List of Figures	vii
List of Tables	xiv
Acknowledgments	xv
Abstract of the Dissertation	xviii
1 Introduction	1
1.1 Quantitative Magnetic Resonance Molecular and Functional Imaging	1
1.1.1 Proton MR Molecular and Functional Imaging	3
1.1.2 Non-proton MR Molecular and Functional Imaging	5
1.2 Perfluorocarbon Nanoparticle Emulsion Contrast Agents	7
1.2.1 ¹ H MR Molecular Imaging of Targeted PFC NP	9
1.2.2 ¹⁹ F MR Molecular Imaging of Targeted PFC NP	12
1.2.3 Cell Tracking using ¹⁹ F MRI of PFC NP	14
1.3 Challenges of Quantitative ¹⁹ F MR Molecular Imaging	15
1.3.1 Signal-to-Noise Ratio	16
1.3.2 Quantitative Imaging Artifacts	17
1.3.3 Chemical Shift and J-coupling	18
1.4 Dissertation Objective, Significance, and Organization	19
1.4.1 Objective	19
1.4.2 Significance and Innovation	20
1.4.3 Organization	21
1.5 References	24

2 Principles of ^{19}F NMR Physics and Image Acquisition with $^{19}\text{F}/^1\text{H}$ Dual-Tuned RF Coils	36
.....	36
2.1 Principles of ^{19}F NMR Physics	36
2.1.1 NMR Background	36
2.1.2 J-coupling in ^{19}F MR of PFC NP	41
2.2 Image Acquisition with $^{19}\text{F}/^1\text{H}$ Dual-Tuned RF Coils	43
2.2.1 Introduction	43
2.2.2 Methods	45
2.2.2.1 Coupled Resonator Model	46
2.2.2.2 Impedance Matching	47
2.2.2.3 Construction of Volume Coils for $^{19}\text{F}/^1\text{H}$ MRI at 3.0 T	48
2.2.2.4 Bench Test of Electromagnetic Performance	50
2.2.2.5 Phantom and <i>In Vivo</i> Imaging	50
2.2.3 Results	51
2.2.3.1 Bench Tests	52
2.2.3.2 Phantom and <i>In Vivo</i> $^{19}\text{F}/^1\text{H}$ Imaging	53
2.2.4 Discussion	55
2.2.5 Conclusion	56
2.3 Acknowledgements	56
2.4 References	56
3 Balanced UTE-SSFP for ^{19}F MR Imaging of Complex Spectra	61
3.1 Introduction	61

3.2 Methods	64
3.2.1 Pulse Sequence Design	64
3.2.2 Phantom Imaging Experiments	67
3.2.3 Sensitivity Comparisons	68
3.2.4 <i>In Vivo</i> Imaging Experiment	69
3.3 Results	70
3.4 Discussion	74
3.5 Conclusion	80
3.6 Acknowledgements	81
3.7 References	81
4. Improved Quantitative ¹⁹F MR Molecular Imaging with Flip Angle Calibration and B₁-Mapping Compensation	89
4.1. Introduction	89
4.2. Methods	91
4.2.1. Magnetic Resonance Spectroscopy	91
4.2.2. PFC NP Formulation and Phantom Setup	92
4.2.3. Power Setting Optimization and Flip Angle Calibration	93
4.2.4. MRI Phantom Setup and B ₁ -Mapping Compensation	94
4.2.5. <i>In Vivo</i> ¹⁹ F MRI Experiment	95
4.2.6. Statistical Analysis	96
4.3. Results	97
4.3.1. Power Setting Optimization and Flip Angle Calibration	97

4.3.2. B ₁ -Mapping Compensation in Phantom Experiments	99
4.3.3. <i>In Vivo</i> ¹⁹ F MRI Experiment	101
4.4. Discussion	102
4.5. Conclusion	104
4.6. Acknowledgements	104
4.7. References	105
5. Novel <i>In Vivo</i> Applications of ¹⁹F MR Molecular Imaging at 3T	110
5.1. Imaging Renal Perfusion in Acute Kidney Injury at 3T	110
5.1.1. Introduction	110
5.1.2. Methods	111
5.1.3. Results	113
5.1.4. Discussion	116
5.1.5. Conclusion	116
5.2. Quantifying the Impact of Diet-Induced Atherosclerotic Plaque Erosions with ¹⁹ F MRI	117
5.2.1. Introduction	117
5.2.2. Methods	118
5.2.2.1. Atherosclerotic Animal Model	118
5.2.2.2. <i>In Vivo</i> ¹⁹ F MR Molecular Imaging	119
5.2.2.3. Histology	120
5.2.3. Results	121
5.2.4. Discussion	125

5.2.5. Conclusion	126
5.3. Acknowledgements	126
5.4. References	127
6. Imaging Peripheral Arterial Disease in Amputated Human Lower Extremity Specimens	132
6.1. Introduction	132
6.2. Methods	133
6.3. Initial Results	135
6.4. Discussion	138
6.5. Acknowledgements	139
6.6. References	139
7. Conclusion	142
7.1. Summary of Major Findings	142
7.2. Future Work	144
7.2.1. ¹⁹ F/ ¹ H Dual-Tuned RF Coils	144
7.2.2. Human <i>In Vivo</i> Applications	145
7.3. References	146

List of Figures

- Figure 1.1** Perfluorocarbon nanoparticle (~250 nm diameter) theranostic contrast agent can be functionalized by inserting various targeting ligands and drug payloads into the lipid monolayer. [Graphics courtesy of Kereos, Inc.]
- Figure 1.2** Gd-bearing nanoparticles targeted to angiogenesis provide T₁-weighted signal to create 3D maps of neovasculature. 3D Neovasculature maps indicating “angiogenic switch” in VX2 tumor. Bars indicate percent of tumor volume enhancing. [Figure reprinted with permission from Schmieder et al.]
- Figure 1.3** **(Top)** Black blood image of the thoracic aorta (arrow) and segmentation of the vessel wall (outlined in yellow) is shown for the week 0 image. The color-coded overlay of signal enhancement (%) shows patchy areas of high angiogenesis. On the week 1 image, the signal enhancement has clearly decreased due to the antiangiogenic effect of targeted fumagillin treatment. **(Bottom)** The level of signal enhancement gradually increases at weeks 2 and 3 after fumagillin treatment, until week 4, when the level of enhancement is practically identical to the week 0 image. [Figure reprinted with permission from Caruthers et al.]
- Figure 1.4** Cardiac magnetic resonance signal enhancement up to 8 weeks after treatment with targeted fumagillin nanoparticles with and without oral atorvastatin. **(Top)** Cardiac magnetic resonance enhancement in untreated (triangles), atorvastatin-treated (circles) and fumagillin-treated animals (squares) during 8 weeks of follow-up imaging. Untreated and statin-treated animals showed a constant level of angiogenesis in the aortic wall. Animals treated with targeted fumagillin nanoparticles at 0 and 4 weeks showed decreased angiogenesis (*p < 0.05) after each dose, which returned to baseline levels within 4 weeks. **(Bottom)** Enhancement in rabbits receiving atorvastatin alone (triangles) or in conjunction with 1 (squares) or 2 (circles) doses of targeted fumagillin nanoparticles. The combination of 2 fumagillin doses and statin produced a sustained decrease in angiogenesis (*p < 0.05). [Figure reprinted with permission from Winter et al.]
- Figure 1.5** ¹⁹F imaging and spectroscopy of crown ether nanoparticles bound to fibrin in ruptured plaque of human carotid artery specimen. The separate ¹H and ¹⁹F images **(top, left)** can be combined with ¹⁹F overlaid on ¹H anatomy **(magnified, right)**. [Figure reprinted with permission from Caruthers et al.]
- Figure 1.6** **Left:** T₁-Weighted Imaging of Fibrin Clots. **(A)** Paramagnetic CE nanoparticles, bound to the clots in cross section, appear as a bright line of signal enhancement with intensity decreasing linearly as the concentration of paramagnetic CE nanoparticle decreases (left to right). Maximum intensity projection through the 3D data depicts the clots *en face* **(B)**. **Mid Left:** Volume selective ¹⁹F spectra from clots show the concentration of crown ether (CE) decreases inversely with perfluorooctyl bromide (PFOB). **Mid Right:** ¹⁹F MR Imaging of PFC NP Bound to Fibrin Clots. These three fluorine images, which have no proton “background,” are oriented

perpendicular to the clots as in A. They illustrate the fibrin-bound PFC nanoparticles of various mixtures applied to the clots. In a broad bandwidth excitation (**top**), all fibrin clots enhance brightly. Narrow bandwidth excitation allows independent visualization of the CE or PFOB nanoparticles. **Right:** ^{19}F Image-based quantification allows relative quantification of NP concentration on clots. [Figure reprinted with permission from Caruthers et al.]

Figure 1.7 ^{19}F MRI (*ex vivo*) of disrupted human carotid artery endarterectomy specimen with atherosclerotic plaque and overlying thrombus using fibrin-targeted PFC NP. **Left:** an optical image of a human carotid endarterectomy sample shows moderate luminal narrowing and several atherosclerotic lesions. **Middle:** A ^{19}F projection image acquired through the entire thickness of carotid artery sample shows high ^{19}F signal along the lumen because of the binding of nanoparticles to fibrin. **Right:** The calculated concentration map of bound nanoparticles (nM) in the carotid sample based on ^{19}F signal intensity in each voxel. [Figure reprinted with permission from Morawski et al.]

Figure 1.8 Localization of PFC NPs labeled cells in mice using ^{19}F MRI. (a) ^{19}F MRI trafficking of stem/progenitor cells labeled with either perfluorooctyl bromide (PFOB) (green) or perfluoropolyether (PFPE) (red) nanoparticles. Labeled cells were locally injected into the skeletal muscle of mouse thigh before MRI. (b)–(d) At 11.7-T field strength, ^{19}F spectral discrimination permits respective imaging of $\sim 1 \times 10^6$ PFOB-loaded cells (b) and PFPE-loaded cells (c). The composite ^{19}F (displayed in color) and ^1H (displayed in grayscale) images (d) reveal the location of PFOB labeled cells in the left leg and PFPE labeled cells in the right leg (dashed line indicates $3 \times 3 \text{ cm}^2$ field of view for ^{19}F images). [Figure reprinted with permission from Partlow et al.]

Figure 1.9 The imaging chain of a commercial MR scanner includes many steps in which measurements and adjustments are made, from determining the power settings for accurate flip angles, to B_0 shimming, to inhomogeneities in B_1 for RF transmit and receive; even during the scan eddy currents, B_0 variations, J-coupling, *etc.* can affect quantification outcomes.

Figure 2.1 **Left:** Longitudinal (spin-lattice) relaxation, described by T_1 relaxation time. **Right:** Transverse (spin-spin) relaxation, described by T_2 relaxation time.

Figure 2.2 Timing diagram for a 90° RF pulse (**top**) followed by a free induction decay (FID) signal (**bottom**) of net magnetization in the transverse plane, detectable by a RF receiver coil.

Figure 2.3 **Left:** Chemical structure of perfluoro-15-crown-5-ether (PFCE). ^{19}F NMR spectrum of PFCE, resulting in a single resonance peak since all ^{19}F nuclei experience the same local magnetic field.

- Figure 2.4** (a) Chemical structure of perfluorooctyl bromide (PFOB; $\text{CF}_3\text{-(CF}_2\text{)}_6\text{-CF}_2\text{Br}$). (b) Representative MR spectrum of PFOB. The J-coupling constant between CF_3 and the adjacent CF_2 group is 12.3 Hz.
- Figure 2.5** Schematic diagram of a coupled resonator circuit. (a) the resonator formed by capacitor C_{t2} and probe (with inductance L) is capacitively coupled, by capacitor C_c , to the secondary resonator formed by capacitor C_{t1} and inductor L . (b & c) the equivalent circuit of in-phase and anti-phase mode. (d) coupled resonator is capacitively matched to 50 Ohm with C_m . [Figure reprinted with permission from Hu et al. (29)]
- Figure 2.6** $^{19}\text{F}/^1\text{H}$ dual-tuned RF coil circuit. (a) Equivalent circuit diagram of two separate LCR resonators (L_1, C_1, R_1) and (L_2, C_2, R_2) electrically coupled via capacitor C_3 . (b) Image of second resonator circuit with coupling capacitors (C3A and C3B) and matching capacitors (C4A and C4B) labeled. (c) Theoretical impedance magnitude output of a SPICE simulation of two capacitively coupled resonators. [Figure reprinted with permission from Hockett et al. (28)]
- Figure 2.7** Photographs of single-turn solenoid RF coils. (a) Smaller coil (8 cm diameter). (b) Larger coil (11.5 cm diameter). (c) T/R box that interfaces with clinical scanner.
- Figure 2.8** Simultaneous dual-frequency return loss (S11) of single-turn solenoid coil measured using network analyzer. Return loss, better than -30 dB, is observed at both the ^1H (127.8 MHz) and ^{19}F (120.2 MHz) resonance frequencies.
- Figure 2.9** Arrangement of capacitors used to spread out the current in the 8 cm diameter $^{19}\text{F}/^1\text{H}$ dual-tuned single-turn solenoid coil.
- Figure 2.10** (a) T_1 -weighted ^1H FFE image of saline phantom using 8 cm diameter $^{19}\text{F}/^1\text{H}$ dual-tuned solenoid coil. (b) Signal intensity profile over the distance of the phantom, as indicated.
- Figure 2.11** (a) AFI B_1 map of saline phantom using 8 cm diameter $^{19}\text{F}/^1\text{H}$ dual-tuned solenoid coil ($119.76\% \pm 0.03\%$ actual/requested flip angle). (b) AFI intensity profile over the distance of the phantom, as indicated.
- Figure 2.12** ^1H (a) and ^{19}F (b) images of a rat lung model of asthma using simultaneous $^{19}\text{F}/^1\text{H}$ imaging of $\alpha_v\beta_3$ -integrin targeted PFC NP.
- Figure 3.1** a: Perfluorooctyl bromide (PFOB: $\text{CF}_3\text{-(CF}_2\text{)}_6\text{-CF}_2\text{Br}$) ^{19}F spectrum. b: All chemical shift components of PFOB CF_2 line group ($\beta, \gamma, \delta, \epsilon, \zeta, \rho$) remain within a phase range of $\pm 90^\circ$ for 0.5 ms. c: ^{19}F signal evolution of the $(\text{CF}_2)_6$ line group with and without apparent T_2 relaxation. During a fast FID readout as in the balanced UTE-SSFP technique, the relative signal remains above 60%, which cannot be recovered for later echo times. [Figure reprinted from Goette, et al. *In press*]

- Figure 3.2** A simultaneous 3D $^{19}\text{F}/^1\text{H}$ balanced UTE-SSFP pulse sequence, consisting of simultaneous $^{19}\text{F}/^1\text{H}$ RF excitation and subsequent FID acquisition at an ultra-short echo time, using balanced gradients (m , m_r) with a Wong-type (39) radial readout trajectory. [Figure reprinted from Goette, et al. *In press*]
- Figure 3.3** Magnitude ^{19}F image of sensitivity imaging phantom, showing PFOB signal acquired with balanced UTE-SSFP sequence. ROI show locations of ^{19}F signal (I_0) [middle], and noise [right] used for SNR calculations. [Figure reprinted from Goette, et al. *In press*]
- Figure 3.4** Molecular imaging of $\alpha_v\beta_3$ -integrin targeted NP on VX2 tumors (arrows) in rabbits by ^{19}F MRI. Gd-free (**a,b,c**) or Gd-containing (**d,e,f**) NP with a perfluorooctyl bromide (PFOB) core were used and imaged with a novel balanced UTE-SSFP based 3D radial sequence. ^1H images show T_1 -based enhancement only with Gd NP (**d**), while the ^{19}F signal is clearly detected in both cases (**b&e**). Image overlays (**c&f**) demonstrate the anatomical co-localization. [Figure reprinted from Goette, et al. *In press*]
- Figure 3.5** Simultaneous $^{19}\text{F}/^1\text{H}$ molecular imaging of angiogenesis targeted perfluorooctyl bromide nanoparticles in a rabbit model of atherosclerosis using 3D radial balanced UTE-SSFP. Proton image (**a**) with 1.25 mm isotropic voxels show anatomy, upon which ^{19}F image can be overlaid (**b**). The ROI in (**b**) is surrounding the aorta, which has a diameter of about 5 mm. The ^{19}F overlay within the aortic region is in green, and extra-aortic ^{19}F signal is blue.
- Figure 3.6** Modeled steady-state gradient echo signal as a function of flip angle (α) for balanced SSFP (“R-FFE”, red line), GRE (“N-FFE”, blue line), and RF-spoiled GRE (“T₁-FFE”, green line) using an estimated actual T_2 of 110 ms.
- Figure 4.1** $^{19}\text{F}/^1\text{H}$ dual-tuned RF coils. (**a**) Single loop rectangular surface coil (7×12 cm, Philips Healthcare, Best, The Netherlands). (**b**) Custom-built 6-element semi-cylindrical coil (15 cm diameter), and (**c**) single-turn solenoid coil (11.5 cm diameter, 14 cm length). [Figure reprinted from Goette, et al. *In review*]
- Figure 4.2** Representative flip angle sweep (10°-210°) on ^{19}F nucleus (**top**) and ^1H nucleus (**bottom**) using the same power setting (peak power = 122.9 W) with a $^{19}\text{F}/^1\text{H}$ dual-tuned surface coil indicating correct power settings for ^{19}F , but too high for ^1H . [Figure reprinted from Goette, et al. *In review*]
- Figure 4.3** 3D Ball plot representation of optimized RF power settings (peak power, W) for ^{19}F (**a**) and ^1H (**b**) nuclei using a $^{19}\text{F}/^1\text{H}$ dual-tuned surface coil and a point source phantom of PFCE NP emulsion. (**c**) Ratio of optimum $^{19}\text{F}/^1\text{H}$ power setting yields a spatially independent calibration value (1.48 ± 0.06 for surface coil). [Figure reprinted from Goette, et al. *In review*]

- Figure 4.4** Power settings (peak power, W) needed to optimize 90° flip angle for ^{19}F and ^1H signals from point source phantom at 9 mm, 15 mm, and 27 mm above $^{19}\text{F}/^1\text{H}$ dual-tuned surface coil (a), semi-cylindrical coil (b), and within single-turn solenoid coil (c). [Figure reprinted from Goette, et al. *In review*]
- Figure 4.5** ^{19}F MRI of phantom with two vials of 1.0 M NaF in agar using a simultaneous $^{19}\text{F}/^1\text{H}$ bFFE sequence and a $^{19}\text{F}/^1\text{H}$ dual-tuned surface coil. Before correction, ^{19}F image (a) and $^{19}\text{F}/^1\text{H}$ overlay image (b) illustrate the inhomogeneous RF field produced by the surface coil, resulting in a mean signal intensity of 2537 ± 31 a.u. and 863 ± 7 a.u. in each vial. ^1H B_1 -field was mapped with actual flip angle imaging (% actual/requested FA) (c), and input into bFFE signal model to create a correction factor (d), which was used to compensate ^{19}F and ^1H signal intensities. The corrected ^{19}F image (e) and $^{19}\text{F}/^1\text{H}$ overlay image (f) demonstrate the image-based compensation technique, resulting in a mean signal intensity of 2621 ± 27 a.u. and 2681 ± 23 a.u. in each vial. [Figure reprinted from Goette, et al. *In review*]
- Figure 4.6** One-way ANOVA analysis of the ^{19}F signal intensity from phantom of two PFC NP vials (1: closer to coil; 2: farther away) before (left) and after (right) B_1 -mapping compensation.
- Figure 4.7** ^{19}F MRI of homogeneous phantom (1.0 M NaF in 2% agar) using a simultaneous $^{19}\text{F}/^1\text{H}$ bFFE sequence and a $^{19}\text{F}/^1\text{H}$ dual-tuned surface coil. Before correction, ^{19}F image (a) and $^{19}\text{F}/^1\text{H}$ overlay image (b) show result of inhomogeneous RF field produced by surface coil. ^1H B_1 -field was mapped with actual flip angle imaging (% actual/requested FA) (c), and input into bFFE signal model to create correction ratio (d), which was used to correct ^{19}F and ^1H signal intensities. Corrected ^{19}F image (e) and $^{19}\text{F}/^1\text{H}$ overlay image (f) demonstrate image-based correction technique. [Figure reprinted from Goette, et al. *In review*]
- Figure 4.8** B_1 -mapping compensation of in vivo cancer model in rabbit with the use of $\alpha_v\beta_3$ -integrin-targeted PFC NP nanoparticles captured by ^{19}F MRI with a $^{19}\text{F}/^1\text{H}$ dual-tuned surface coil (located at image right). In the uncorrected ^{19}F image overlaid on the high-resolution ^1H image (a), PFC NP concentration was quantified as 20.0 ± 0.12 mM $_{^{19}\text{F}}$, compared to an external standard of known concentration (150 mM $_{^{19}\text{F}}$). Illustrated are: B_1 -field mapping with AFI (% actual/requested FA) (b) and calibration mask calculated from a balanced UTE-SSFP signal model (c). In the corrected ^{19}F image overlaid on the high-resolution ^1H image, PFC NP concentration was quantified as 25.5 ± 0.10 mM $_{^{19}\text{F}}$. [Figure reprinted from Goette, et al. *In review*]
- Figure 5.1** (a) ^1H TSE image of unilateral permanent occlusion of renal artery in rat left kidney. (b) ^{19}F bFFE image of PFCE NP emulsion injected i.v. (3 ml/kg). Location of kidneys outlined in red (arrow: injured left kidney). (c) ^{19}F image false-colored in green overlaid on ^1H image.

Figure 5.2 (a) ^1H TSE image of *ex vivo* rat kidney cross-section showing cortex [C] and medulla [M]. *In vivo* rat kidney cross sections showing renal perfusion via ^{19}F imaging of PFCE NP emulsion (3 ml/kg) in the following: (b, c) normal controls-L, R; (d, e) permanently occluded-L, contralateral control-R; (f, g) ischemia/reperfusion-L, contralateral control-R. (h, i) *Ex vivo* ^{19}F imaging of ischemia/reperfusion-L, contralateral control-R.

Figure 5.3 (a) Cross-sectional ^1H image of rat anatomy, showing left injured kidney in an ischemia/reperfusion model of AKI and external ^{19}F standard outlined in red. (b) ^{19}F MR image using simultaneous $^{19}\text{F}/^1\text{H}$ bFFE sequence of PFCE NP emulsion (3 ml/kg) circulating for 5 min. Compared to external PFCE standard (150 mM $_{19\text{F}}$), ^{19}F signal was quantified in the kidney, which showed lower renal perfusion in the medulla (63.8 ± 10.9 mM $_{19\text{F}}$) than in the cortex (82.8 ± 6.9 mM $_{19\text{F}}$). (c) ^{19}F image overlaid in green on ^1H image showing colocalization of standard and renal ^{19}F signal. (d) B_1 map using AFI (% actual/requested flip angle) demonstrating that nearly the same flip angle was achieved in the ^{19}F standard (95.2 ± 6.0 %) as in the kidney (95.9 ± 3.4 %) with the $^{19}\text{F}/^1\text{H}$ dual-tuned solenoid coil.

Figure 5.4 (a) Long-axis ^1H image of rat anatomy, showing left injured kidney in an ischemia/reperfusion model of AKI outlined in red. (b) B_1 map using AFI (% actual/requested flip angle) showing homogeneous RF field within field-of-view (FOV) (~ 5 cm long) of $^{19}\text{F}/^1\text{H}$ dual-tuned solenoid coil (c), which falls off outside coil FOV.

Figure 5.5 ^{19}F MRI of 1 ml/kg PFC NP emulsion injected into normal chow rabbit 3 min prior to imaging. (a) ^{19}F bFFE image without REST slab shows long-axis view of the rabbit, with ^{19}F signal detectable in aorta, liver, and kidney, confirmed with colocalization in $^{19}\text{F}/^1\text{H}$ overlay image (c). A REST slab perpendicular to the imaging slice eliminates ^{19}F signal from image (b & d). REST slab and imaging slice location (e).

Figure 5.6 Cross-sectional ^{19}F MR images without (a) and with (b) one parallel REST slab proximal to the imaging slice, which eliminates only aortic ^{19}F signal from circulating PFC NPs, confirmed with ^{19}F overlays (green) on ^1H images (c & d).

Figure 5.7 Locations of saturation bands used to eliminate ^{19}F signal from flowing blood proximal and distal to imaging slice (which continued beyond the image FOV). Aorta, shown in red, was imaged with a time-of-flight angiogram. [Figure reprinted from Palekar, Goette, et al. *In preparation*]

Figure 5.8 Cross-sectional ^1H images of (a) normal chow rabbit and (d) cholesterol fed rabbit showing location of abdominal aorta (red box). ^{19}F bFFE images of PFCE nanoparticle ^{19}F signal in the region of interest for (b) normal chow rabbit and (e) cholesterol fed rabbit. Saturation bands proximal and distal to imaging slice eliminate ^{19}F signal from blood. ^{19}F signal (green) overlaid on ^1H image showing ^{19}F signal colocalization for the region of interest in a (c) normal chow rabbit and

(f) cholesterol fed rabbit, demonstrating deposition of PFC-NP only in inflamed abdominal aorta (AA) and vena cava (VC). Representative oil red O stains of the imaged area showing plaque elements in (g) normal chow rabbit and (h) cholesterol fed rabbit. Scale bars denote 500 μm . [Figure reprinted from Palekar, Goette, et al. *In preparation*]

Figure 6.1 (a) T_1 -weighted ^1H FFE coronal image of leg phantom. Setup of MR angiography of phantom with flowing (~ 8 cm/s) saline doped 5000:1 with Gd^{3+} using M2D TOF (multiple 2D, time-of-flight) ^1H imaging with REST slab position (b). MRA maximum intensity projection (MIP) and MIP overlay on ^1H image without (c&d) and with a REST slab (e&f) saturating the spins in the return flow.

Figure 6.2 (a) Semi-cylindrical $^{19}\text{F}/^1\text{H}$ dual-tuned coil. (b) Leg phantom, consisting of tubing encased within 2% agar in 2L bottle. Actual Flip Angle Imaging (% Actual/Requested Flip Angle) maps in the transverse (c) and sagittal (e) views with corresponding profile plots (d & f) increasing in distance away from the coil (location illustrated in red).

Figure 6.3 T_1 -weighted ^1H FFE transverse (a) and coronal (b) images of leg phantom. Simultaneous $^{19}\text{F}/^1\text{H}$ imaging of PFCE NP emulsion in leg phantom tubing (static) using bFFE sequence in transverse (c) and coronal (d) planes. Note: banding artifacts from coil are present in coronal slice. ^{19}F image using balanced UTE-SSFP sequence in transverse plane (e), with coronal MIP (f).

Figure 6.4 MR angiography of leg with flowing (600 ml/hr) saline using M2D TOF (multiple 2D, time-of-flight) ^1H imaging. Maximum intensity projections (MIP) in coronal (a), sagittal (b), and transverse (c) planes. MRA setup and slice orientation (d).

Figure 6.5 (a) High-resolution T_1 -weighted ^1H FFE transverse image of leg anatomy (arrow: cannulated artery). (b) ^{19}F imaging of PFCE NP emulsion (~ 2 ml/kg) in artery using balanced UTE-SSFP sequence in transverse plane. Other ^{19}F signal from PFC NP emulsion that pooled outside the specimen due to leaking from an absence of a return circuit.

Figure 7.1 Unique $^{19}\text{F}/^1\text{H}$ dual-tuned coil design (left) and circuit diagram (right) with active switching, allowing for transmission using an outer coil element and reception using an inner coil element.

List of Tables

Table 1.1 NMR Properties of Proton and Non-proton Nuclei with Net Nuclear Spin

Table 1.2 Biological Abundance of Relevant NMR Nuclei in the Human Body

Table 1.3 NMR Spectral Ranges for Different Nuclei

Table 3.1 Sensitivity of ^{19}F MR Acquisition Techniques

Acknowledgments

I have been honored to work with a diverse group of scientists at the Consortium for Translational Research in Advanced Imaging and Nanomedicine (C-TRAIN) at Washington University in St. Louis, to whom I am truly grateful. First and foremost, I would like to thank my advisor, Dr. Samuel Wickline, who has continually provided insight, support, and a positive, collaborative environment for me to explore any and all potential research interests. One of many of Sam's professional qualities that I will strive to emulate is his ability to seek out and ask clinically relevant research questions, which, when answered, have the potential to change specific clinical outcomes. Additionally, I appreciate the leadership of Dr. Gregory Lanza, who showed me how to conduct and manage research projects with scientific rigor, all while keeping an ultimate clinical goal in mind. Much of my theoretical knowledge and hands-on experience with MRI can be directly attributed to Dr. Shelton Caruthers, who took me under his wing when I decided to shift research projects. I truly appreciate the time and energy that Shelton invested into my training, as well as his seemingly endless plethora of research ideas.

I have thoroughly enjoyed collaborating with the past and present students, scientists, researchers, and staff at C-TRAIN, including Todd Williams, Frank Hockett, Anne Schmieder Atteberry, Mary Watkins, Dr. Junjie Chen, Dr. Mike Hughes, Dr. Jon Marsh, Dr. Hua Pan, Dr. Josh Hood, Dr. Ya-Jian Cheng, Dr. Lingzhi Hu, Dr. Jacob Myerson, Dr. Kirk Hou, John Stacy Allen, Mike Scott, Dr. Chandu Vemuri, Dr. Charlene Blake, Dr. Sandor J. Kovács, and Sheila Crowder. I can trace many pieces of this dissertation to the hard work of each and every one of you; thank you.

I would like to thank Dr. Joseph Ackerman for not only providing guidance on my thesis committee, but also for teaching me the theory behind nuclear magnetic resonance in his graduate MR course. I am proud to be a part of the rich history of the Biomedical Engineering department at Wash U, which would certainly not exist in its current form without the leadership of Dr. Frank Yin. I would like to thank Dr. Yin for taking the time to meet with me as a curious, yet inexperienced, 17-year-old junior in high school over a decade ago. His passion for BME sparked my interest in this field, which was encouraged by an outstanding high school biology teacher in Elmer Kellmann, and further supported by my undergraduate research advisors at Georgia Tech, Dr. Suzanne Eskin, Dr. Larry McIntire, and Dr. John Oshinski. My experience in

the BME department as Wash U has been enriched by Dr. Mark Anastasio, with whom I have engaged in many helpful discussions about image acquisition, reconstruction, and post-processing as a member of my committee, as well as Dr. Shelly Sakiyama-Elbert, Dr. Larry Taber, Glenn Reitz, and Karen Teasdale.

I have had the privilege to collaborate with several talented and dedicated engineers at Philips Healthcare, including Dr. Jochen Keupp, Dr. Carsten Schirra, Dr. Jürgen Rahmer, and Dr. Melanie Traugber. Their expertise in medical imaging has shaped my experience in clinical MR and will undoubtedly have a lasting impact on my career.

I have been fortunate to receive funding from the American Hearst Association with a predoctoral fellowship (11PRE7530046), several grants to Dr. Wickline and Dr. Lanza from the National Institutes of Health (R01 HL073646, HL112518), and the Barnes-Jewish Hospital Charitable Foundation.

I cannot begin to describe how much I appreciate the love and support of my family and friends. None of this work would have been possible without the encouragement and support of my parents, sister, and in-laws. Finally, and most importantly, I would like to thank my wife, Julie, without whom I would not be the man that I am today.

Matthew John Goette

Washington University in St. Louis

August 2014

Dedicated to the memory of Patrick, from Matt-boy.

ABSTRACT OF THE DISSERTATION

Absolute Quantitation for MR Molecular Imaging of Angiogenesis

by

Matthew John Goette

Doctor of Philosophy in Biomedical Engineering

Washington University in St. Louis, 2014

Professor Samuel Wickline, Chair

Medical imaging is undergoing a transition from an art that is used to make static images of human physiology into a scientific tool that employs advanced techniques to measure clinically relevant data. Recently, the role of magnetic resonance imaging in cardiovascular and oncological research has grown, largely due to the implementation of new quantitative techniques in the clinic. Magnetic resonance imaging (MRI) and spectroscopy (MRS) are particularly rich in their capability to quantify both physiology and disease via biomarker detection. While this is true for many applications of MRI in cardiovascular and oncological research, ^{19}F MR molecular imaging is particularly useful when coupled to the use of emerging site-targeted molecular imaging agents for diagnosis and therapy, such as $\alpha_v\beta_3$ integrin-targeted perfluorocarbon (PFC) nanoparticle (NP) emulsions. Unfortunately, the radiological world is realizing that although image quality may be consistently high, the absolute quantitative values being calculated vary widely across time, techniques, laboratories, and imaging platforms.

The overall objective of this work is to advance the state of the art for ^{19}F MR molecular imaging of perfluorocarbon nanoparticle emulsion contrast agents. To reach this objective, three specific aims have been identified: (1) to create new tools and techniques for ^{19}F MR molecular imaging of PFC nanoparticles, (2) to develop translatable procedures for absolute quantification of ^{19}F nuclei with MR molecular imaging, and (3) to evaluate the potential for clinical translation with *ex vivo* and *in vivo* preclinical experiments. Robust, standardized techniques are developed in this work to improve the accuracy of *in vivo* quantitative ^{19}F MR molecular imaging, validate system performance, calibrate measurements to ensure repeatability of these quantitative metrics, and evaluate the potential for clinical translation. As these quantitative metrics become routine in medical imaging procedures, these standardized calibrations and techniques are expected to be critical for accurate interpretation of underlying pathophysiology. This will also impact the development of new therapies and diagnostic techniques/agents by reducing the variability of image-based measurements, thereby increasing the impact of the studies and reducing the overall time and cost to translate new technologies into the clinic.

Chapter 1. Introduction

1.1 Quantitative Magnetic Resonance Molecular and Functional Imaging

Medical imaging is undergoing a transition from an art that is used to make static images of human physiology into a scientific tool that employs advanced techniques to measure clinically relevant data. This is particularly true for magnetic resonance imaging (MRI), which has been widely adopted as a powerful diagnostic imaging modality with superior soft tissue contrast and an excellent human safety profile, due to a lack of ionizing radiation (1). MRI is increasingly being used to generate quantitative metrics of human physiological function, as seen in the clinic with measurements of myocardial function and viability (2), apparent diffusion coefficient in acute stroke (3), blood flow velocity through a stenotic vessel (4), and first-pass contrast agent kinetics (5), among many others. Alongside the implementation of new imaging procedures is the development of new contrast agents, which include targeted imaging agents and detectable therapeutics. The potential of these “theranostic” agents to offer personalized diagnosis, precise therapy delivery, and unparalleled post-therapy response arises from their quantitative nature (6).

Molecular imaging offers extraordinary potential for studying cell biology, detecting disease biomarkers, and monitoring targeted drug delivery using noninvasive techniques (7-11). Its hallmark is the ability to visualize and characterize the presence of specific cellular indicators of biological processes using a variety of targeting ligands, such as fibrin (12), $\alpha_v\beta_3$ integrin (13), epidermal growth factor receptor (EGFR) (14), and vascular cell adhesion molecule 1 (VCAM-1) (15). Perhaps more profoundly and clinically useful is the potential for quantification, not only of biomarkers, but also of targeted drug delivery and therapy response (16-18). While relative

values derived from images are helpful, absolute and accurate measures are required for pre-clinical and clinical studies, as well as ultimate clinical therapy utility. Accurate and stable quantification is especially vital where time-varying biomarker information is required, such as in pharmacodynamic studies.

Functional imaging presents an opportunity to observe and quantify pathophysiological changes to tissue or organ functionality in response to disease or external stimulus. Recent developments in MRI techniques and contrast agents afford numerous opportunities for direct and noninvasive readouts of essential functional indexes such as diffusion (19), perfusion (5), pH (20), and blood oxygenation (21). Since molecular and functional imaging offer different but complementary insights into the same pathophysiological processes, there is a growing interest in devising reliable platforms that permit accurate and repeatable quantitative molecular and functional readouts of the underlying biological mechanism of disease states in a more comprehensive manner (22,23).

While molecular and functional imaging are generally robust due to the combination of various imaging modalities, magnetic resonance imaging alone is a rich molecular and functional imaging modality because of the inherent ability to image various contrasting tissue characteristics, and the ability to take spectroscopic and parametric measurements. Most current MR techniques are qualitative (i.e., relative), often requiring pre- and post-agent imaging with subsequent image registration and comparison. Current “absolute” methods are still, in reality, relative measures in that they vary temporally and spatially within an imaging system (e.g., due to hardware sensitivity, tuning, scaling, etc.) and across imaging systems (e.g., due to differences in hardware, techniques, etc.).

As these new quantitative imaging techniques undergo clinical evaluation, their precision, accuracy, and repeatability must be fine-tuned and standardized before they can be fully integrated into the clinical setting. Robust methods of quantitative imaging will also be essential in the pre-clinical development of novel contrast agents, therapeutics, and diagnostic protocols. Just as imaging techniques with known endogenous and exogenous contrast mechanisms require thorough testing, the eventual translation of these new agents into the clinic will require robust, precise, and repeatable quantitative imaging protocols.

1.1.1 Proton MR Molecular and Functional Imaging

Magnetic resonance molecular and functional imaging is generally divided into two options based on the imaging nucleus of choice: proton and non-proton. Non-proton MRI is employed to directly visualize clinically relevant exogenous contrast agents or molecules that contain nuclei other than hydrogen exhibiting net nuclear spin in external magnetic fields. Proton imaging utilizes intrinsic or agent-induced local relaxation modulation of hydrogen (^1H) nuclei, which contain a single proton and no accompanying neutron. In proton imaging, detected ^1H spins are correlated with the expression of biochemical markers or the quantitative value of specific functional indexes. ^1H MR molecular and functional imaging offers a wide variety of contrast mechanisms that can be utilized by modifying the contrast agent, pulse sequence, and imaging protocol. Contrast can be generated either by manipulating endogenous tissue relaxation properties, or by detecting the effects of exogenous contrast agents.

Several relevant endogenous contrast-based functional imaging approaches are in or entering clinical use. Among them, diffusion tensor MRI (DTI) correlates water diffusion in soft tissue with a magnetic resonance readout and delineates tissue microstructures resulting from

restricted boundaries for water diffusion (19). Arterial spin labeling (ASL) utilizes a special pulse sequence and applies RF power to magnetically label arterial blood flow (24). ASL is widely studied as an alternative method to traditional perfusion imaging techniques, which utilize potentially nephrotoxic contrast agents. Blood-oxygenation-level-dependent (BOLD) MRI permits non-invasive detection of tissue functionality by measuring T_2^* contrast generated by deoxyhemoglobin in metabolically active tissues that are extracting and using oxygen (21).

Exogenous ^1H contrast agents are engineered for several clinical applications by utilizing a variety of targeting ligands, many of which exhibit well-characterized biochemical properties. NMR scientists exploit a wide range of physical properties of these agents, which typically generate contrast by modulating the local relaxation of ^1H nuclei in one of the following manners. Superparamagnetic iron oxide (SPIO) particles generate local magnetic field inhomogeneities that can be visualized using T_2^* -weighted gradient echo imaging sequences (25). Additionally, paramagnetic contrast agents containing metals such as gadolinium (Gd^{3+}) and manganese (Mn^{2+}) encode agent concentration into signal intensity on T_1 -weighted images (26). New techniques to image endogenous cellular proteins or exogenous agent-introduced peptides by indirectly affecting ^1H resonances include chemical exchange saturation transfer (CEST) (27) and amide proton transfer (APT) (28,29). Finally, techniques like spin-lattice relaxation time in the rotating frame ($T_{1\rho}$) (30) have drawn attention recently, but the clinical adoption of these newer methods still remains under investigation.

Hydrogen has been the dominant imaging nucleus of choice largely due to the numerous mechanisms to quickly generate high-contrast clinical images with proton MRI; however, ^1H molecular and functional imaging is not without its drawbacks. All ^1H -based imaging techniques are best performed with a pre-contrast baseline scan as well as the endogenous or exogenous

contrast scan of interest. As such, these imaging approaches are highly susceptible to patient motion between the two scans, which make accurate and repeatable image coregistration difficult in the clinic. In addition, proton molecular and functional applications often suffer from the omnipresent ^1H background signal, which may hinder the unambiguous identification of sparse molecular targets or detection of small changes in tissue functionality.

1.1.2 Non-proton MR Molecular and Functional Imaging

Non-proton MR molecular and functional imaging, on the other hand, is not plagued by the abundant proton background signal because ^1H nuclei are ignored, which might allow in certain circumstances for the specific and sensitive detection of various disease biomarkers and metrics of tissue functionality if the imaged nuclear spectrum is unique with no confounding background. As an unavoidable tradeoff, however, non-proton MRI is more technically challenging because of lower gyromagnetic ratios and inherently lower natural abundance of detectable nuclei in patients compared to ^1H MRI (31).

Table 1.1 shows several non-proton nuclei exhibiting net nuclear spin in an external magnetic field, which are detectable with MR. Compared to ^1H with a gyromagnetic ratio (γ) of 42.5 MHz/T, phosphorus (^{31}P) and sodium (^{23}Na) have much lower resonance frequencies (^{31}P : $\gamma = 17.2$ MHz/T, ^{23}Na : $\gamma = 11.3$ MHz/T). Since MR sensitivity is roughly proportional to γ^2 according to Curie's Law (32), ^{31}P and ^{23}Na exhibit much lower relative sensitivities when detected with MR, calculated in Table 1.1 as 0.066 and 0.092, respectively, compared to ^1H (1.000). Despite relatively low MR sensitivity, ^{31}P and ^{23}Na are widely exploited as endogenous non-proton nuclei for functional imaging in evaluating tissue metabolism and electrophysiology because they are key components in many important organic and inorganic molecules that are

naturally present in animals and humans (33,34). Sodium imaging, in particular, has been successfully utilized to enhance knee imaging in the clinic (35,36). ^{13}C also has a very low relative sensitivity (0.01591), but can be hyperpolarized yielding several thousand fold increases in sensitivity, allowing researchers to probe several key biochemical pathways including glycolysis, the citric acid cycle, and fatty acid synthesis (37,38).

Table 1.1 NMR Properties of Proton and Non-proton Nuclei with Net Nuclear Spin

Nucleus	Abundance (%) ^a	Net Nuclear Spin, I	Gyromagnetic Ratio, γ (MHz/T)	Relative Sensitivity ^b
^1H	99.9885	1/2	42.5775	1.00000
^2H	0.0115	1	6.5359	0.00965
^{31}P	100	1/2	17.2515	0.06652
^{23}Na	100	3/2	11.2688	0.09270
^{14}N	99.636	1	3.0777	0.00101
^{13}C	1.07	1/2	10.7084	0.01591
^{19}F	100	1/2	40.0776	0.83400

^a Natural abundance of the isotope in percent.

^b Sensitivity relative to ^1H (1.000) assuming an equal number of nuclei and constant temperature. Values were calculated from expression for constant applied field (M_0): $0.0076508(\mu/\mu_N)^3(I+1)/I^2$, where I is the net nuclear spin, and μ/μ_N is the nuclear magnetic moment in units of the nuclear magneton μ_N (39).

The gyromagnetic ratio of fluorine (^{19}F) nuclei (40.1 MHz/T), on the other hand, is very close to ^1H (42.5 MHz/T), only 6% different (a separation of 7.6 MHz at 3T) (40). As such, ^{19}F spins generate favorably comparable MR signal to ^1H spins with a relative sensitivity of 0.834, or about 83% that of ^1H ; this is much stronger than the other non-proton imaging nuclei that are detectable with MR. Additionally, there is essentially no ^{19}F background signal in the human body (or other small animals) under physiological conditions, as seen by Table 1.2. Therefore, ^{19}F MR imaging, typically performed with a fluorinated contrast agent, is a promising molecular imaging approach with the potential for extraordinary specificity. As a point of clarification, the ^{19}F nomenclature is used throughout to distinguish this 100% naturally-occurring (non-radioactive) isotope of fluorine (with an atomic number of 19) from radioactive ^{18}F , which is

frequently used in fluorodeoxyglucose (^{18}F -FDG) positron emission tomography (PET) scans. Finally, because ^{19}F atoms can be readily engineered into various organic molecules by substituting for existing ^1H atoms, ^{19}F MRI with appropriately functionalized contrast agents represents a versatile imaging paradigm for quantitatively probing biomarker expression at the molecular level (41,42).

Table 1.2 Biological Abundance of Relevant NMR Nuclei in the Human Body

Element	Relevant NMR Nucleus	Biological Abundance ^a
Hydrogen	^1H	0.63
Phosphorus	^{31}P	0.0024
Sodium	^{23}Na	0.00041
Nitrogen	^{14}N	0.015
Carbon	^{13}C	0.094
Fluorine	^{19}F	0.000012

^a Biological abundance is the fraction of one type of atom in the human body, calculated from (43).

1.2 Perfluorocarbon Nanoparticle Emulsion Contrast Agents

On the forefront of this new molecular and functional imaging paradigm are the ligand-targeted perfluorocarbon (PFC) nanoparticle (NP) emulsions invented in our labs at Washington University. This multifunctional agent (Fig. 1.1) is comprised of a lipid monolayer encapsulating a hydrophobic perfluorocarbon core with PFCs such as perfluoro-15-crown-5-ether (PFCE; $\text{C}_{10}\text{F}_{20}\text{O}_5$) or perfluorooctyl bromide (PFOB; $\text{CF}_3\text{-(CF}_2)_6\text{-CF}_2\text{Br}$), which generate nanoparticles following an emulsification process (44). These perfluorocarbons are a type of fluorine-containing molecule derived from hydrocarbons by complete substitution of ^1H with ^{19}F atoms. PFOB in particular has been clinically approved as a blood substitute for over 20 years and has displayed a very good bio-safety profile because it is biologically inert and not metabolized by human body. The nominal size of a PFC NPs is approximately 250 nm in diameter. The half-life of PFC NPs in the blood stream is ~2-4 hours, and particles are

sequestered by the liver and spleen, with the perfluorocarbon component then cleared by volatilization and exhalation from the lungs.

PFC nanoparticles have proved to be a highly adaptable delivery vehicle for targeted molecular and functional imaging. Targeting ligands can be conjugated covalently or noncovalently to the lipid surface to functionalize the particles. Some have termed these particles “theranostic” agents, combining *therapeutic* drug payloads into the lipid monolayer along with *diagnostic* imaging agents such as chelated gadolinium (Gd) (~100,000 chelates per particle), which can be detected with T₁-weighted proton (¹H) imaging. Additionally, fluorine (¹⁹F) magnetic resonance imaging (MRI) and spectroscopy (MRS) can be used to sensitively detect, specifically identify, and directly quantify the perfluorocarbon core of these nanoparticles in a wide variety of applications (45-50). In addition to their extensive applications in diagnostic imaging, and due to an opportune half-life in the blood stream, PFC NPs have also been exploited as a potential vehicle for drug delivery (6,51-53). For example, PFC nanoparticles have been used pre-clinically to detect thrombus and plaque angiogenesis in atherosclerosis and to deliver antiangiogenic therapy with an image-based readout of dosing efficacy (54,55).

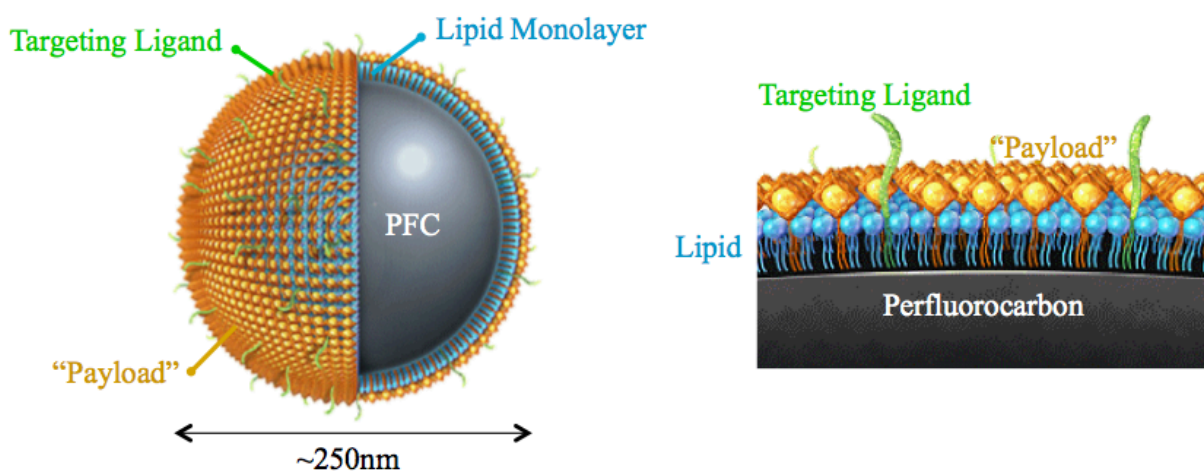


Figure 1.1 Perfluorocarbon nanoparticle (~250 nm diameter) theranostic contrast agent can be functionalized by inserting various targeting ligands and drug payloads into the lipid monolayer. [Graphics courtesy of Kereos, Inc.]

1.2.1 ^1H MR Molecular Imaging of Targeted PFC NP

Applications of PFC nanoparticles as a ^1H contrast agent for molecular imaging have been extensively investigated in preclinical models of cancer and cardiovascular disease, particularly with angiogenesis targeted imaging (54). Conjugation of an RGD peptide or mimetic to the lipid monolayer functionalizes the nanoparticles to the presence of $\alpha_v\beta_3$ integrin, offering active targeting of these particles to neovasculature, or the formation of new blood vessels. When Gd chelates are incorporated into the lipid surface of the particles, there is a direct inner-sphere dipole-dipole interaction between Gd and the water molecules surrounding the biomarker sites, leading to shorter T_1 relaxation times. It has been shown that the chemical structure of the Gd chelates affects the relaxivity of the PFC NP as a ^1H contrast agent, and that chelates with longer linker chains (e.g. DOTA-PE) enhance water relaxation more efficiently than those with shorter chains (e.g. DOTADTPA) (56). Through T_1 -weighted imaging, 3D maps of angiogenesis can be constructed to visualize angiogenesis patterns and temporal development (Fig. 1.2) (57). We have shown that not only visualizing but also assigning values to the extent of angiogenesis present in various tumor models is beneficial in the non-invasive characterization of angiogenesis (55,57-62) and in monitoring (and even predicting) response to therapy (45,63,64).

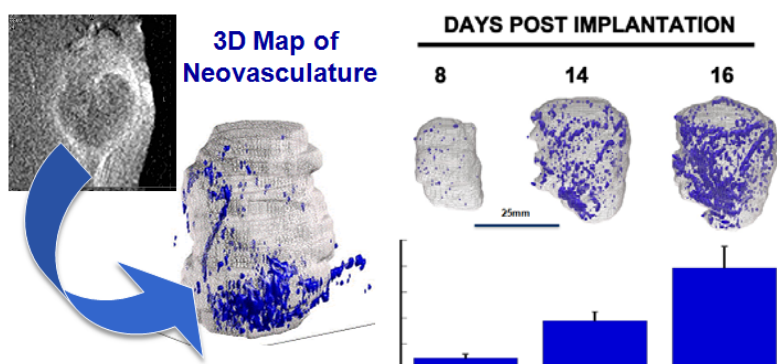


Figure 1.2 Gd-bearing nanoparticles targeted to angiogenesis provide T_1 -weighted signal to create 3D maps of neovasculature. 3D Neovasculature maps indicating “angiogenic switch” in VX2 tumor. Bars indicate percent of tumor volume enhancing. [Figure reprinted with permission from Schmieder et al. (57)]

One series of studies by our group investigated the diagnosis and treatment of angiogenesis in early-stage atherosclerosis with paramagnetic $\alpha_v\beta_3$ -integrin-targeted nanoparticles (63,65,66). It was shown that angiogenesis can be specifically targeted with these nanoparticles and imaged in an *in vivo* hyperlipidemic rabbit model (Fig. 1.3). Furthermore, using a semi-quantitative method to measure MR signal enhancement from digitally segmented rabbit aortas, the response to a combination of antiangiogenic and cholesterol lowering therapy (i.v. fumagillin-loaded nanoparticles plus orally-administered atorvastatin) could be monitored and quantified over time (Figs. 1.3 & 1.4). The combination of targeted fumagillin nanoparticles and atorvastatin synergistically sustained an antiangiogenic effect over several weeks.

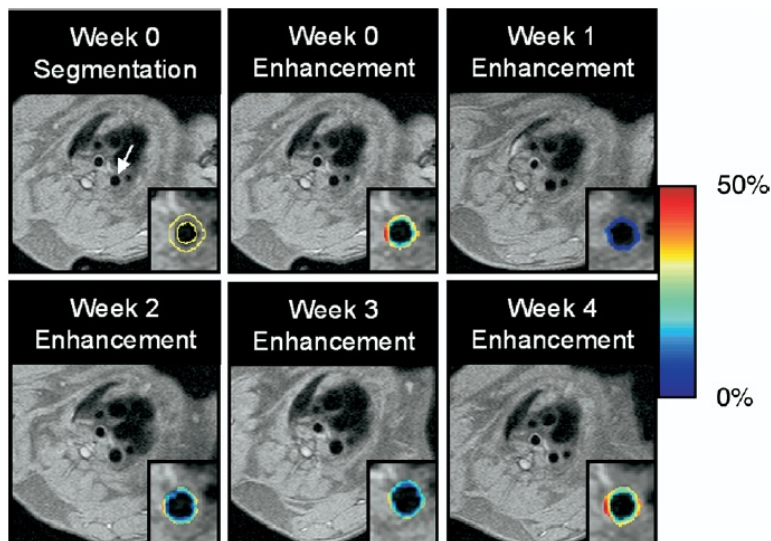


Figure 1.3 (Top) Black blood image of the thoracic aorta (arrow) and segmentation of the vessel wall (outlined in yellow) is shown for the week 0 image. The color-coded overlay of signal enhancement (%) shows patchy areas of high angiogenesis. On the week 1 image, the signal enhancement has clearly decreased due to the antiangiogenic effect of targeted fumagillin treatment. **(Bottom)** The level of signal enhancement gradually increases at weeks 2 and 3 after fumagillin treatment, until week 4, when the level of enhancement is practically identical to the week 0 image. [Figure reprinted with permission from Caruthers et al. (9)]

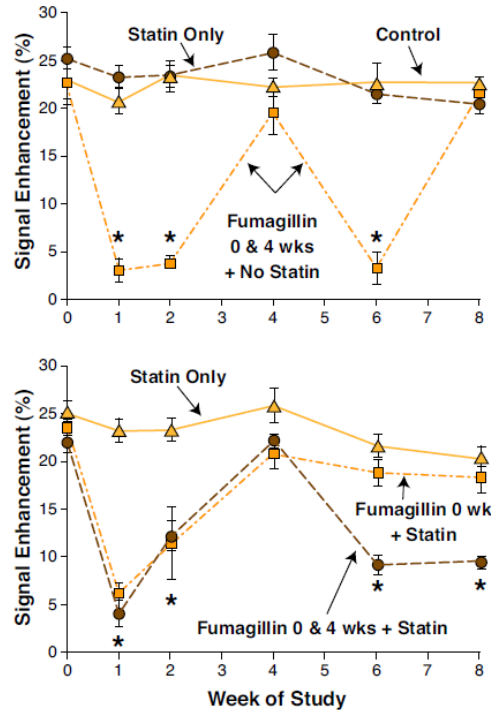


Figure 1.4 Cardiac magnetic resonance signal enhancement up to 8 weeks after treatment with targeted fumagillin nanoparticles with and without oral atorvastatin. **(Top)** Cardiac magnetic resonance enhancement in untreated (triangles), atorvastatin-treated (circles) and fumagillin-treated animals (squares) during 8 weeks of follow-up imaging. Untreated and statin-treated animals showed a constant level of angiogenesis in the aortic wall. Animals treated with targeted fumagillin nanoparticles at 0 and 4 weeks showed decreased angiogenesis (* $p < 0.05$) after each dose, which returned to baseline levels within 4 weeks. **(Bottom)** Enhancement in rabbits receiving atorvastatin alone (triangles) or in conjunction with 1 (squares) or 2 (circles) doses of targeted fumagillin nanoparticles. The combination of 2 fumagillin doses and statin produced a sustained decrease in angiogenesis (* $p < 0.05$). [Figure reprinted with permission from Winter et al. (67)]

In addition to Gd and $\alpha_v\beta_3$ integrin, other combinations of targeting ligands (e.g. $\alpha_5\beta_1$ (57) and Robo4 (68)) and imaging labels (e.g. manganese (69)) can be incorporated into the PFC NP construct to investigate other preclinical disease models. Finally, although these studies show that there is great promise for image-guided therapy using MRI, this process still inherently yields relative measures of disease. From this research, we have experienced firsthand what many others have also observed: that the confidence limits on image-based “quantification” can be quite broad, particularly for MRI.

1.2.2 ^{19}F MR Molecular Imaging of Targeted PFC NP

Targeted PFC nanoparticles actively bind to molecular biomarkers at sites of disease and can be imaged using ^{19}F MRI by detecting the particles' perfluorocarbon core. It has been shown that ^{19}F MRI at clinical field strengths can be used to detect the sparse distribution PFC NPs at very low concentration (picomolar) (70). Additionally, ^{19}F MR can be used to image PFC NPs without conjugated ^1H contrast payloads, and thus avoid potential renal damage that can be triggered by conventional ^1H contrast agents, as is the case with increased risk of nephrogenic systemic fibrosis (NSF) associated with Gd-containing agents (71-74).

Applications of ^{19}F MR molecular imaging have been demonstrated in multiple preclinical animal models of cardiovascular disease and cancer. For example, tumor angiogenesis has been successfully imaged with ^{19}F MRI of $\alpha_v\beta_3$ integrin-targeted PFC NP (75). The same particle with fibrin targeting ligands has been shown to progressively bind to atherosclerotic plaques on arterial walls. We have exploited this technology to target and image *in vitro* thrombus and ruptured plaque in human endarterectomy samples (Fig. 1.5). In addition, when combined with multiple PFCs, it can provide “multi-color” (spectral), highly specific detection and quantification of individual targeted agents (Fig. 1.6) (49).

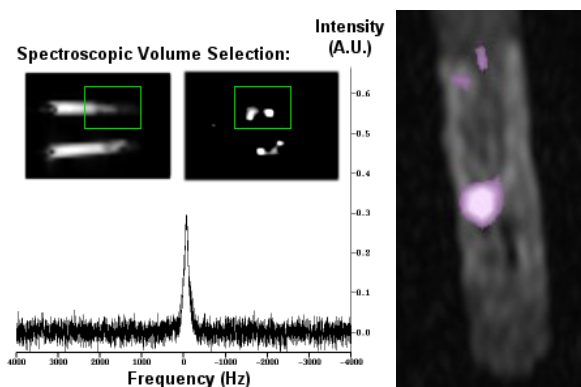


Figure 1.5 ^{19}F imaging and spectroscopy of crown ether nanoparticles bound to fibrin in ruptured plaque of human carotid artery specimen. The separate ^1H and ^{19}F images (**top, left**) can be combined with ^{19}F overlaid on ^1H anatomy (**magnified, right**). [Figure reprinted with permission from Caruthers et al. (49)]

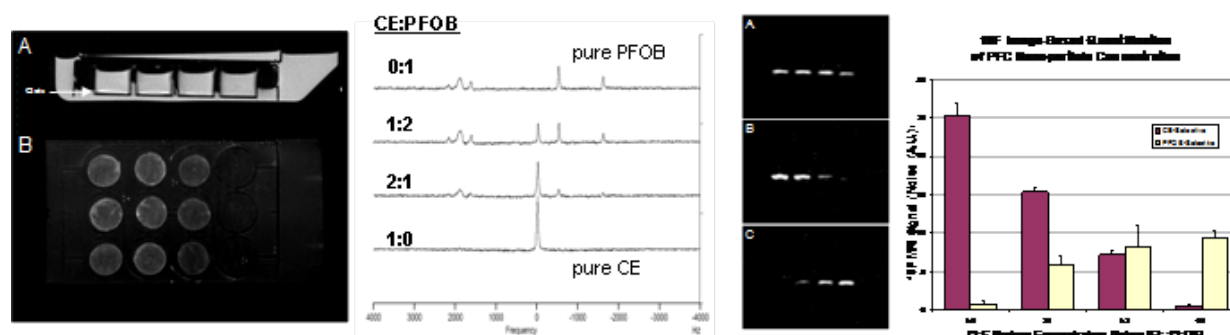


Figure 1.6 Left: T₁-Weighted Imaging of Fibrin Clots. (A) Paramagnetic CE nanoparticles, bound to the clots in cross section, appear as a bright line of signal enhancement with intensity decreasing linearly as the concentration of paramagnetic CE nanoparticle decreases (left to right). Maximum intensity projection through the 3D data depicts the clots *en face* (B). **Mid Left:** Volume selective ¹⁹F spectra from clots show the concentration of crown ether (CE) decreases inversely with perfluorooctyl bromide (PFOB). **Mid Right:** ¹⁹F MR Imaging of PFC NP Bound to Fibrin Clots. These three fluorine images, which have no proton “background,” are oriented perpendicular to the clots as in A. They illustrate the fibrin-bound PFC nanoparticles of various mixtures applied to the clots. In a broad bandwidth excitation (top), all fibrin clots enhance brightly. Narrow bandwidth excitation allows independent visualization of the CE or PFOB nanoparticles. **Right:** ¹⁹F Image-based quantification allows relative quantification of NP concentration on clots. [Figure reprinted with permission from Caruthers et al. (49)]

Another goal of quantitative ¹⁹F MR molecular imaging of site-targeted agents is akin to non-invasive immunohistochemistry (Fig. 1.7) (50). In this particular application, ¹⁹F MRI provides a quantitative readout of retained particle concentration in human endarterectomy samples and confirms a heterogeneous accumulation of PFC NPs throughout the entire lesion (50). Researchers have recently discovered that the porous structure of vulnerable plaques allows plain PFC NP, without any targeting ligands, to penetrate into and accumulate within these plaques through disrupted endothelial barriers (76). Moreover, advanced MR pulse sequences (e.g. diffusion weighted ¹⁹F sequences (77)) and other targeting mechanisms (e.g. VCAM (15)) have been developed to extend ¹⁹F MR molecular imaging of PFC NP to more diverse clinical applications. Finally, recent work by Zhang et al. suggests that PFC NPs without a targeting moiety that passively collect in the vasculature may be of use in atherosclerosis imaging (76).

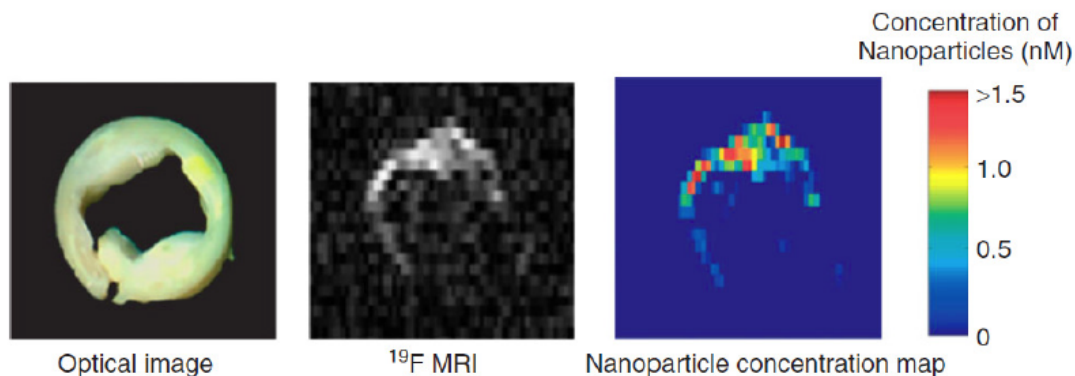


Figure 1.7 ^{19}F MRI (*ex vivo*) of disrupted human carotid artery endarterectomy specimen with atherosclerotic plaque and overlying thrombus using fibrin-targeted PFC NP. **Left:** an optical image of a human carotid endarterectomy sample shows moderate luminal narrowing and several atherosclerotic lesions. **Middle:** A ^{19}F projection image acquired through the entire thickness of carotid artery sample shows high ^{19}F signal along the lumen because of the binding of nanoparticles to fibrin. **Right:** The calculated concentration map of bound nanoparticles (nM) in the carotid sample based on ^{19}F signal intensity in each voxel. [Figure reprinted with permission from Morawski et al. (50)]

1.2.3 Cell Tracking using ^{19}F MRI of PFC NP

One important application of PFC nanoparticles as a ^{19}F MR imaging agent is cell tracking. Several cells types have been labeled with PFC NPs and *in vivo* tracking of these cells has been confirmed in preclinical models of heart ischemia (78), lung injury (79) and organ transplant (80), among others. Macrophages are the most widely studied cell type due to their role in inflammatory processes, and can be labeled with PFC NPs either through *in vitro* incubation or *in vivo* labeling in the blood stream. Macrophages internalize PFC NPs through endocytosis and actively home to the site of disease without an observable loss of bioactivity. ^{19}F MRI enables noninvasive measurement of macrophage recruitment, which is believed to be an essential indicator of the severity of inflammation (81). In addition to macrophages, stem cells (46) and dendritic cells (82) have been labeled and quantified with ^{19}F MRI of PFC NP. *In vivo* tracking of stem cells could provide a useful imaging approach for ongoing clinical trials of stem-cell therapy (Figure 1.8).

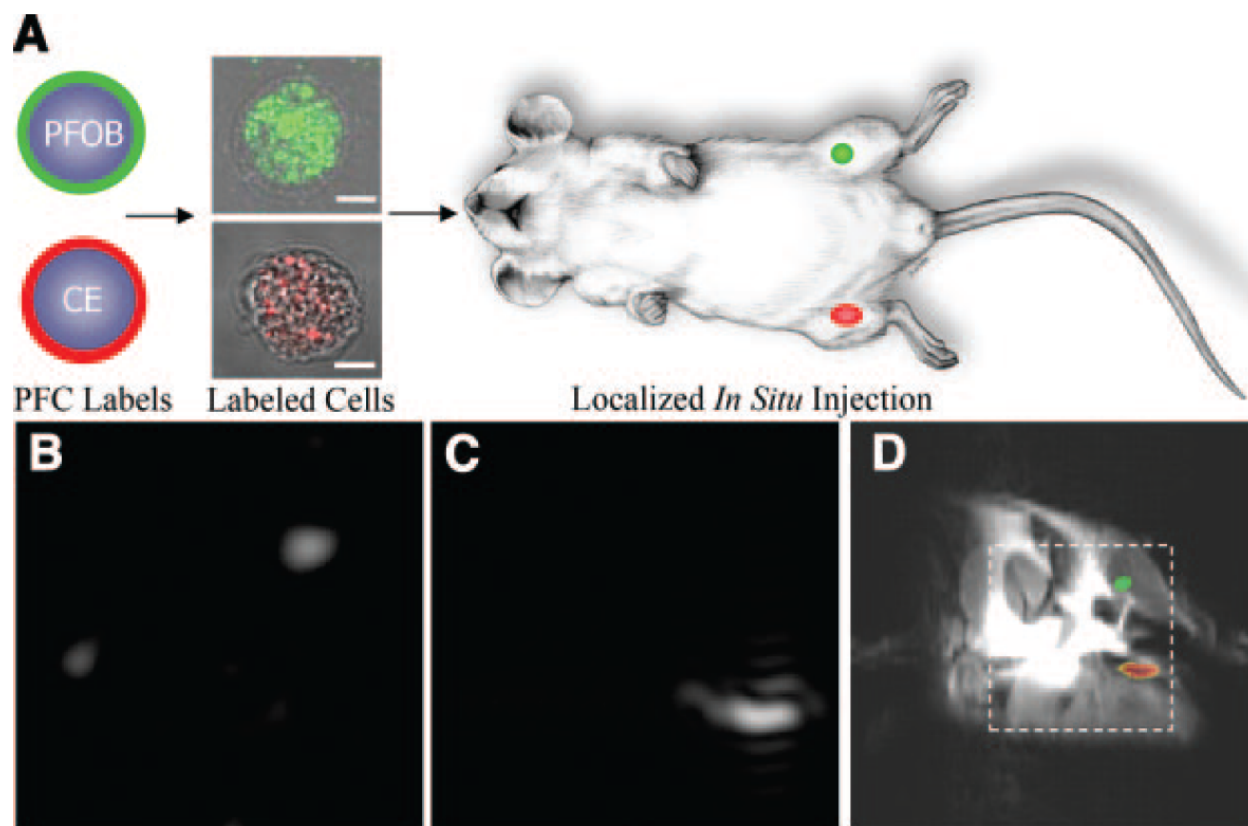


Figure 1.8 Localization of PFC NPs labeled cells in mice using ^{19}F MRI. (a) ^{19}F MRI trafficking of stem/progenitor cells labeled with either perfluorooctyl bromide (PFOB) (green) or perfluoropolyether (PFPE) (red) nanoparticles. Labeled cells were locally injected into the skeletal muscle of mouse thigh before MRI. (b)–(d) At 11.7-T field strength, ^{19}F spectral discrimination permits respective imaging of $\sim 1 \times 10^6$ PFOB-loaded cells (b) and PFPE-loaded cells (c). The composite ^{19}F (displayed in color) and ^1H (displayed in grayscale) images (d) reveal the location of PFOB labeled cells in the left leg and PFPE labeled cells in the right leg (dashed line indicates $3 \times 3 \text{ cm}^2$ field of view for ^{19}F images). [Figure reprinted with permission from Partlow et al. (46)]

1.3 Challenges of Quantitative ^{19}F MR Molecular Imaging

The imaging chain of a clinical MR system has many steps that may confound absolute signal calibration (Fig. 1.9). This is especially true for non-proton nuclei, for which specialized transmit/receive (T/R) coils must be used. For example, coil tuning and RF drive power (i.e., flip angle) settings must be calibrated and center frequency determined for tracers such as fluorine that are in miniscule concentrations lending little signal on which to perform these vital measures that drive not only image quality, but ultimately accuracy of quantification. In addition, the

spatial distribution of imaging labels in molecular imaging is generally heterogeneous, due to the intrinsically sparse expression pattern of pathological epitopes in tissue.

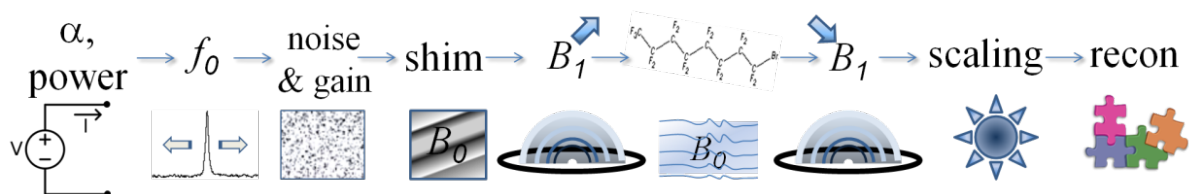


Figure 1.9 The imaging chain of a commercial MR scanner includes many steps in which measurements and adjustments are made, from determining the power settings for accurate flip angles, to B_0 shimming, to inhomogeneities in B_1 for RF transmit and receive; even during the scan eddy currents, B_0 variations, J-coupling, etc. can affect quantification outcomes.

Although interest in ^{19}F MR molecular imaging of PFC NPs has grown significantly over the past decade, this new imaging paradigm requires further technical advancement to overcome these challenges to bridge the gap between laboratory and clinic. Since there is little-to-no naturally occurring fluorine in the body, the available signal for ^{19}F MRI is principally limited by the administered dose of PFC NPs. Therefore, it is critical to improve imaging techniques by enhancing sensitivity of PFC NP detection at concentrations low enough for clinical translation (~ 1 ml/kg). Moreover, accurate quantification of PFC NPs *in vivo* requires image acquisition techniques that are robust against potential field inhomogeneities associated with clinical imaging systems (e.g. B_0 and B_1 field inhomogeneities). Finally, unlike ^1H atoms in water, ^{19}F atoms in perfluorocarbons experience more complicated chemical environments, which often result in large chemical shifts and scalar coupling (J-coupling) between different line groups.

1.3.1 Signal-to-Noise Ratio

Two major factors limit the potential signal-to-noise ratio (SNR) for ^{19}F MRI: the total number of ^{19}F imaging labels targeted to a particular site, and the small fraction of ^{19}F nuclear spins that generate a detectable MR signal, governed by Boltzmann statistics and magnetic field

strength. Several approaches have been proposed to overcome these limitations and improve SNR in ^{19}F MRI. Improving the sensitivity of the radio frequency (RF) coils, which transmit and receive the ^{19}F signal, is the most straightforward approach to increase SNR and subsequently improve image quality. It is necessary to design application-specific RF coils that are suited to particular imaging subjects, to avoid unnecessary signal loss. In addition to improved RF coils, choosing or designing an appropriate pulse sequence (i.e., the organization and timing of RF energy deposition, gradient application, and image formation) is also critical for optimizing ^{19}F imaging. Giraudeau et al. have recently shown that SNR can vary significantly (up to threefold differences) in ^{19}F MRI scans of fluorinated labels like PFOB depending on which sequences and parameters (e.g. echo time, or TE) are used (83).

1.3.2 Quantitative Imaging Artifacts

^{19}F MRI is potentially quantitative in nature because ^{19}F spin density (and signal) is linearly correlated to the deposition and resultant concentration PFC NPs at a particular site in the body. However, in most *in vivo* applications, several other factors come into play that may affect the accuracy of quantitative ^{19}F MR measurements. For example, the measured ^{19}F signal might not directly reflect ^{19}F concentration, but instead be convolved with image acquisition factors such as variable T_1 and T_2 relaxation characteristics within a perfluorocarbon molecule. Similar to ^1H MRI, ^{19}F is also susceptible to imaging artifacts, such as motion and eddy current artifacts, all of which can hamper image quality and can result in quantification errors (75). Lastly, and importantly for this work, ^{19}F quantification suffers from field inhomogeneities inherent to many transmit and receive RF coils. Since the concentration of PFC NPs at a site of disease measured with ^{19}F MR is determined by a comparison to an external standard of known

concentration, local differences in the B_1 (RF) field between the targeted region of interest and the location of the standard lead to errors in the quantified ^{19}F signal. Therefore, to achieve accurate and reproducible ^{19}F MRI measurements across different applications, it is necessary to implement robust correction methods and optimized, artifact-resistant pulse sequences.

1.3.3 Chemical Shift and J-coupling

Clinically useful perfluorocarbon molecules can exhibit more complicated nuclear magnetic resonance (NMR) spin characteristics, and hence ^{19}F MRI properties, than do protons with ^1H MRI. As noted in Table 1.3, NMR-detectable ^{19}F nuclei can be observed over a much wider spectral range (240 kHz) than ^1H (1.28 kHz) or other non-proton nuclei. Chemical shift is a term to describe how some nuclei resonate at different Larmor frequencies than others due to differing gyromagnetic ratios (inherent to the element), or in the case of PFC molecules, to describe how spins of the same isotope experiencing the same local magnetic field resonate at different frequencies due to varying molecular environments (i.e. chemical bonds). Many PFC molecules, like PFOB, contain ^{19}F nuclei that exhibit multiple chemical shifts, which can cause chemical shift artifacts along the readout gradient direction, and special reconstruction algorithms are needed to correct for these artifacts (75). Moreover, these PFC ^{19}F nuclei within different molecular environments can have strong interactions with each other, which results in a process called homonuclear scalar coupling, or J-coupling. J-coupling between different chemical groups in PFC molecules causes a T_2 -shortening behavior in spin echo MRI (i.e. J-modulation), which significantly reduces the detectable signal intensity for ^{19}F MRI. However, once an understanding of the underlying physics of these unique NMR properties of PFC NPs is

achieved, the resultant artifacts can be compensated, or even taken advantage of to expand ^{19}F MRI to new applications (84).

Table 1.3 NMR Spectral Ranges for Different Nuclei

Nucleus	Range (ppm)	Range (kHz at 3T) ^a
^1H	10	1.28
^{31}P	30	1.54
^{13}C	200	10.0
^{19}F	2000	240

^a Spectral ranges in kHz at 3T calculated from (85).

1.4 Dissertation Objective, Significance, and Organization

1.4.1 Objective

The objective of this thesis is to advance the state of the art for ^{19}F MR molecular imaging of perfluorocarbon nanoparticle emulsion contrast agents. To achieve this objective, three specific aims have been identified:

1. Create new tools and techniques for ^{19}F MR molecular imaging of PFC nanoparticles.
2. Develop translatable procedures for absolute quantification of ^{19}F nuclei with MR molecular imaging.
3. Evaluate the potential for clinical translation with *ex vivo* and *in vivo* preclinical experiments.

As the quantification of these PFC NP contrast agents becomes more widely used, the validity, accuracy, and repeatability of these metrics becomes essential to their clinical implementation. Robust, standardized techniques are developed in this work to improve the accuracy of quantitative MR molecular imaging, validate system performance, calibrate measurements to ensure repeatability of these quantitative metrics, and evaluate the potential for clinical translation. As these quantitative metrics become routine in medical imaging procedures, these standardized calibrations and techniques are expected to be critical for accurate

interpretation of underlying pathophysiology. This will also impact the development of new therapies and diagnostic techniques/agents by reducing the variability of image-based measurements, thereby increasing the impact of the studies and reducing the overall time and cost to translate new technologies into the clinic.

1.4.2 Significance and Innovation

In biomedical research, there is a clear and present need for repeatable, accurate quantitative imaging as is evidenced by the recent emphasis of many interdisciplinary committees on standardization for quantitative imaging. While true for all imaging modalities, this is particularly true for MRI and even more so for emerging ^{19}F MR molecular imaging applications where measuring biomarker concentrations accurately over time makes the difference between success and failure – success, for example, in drug development, clinical trials, or clinical diagnosis. Recently, NIST and others have jointly implemented traceable phantoms to test imaging systems with standardized approaches (86), which is vital for quantifying intra- and inter-lab variability in imaging. Characterizing system stability (or identifying problems and having service engineers correct malfunctions) is useful for robust signal analysis and time-resolved signal changes as is needed for first-pass dynamic contrast enhancement (DCE). However, characterizing signal stability is not the same as calibrating accurate derived values such as concentrations of site-targeted contrast agents, and it does not necessarily incorporate system-specific and patient-specific settings such as power settings and field inhomogeneity corrections. This work addresses both the validation of MR system performance specifications and correction techniques, both prospectively and retrospectively, with the ultimate goal of accurate, repeatable quantification in MRI. Furthermore, it expands on

the current efforts in the area of DCE to include imaging and spectroscopy of multiple nuclei other than hydrogen.

The innovative aspect of this work is in the creation of novel techniques to calibrate ^{19}F MR molecular imaging of PFC NP emulsions where there is a low expected concentration of the agent. Advanced dual-tuned $^{19}\text{F}/^1\text{H}$ RF coils are used so that coil-specific (and, therefore, anatomy-specific) calibrations can be performed on the ^1H signal, and directly ported to the nuclear signal of the test agent (e.g., ^{19}F), regardless of its location or concentration. Fast, automatable methods will be established to increase quantitative MR molecular imaging accuracy, precision, and repeatability. Importantly, this capability has the potential to be translated into user-friendly applications for clinical diagnosis and therapy monitoring. These tools, based on high-performance, readily available clinical imaging systems, will be directly implemented for pre-clinical and clinical trials, potentially increasing the efficiency and effectiveness of future translational research.

1.4.3 Organization

In Chapter 2, the underlying principles behind ^{19}F NMR physics and image acquisition are explored, as well as the unique properties of $^{19}\text{F}/^1\text{H}$ dual-tuned RF coils. First, the NMR physics governing all magnetically susceptible nuclear spins is reviewed, and distinctions are drawn between ^1H atoms and ^{19}F nuclei. Then, resultant magnetic resonance properties of ^{19}F spins, such as J-coupling, are examined, along with their effect on perfluorocarbon molecules like PFOB. Next, the theory behind image acquisition with $^{19}\text{F}/^1\text{H}$ dual-tuned RF coils is considered, which includes a coupled resonator model with appropriate impedance matching to create two distinct resonant peaks for each nuclei. This enables truly simultaneous acquisition of

the ^1H and ^{19}F signals, yielding co-registered images of anatomy and function. A new dual-tuned single-turn-solenoid RF coil is designed and constructed to open up new applications to this simultaneous imaging. Experimental results with this new coil are then presented, including bench tests of electromagnetic performance, as well as phantom and *in vivo* imaging capabilities.

Chapter 3 introduces a new pulse sequence, termed “balanced UTE-SSFP”, for highly sensitive ^{19}F MR imaging of agents with complex spectra. The NMR properties of molecules with non-proton nuclei such as PFOB are first discussed to understand their broad chemical shifts and complex relaxation characteristics. Then, the CF_2 spectral peak signatures of PFOB are modeled, which contain 12 of the 17 available ^{19}F nuclei in the molecule. This line group quickly dephases and decays due to T_2 relaxation, yet can be utilized if acquired quickly.

A new 3D $^{19}\text{F}/^1\text{H}$ pulse sequence is then designed and implemented to capture these CF_2 resonances, which consists of $^{19}\text{F}/^1\text{H}$ RF excitation using FID acquisition at an ultra-short echo time (UTE) and a balanced steady-state free precession (SSFP) gradient scheme with a Wong-type radial readout trajectory. The sensitivity of this new balanced UTE-SSFP pulse sequence is compared to existing sequences with the use of an imaging phantom, and shown to have a sensitivity twofold better than other sequences. Finally, *in vivo* imaging of angiogenesis-targeted PFOB nanoparticles is demonstrated in a rabbit model of cancer on a clinical 3T scanner, to validate the translational potential for the new pulse sequence.

In Chapter 4, a new approach to overcome challenges for accurate *in vivo* quantitative ^{19}F MR molecular imaging is presented, which includes flip angle calibration between the relevant ^1H and ^{19}F nuclei of interest, as well as B_1 -mapping compensation to offset expected RF inhomogeneities. A disparity in the required power settings of $^{19}\text{F}/^1\text{H}$ dual-tuned RF coils to achieve optimum flip angles for the ^{19}F and ^1H nuclei is first reported and investigated. Then, an

approach to remediate this difference in requisite power settings is proposed and tested, which involves a coil-specific, but spatially independent calibration ratio for each coil. This strategy permits determination of the optimum power setting for the ^{19}F nuclei, which are typically sparse at least at the beginning of a typical imaging experiment, by utilizing the abundant ^1H signal as a reference.

Another challenge to accurate quantitative ^{19}F MRI involves inhomogeneous RF (B_1) fields produced by many RF coils. A solution is proposed that entails mapping this B_1 field and performing an image-based correction using a signal model of the acquisition technique, which is tested in phantom and *in vivo* experiments in a rabbit model of cancer.

Chapter 5 examines two *in vivo* applications of ^{19}F MR molecular imaging at 3T. First, a new technique to image renal perfusion in acute kidney injury (AKI) at clinically relevant field strengths is presented. A model of AKI is implemented in rats by ligation and occlusion of the left renal artery, followed by reperfusion. Renal perfusion is then imaged at 3T with a $^{19}\text{F}/^1\text{H}$ dual-tuned coil after administration of PFC NPs via the tail vein. These *in vivo* results are confirmed with *ex vivo* imaging of excised kidneys, also at 3T. Next, the impact of diet-induced atherosclerotic plaque erosions is investigated with quantitative ^{19}F MRI of a hyperlipidemic rabbit model *in vivo*. A method is introduced and tested that seeks to visualize nontargeted PFC nanoparticles that accumulate passively in the intimal plaque regions of the rabbit aorta as a consequence of endothelial erosions and vascular barrier disruption with the use of ^{19}F MR molecular imaging combined with saturation bands to eliminate signal from the flowing blood pool, which allows ^{19}F imaging of the vessel wall itself.

Chapter 6 investigates the potential use of ^{19}F MR molecular imaging at 3T in the clinic with a pilot study of atherosclerosis imaging using nontargeted PFC NP in human tissue

specimens. Initial imaging results in a phantom and an amputated human lower limb are presented, which show promise for the use of ^{19}F imaging in human atherosclerosis imaging in the future.

In Chapter 7, the major findings of the thesis are summarized and the main conclusions that are drawn from the work are contextualized. Future directions for the work are suggested, which include other potential clinical applications of ^{19}F MR molecular imaging in humans.

1.5 References

1. Gallagher FA. An introduction to functional and molecular imaging with MRI. *Clin Radiol* 2010;65(7):557-566.
2. Saraste A, Nekolla S, Schwaiger M. Contrast-enhanced magnetic resonance imaging in the assessment of myocardial infarction and viability. *J Nucl Cardiol* 2008;15(1):105-117.
3. Schlaug G, Siewert B, Benfield A, Edelman RR, Warach S. Time course of the apparent diffusion coefficient (ADC) abnormality in human stroke. *Neurology* 1997;49(1):113-119.
4. Pennell DJ. Cardiovascular magnetic resonance. *Circulation* 2010;121(5):692-705.
5. Tofts PS, Brix G, Buckley DL, Evelhoch JL, Henderson E, Knopp MV, Larsson HB, Lee TY, Mayr NA, Parker GJ, Port RE, Taylor J, Weisskoff RM. Estimating kinetic parameters from dynamic contrast-enhanced T(1)-weighted MRI of a diffusable tracer: standardized quantities and symbols. *J Magn Reson Imaging* 1999;10(3):223-232.

6. Lanza GM, Winter PM, Caruthers SD, Hughes MS, Hu G, Schmieder AH, Wickline SA. Theragnostics for tumor and plaque angiogenesis with perfluorocarbon nanoemulsions. *Angiogenesis* 2010;13(2):189-202.
7. Weissleder R, Mahmood U. Molecular imaging. *Radiology* 2001;219(2):316-333.
8. Piwnica-Worms DR. Introduction to molecular imaging. *J Am Coll Radiol* 2004;1(1 Suppl):2-3.
9. Caruthers SD, Wickline SA, Lanza GM. Targeted Nanoparticles for Molecular Imaging and Therapy: A Multi-Modality Approach to Molecular Medicine. In: Spekowius G, Wendler T, editors. *Advances in Healthcare Technology*. Volume 6. Dordrecht, the Netherlands: Springer; 2006. p 305-322.
10. Gross S, Piwnica-Worms D. Molecular imaging strategies for drug discovery and development. *Curr Opin Chem Biol* 2006;10(4):334-342.
11. Caruthers SD, Wickline SA, Lanza GM. Nanotechnological applications in medicine. *Curr Opin Biotech* 2007;18(1):26-30.
12. Lanza G, Lorenz C, Fischer S, Scott M, Cacheris W, Kaufman R, Gaffney P, Wickline S. Enhanced detection of thrombi with a novel fibrin-targeted magnetic resonance imaging agent. *Acad Radiol* 1998;5(suppl 1):s173-s176.
13. Anderson SA, Rader RK, Westlin WF, Null C, Jackson D, Lanza GM, Wickline SA, Kotyk JJ. Magnetic resonance contrast enhancement neovasculature with $\alpha\beta 3$ -targeted nanoparticles. *Magn Reson Med* 2000;44(3):433-439.
14. Yang L, Mao H, Wang YA, Cao Z, Peng X, Wang X, Duan H, Ni C, Yuan Q, Adams G, Smith MQ, Wood WC, Gao X, Nie S. Single chain epidermal growth factor receptor

- antibody conjugated nanoparticles for in vivo tumor targeting and imaging. *Small* 2009;5(2):235-243.
15. Southworth R, Kaneda M, Chen J, Zhang L, Zhang H, Yang X, Razavi R, Lanza G, Wickline SA. Renal vascular inflammation induced by Western diet in ApoE-null mice quantified by ¹⁹F NMR of VCAM-1 targeted nanobeacons. *Nanomed-Nanotechnol* 2009;5(3):359-367.
 16. Winter P, Caruthers S, Fuhrhop R, Allen J, Williams T, Harris T, Wickline S, Lanza G. Serial Delivery and Assessment of Targeted Anti-Angiogenic Therapy against Atherosclerosis. *J Cardio Magn Reson* 2007;9(2):350.
 17. Cai W, Chen X. Multimodality molecular imaging of tumor angiogenesis. *J Nucl Med* 2008;49 Suppl 2:113S-128S.
 18. Schmieder AH, Winter PM, Williams TA, Allen JS, Hu G, Zhang H, Caruthers SD, Wickline SA, Lanza GM. MR Molecular Imaging of Neovasculature May Predict Response to Antiangiogenic Therapy in Animal Cancer Models. In *Proc Intl Soc Mag Reson Med*, 2008. p. 799.
 19. Le Bihan D, Mangin JF, Poupon C, Clark CA, Pappata S, Molko N, Chabriat H. Diffusion tensor imaging: concepts and applications. *J Magn Reson Imaging* 2001;13(4):534-546.
 20. Kalman FK, Woods M, Caravan P, Jurek P, Spiller M, Tircso G, Kiraly R, Brucher E, Sherry AD. Potentiometric and relaxometric properties of a gadolinium-based MRI contrast agent for sensing tissue pH. *Inorg Chem* 2007;46(13):5260-5270.
 21. Ogawa S, Lee TM, Kay AR, Tank DW. Brain magnetic resonance imaging with contrast dependent on blood oxygenation. *P Natl Acad Sci USA* 1990;87(24):9868-9872.

22. Choudhury RP, Fuster V, Fayad ZA. Molecular, cellular and functional imaging of atherothrombosis. *Nat Rev Drug Discov* 2004;3(11):913-925.
23. Benaron DA. The future of cancer imaging. *Cancer Metastasis Rev* 2002;21(1):45-78.
24. Williams DS, Detre JA, Leigh JS, Koretsky AP. Magnetic resonance imaging of perfusion using spin inversion of arterial water. *P Natl Acad Sci USA* 1992;89(1):212-216.
25. Harisinghani MG, Barentsz J, Hahn PF, Deserno WM, Tabatabaei S, van de Kaa CH, de la Rosette J, Weissleder R. Noninvasive detection of clinically occult lymph-node metastases in prostate cancer. *N Engl J Med* 2003;348(25):2491-2499.
26. Pautler RG, Silva AC, Koretsky AP. In vivo neuronal tract tracing using manganese-enhanced magnetic resonance imaging. *Magn Reson Med* 1998;40(5):740-748.
27. Ward KM, Aletras AH, Balaban RS. A new class of contrast agents for MRI based on proton chemical exchange dependent saturation transfer (CEST). *J Magn Reson* 2000;143(1):79-87.
28. Zhou J, Lal B, Wilson DA, Laterra J, van Zijl PC. Amide proton transfer (APT) contrast for imaging of brain tumors. *Magn Reson Med* 2003;50(6):1120-1126.
29. Jones CK, Schlosser MJ, van Zijl PC, Pomper MG, Golay X, Zhou J. Amide proton transfer imaging of human brain tumors at 3T. *Magn Reson Med* 2006;56(3):585-592.
30. Regatte RR, Akella SV, Borthakur A, Kneeland JB, Reddy R. In vivo proton MR three-dimensional T1rho mapping of human articular cartilage: initial experience. *Radiology* 2003;229(1):269-274.
31. Levitt M. *Spin Dynamics: Basics of Nuclear Magnetic Resonance*. Hoboken, NJ: John Wiley & Sons; 2008. 740 p.

32. Ackerman JJH. Course Lecture. CHEM 576 "Magnetic Resonance". 2010.
33. Maril N, Rosen Y, Reynolds GH, Ivanishev A, Ngo L, Lenkinski RE. Sodium MRI of the human kidney at 3 Tesla. *Magn Reson Med* 2006;56(6):1229-1234.
34. Zhang J, Wilke N, Wang Y, Zhang Y, Wang C, Eijgelshoven MH, Cho YK, Murakami Y, Ugurbil K, Bache RJ, From AH. Functional and bioenergetic consequences of postinfarction left ventricular remodeling in a new porcine model. MRI and 31 P-MRS study. *Circulation* 1996;94(5):1089-1100.
35. Li X, Majumdar S. Quantitative MRI of articular cartilage and its clinical applications. *J Magn Reson Imaging* 2013;38(5):991-1008.
36. Fan X, River JN, Muresan AS, Popescu C, Zamora M, Culp RM, Karczmar GS. MRI of perfluorocarbon emulsion kinetics in rodent mammary tumours. *Phys Med Biol* 2006;51(2):211-220.
37. Kurhanewicz J, Bok R, Nelson SJ, Vigneron DB. Current and potential applications of clinical ¹³C MR spectroscopy. *J Nucl Med* 2008;49(3):341-344.
38. Keshari KR, Sai V, Wang ZJ, Vanbrocklin HF, Kurhanewicz J, Wilson DM. Hyperpolarized [1-¹³C]dehydroascorbate MR spectroscopy in a murine model of prostate cancer: comparison with ¹⁸F-FDG PET. *J Nucl Med* 2013;54(6):922-928.
39. Weast RC. CRC handbook of chemistry and physics. Cleveland, OH: CRC Press; 1988.
40. Reid DG, Murphy PS. Fluorine magnetic resonance in vivo: a powerful tool in the study of drug distribution and metabolism. *Drug Discov Today* 2008;13(11-12):473-480.
41. Ahrens ET, Flores R, Xu HY, Morel PA. In vivo imaging platform for tracking immunotherapeutic cells. *Nat Biotechnol* 2005;23(8):983-987.

42. Chen J, Lanza GM, Wickline SA. Quantitative magnetic resonance fluorine imaging: today and tomorrow. *Wiley Interdiscip Rev Nanomed Nanobiotechnol* 2010;2(4):431-440.
43. Foster MA. *Magnetic resonance in medicine and biology*. New York, NY: Pergamon Press; 1984. xi, 244 p. p.
44. Kaneda MM, Caruthers S, Lanza GM, Wickline SA. Perfluorocarbon nanoemulsions for quantitative molecular imaging and targeted therapeutics. *Ann Biomed Eng* 2009;37(10):1922-1933.
45. Wickline SA, Mason RP, Caruthers SD, Chen J, Winter PM, Hughes MS, Lanza GM. Fluorocarbon Agents for Quantitative Multimodal Molecular Imaging and Targeted Therapeutics. In: Weissleder R, Ross BD, Rehemtulla A, Gambhir SS, editors. *Molecular Imaging: Principles and Practice*: McGraw-Hill; 2010.
46. Partlow KC, Chen J, Brant JA, Neubauer AM, Meyerrose TE, Creer MH, Nolte JA, Caruthers SD, Lanza GM, Wickline SA. ¹⁹F magnetic resonance imaging for stem/progenitor cell tracking with multiple unique perfluorocarbon nanobeacons. *FASEB J* 2007;21(8):1647-1654.
47. Neubauer AM, Caruthers SD, Hockett FD, Cyrus T, Robertson JD, Allen JS, Williams TD, Fuhrhop RW, Lanza GM, Wickline SA. Fluorine cardiovascular magnetic resonance angiography in vivo at 1.5 T with perfluorocarbon nanoparticle contrast agents. *J Cardiovasc Magn Reson* 2007;9(3):565-573.
48. Neubauer AM, Partlow KC, Caruthers SD, Brant J, Hockett FD, Chen J, Nolte J, Lanza GM, Wickline SA. Endothelial stem cell detection in vivo with unique perfluorocarbon

- nanoparticle labels using fluorine (F-19) MRI at 1.5 T. *Circulation* 2006;114(18):251-251.
49. Caruthers SD, Neubauer AM, Hockett FD, Lamerichs R, Winter PM, Scott MJ, Gaffney PJ, Wickline SA, Lanza GM. In vitro demonstration using ¹⁹F magnetic resonance to augment molecular imaging with paramagnetic perfluorocarbon nanoparticles at 1.5 tesla. *Invest Radiol* 2006;41(3):305-312.
 50. Morawski AM, Winter PM, Yu X, Fuhrhop RW, Scott MJ, Hockett F, Robertson JD, Gaffney PJ, Lanza GM, Wickline SA. Quantitative "magnetic resonance immunohistochemistry" with ligand-targeted ¹⁹F nanoparticles. *Magn Reson Med* 2004;52(6):1255-1262.
 51. Wickline SA, Neubauer AM, Winter P, Caruthers S, Lanza G. Applications of nanotechnology to atherosclerosis, thrombosis, and vascular biology. *Arterioscl Thromb Vas* 2006;26(3):435-441.
 52. Pan H, Soman NR, Schlesinger PH, Lanza GM, Wickline SA. Cytolytic peptide nanoparticles ('NanoBees') for cancer therapy. *Wiley Interdiscip Rev Nanomed Nanobiotechnol* 2011;3(3):318-327.
 53. Caruthers SD, Cyrus T, Winter PM, Wickline SA, Lanza GM. Anti-angiogenic perfluorocarbon nanoparticles for diagnosis and treatment of atherosclerosis. *Wiley Interdiscip Rev Nanomed Nanobiotechnol* 2009;1(3):311-323.
 54. Winter PM, Caruthers SD, Kassner A, Harris TD, Chinen LK, Allen JS, Lacy EK, Zhang H, Robertson JD, Wickline SA, Lanza GM. Molecular imaging of angiogenesis in nascent Vx-2 rabbit tumors using a novel $\alpha v\beta 3$ -targeted nanoparticle and 1.5 Tesla magnetic resonance imaging. *Cancer Res* 2003;63(18):5838-5843.

55. Lijowski M, Caruthers S, Hu G, Zhang HY, Scott MJ, Williams T, Erpelding T, Schmieder AH, Kiefer G, Gulyas G, Athey PS, Gaffney PJ, Wickline SA, Lanza GM. High Sensitivity High-Resolution SPECT-CT/MR Molecular Imaging of Angiogenesis in the Vx2 Model. *Invest Radiol* 2009;44(1):15-22.
56. Winter PM, Caruthers SD, Yu X, Song SK, Chen J, Miller B, Bulte JWM, Robertson JD, Gaffney PJ, Wickline SA, Lanza GM. Improved molecular imaging contrast agent for detection of human thrombus. *Magn Reson Med* 2003;50(2):411-416.
57. Schmieder AH, Caruthers SD, Zhang H, Williams TA, Robertson JD, Wickline SA, Lanza GM. Three-dimensional MR mapping of angiogenesis with $\alpha 5\beta 1(\alpha v\beta 3)$ -targeted theranostic nanoparticles in the MDA-MB-435 xenograft mouse model. *FASEB J* 2008;22(12):4179-4189.
58. Winter PM, Caruthers SD, Allen JS, Cai K, Williams TA, Lanza GM, Wickline SA. Molecular imaging of angiogenic therapy in peripheral vascular disease with $\alpha v\beta 3$ -integrin-targeted nanoparticles. *Magn Reson Med* 2010;64(2):369-376.
59. Schmieder AH, Winter PM, Caruthers SD, Harris TD, Williams TA, Allen JS, Lacy EK, Zhang H, Scott MJ, Hu G, Robertson JD, Wickline SA, Lanza GM. Molecular MR imaging of melanoma angiogenesis with $\alpha v\beta 3$ -targeted paramagnetic nanoparticles. *Magn Reson Med* 2005;53(3):621-627.
60. Hu G, Lijowski M, Zhang H, Partlow KC, Caruthers SD, Kiefer G, Gulyas G, Athey P, Scott MJ, Wickline SA, Lanza GM. Imaging of Vx-2 rabbit tumors with $\alpha v\beta 3$ - integrin-targeted ^{111}In nanoparticles. *Int J Cancer* 2007;120(9):1951-1957.
61. Schmieder AH, Williams TA, Allen JS, Hu G, Zhang H, Caruthers SD, Wickline SA, Lanza GM. High-Resolution 3D MRI Mapping of Tumor Angiogenesis using $\alpha 5\beta 1$ -

- Targeted Perfluorocarbon Nanoparticles. In Proceedings of the 15th Annual Meeting of ISMRM, Berlin, Germany, 2007. p. 1187.
62. Schmieder AH, Williams TA, Allen JS, Hu G, Zhang H, Caruthers SD, Wickline SA, Lanza GM. Time-Resolved Molecular Imaging of the “Angiogenic Switch” in Animal Models of Cancer. In Proc Intl Soc Mag Reson Med, 2008. p. 14.
 63. Winter PM, Schmieder AH, Caruthers SD, Keene JL, Zhang H, Wickline SA, Lanza GM. Minute dosages of $\alpha v \beta 3$ -targeted fumagillin nanoparticles impair Vx-2 tumor angiogenesis and development in rabbits. FASEB J 2008;22(8):2758-2767.
 64. Soman NR, Baldwin SL, Hu G, Marsh JN, Lanza GM, Heuser JE, Arbeit JM, Wickline SA, Schlesinger PH. Molecularly targeted nanocarriers deliver the cytolytic peptide melittin specifically to tumor cells in mice, reducing tumor growth. J Clin Invest 2009;119(9):2830-2842.
 65. Winter PM, Morawski AM, Caruthers SD, Fuhrhop RW, Zhang H, Williams TA, Allen JS, Lacy EK, Robertson JD, Lanza GM, Wickline SA. Molecular imaging of angiogenesis in early-stage atherosclerosis with $\alpha v \beta 3$ -integrin-targeted nanoparticles. Circulation 2003;108(18):2270-2274.
 66. Winter PM, Neubauer AM, Caruthers SD, Harris TD, Robertson JD, Williams TA, Schmieder AH, Hu G, Allen JS, Lacy EK, Zhang H, Wickline SA, Lanza GM. Endothelial $\alpha v \beta 3$ integrin-targeted fumagillin nanoparticles inhibit angiogenesis in atherosclerosis. Arterioscl Throm Vas 2006;26(9):2103-2109.
 67. Winter PM, Caruthers SD, Zhang HY, Williams TA, Wickline SA, Lanza GM. Antiangiogenic Synergism of Integrin-Targeted Fumagillin Nanoparticles and Atorvastatin in Atherosclerosis. JACC Cardiovasc Imaging 2008;1(5):624-634.

68. Boles KS, Schmieder AH, Koch AW, Carano RAD, Wu Y, Caruthers SD, Tong RK, Stawicki S, Hu G, Scott MJ, Zhang H, Reynolds BA, Wickline SA, Lanza GM. MR angiogenesis imaging with Robo4- vs. $\alpha\beta 3$ -targeted nanoparticles in a B16/F10 mouse melanoma model. *FASEB J* 2010;24(11):4262-4270.
69. Pan D, Caruthers SD, Hu G, Senpan A, Scott MJ, Gaffney PJ, Wickline SA, Lanza GM. Ligand-directed nanobialys as theranostic agent for drug delivery and manganese-based magnetic resonance imaging of vascular targets. *J Am Chem Soc* 2008;130(29):9186-9187.
70. Morawski AM, Lanza GA, Wickline SA. Targeted contrast agents for magnetic resonance imaging and ultrasound. *Curr Opin Biotech* 2005;16(1 SPEC. ISS.):89-92.
71. Sadowski EA, Bennett LK, Chan MR, Wentland AL, Garrett AL, Garrett RW, Djamali A. Nephrogenic systemic fibrosis: risk factors and incidence estimation. *Radiology* 2007;243(1):148-157.
72. Boyd AS, Zic JA, Abraham JL. Gadolinium deposition in nephrogenic fibrosing dermopathy. *J Am Acad Dermatol* 2007;56(1):27-30.
73. Grobner T. Gadolinium—a specific trigger for the development of nephrogenic fibrosing dermopathy and nephrogenic systemic fibrosis? *Nephrol Dial Transplant* 2006;21(4):1104-1108.
74. Aspelin P, Aubry P, Fransson SG, Strasser R, Willenbrock R, Berg KJ, Nephrotoxicity in High-Risk Patients Study of I-O, Low-Osmolar Non-Ionic Contrast Media Study I. Nephrotoxic effects in high-risk patients undergoing angiography. *N Engl J Med* 2003;348(6):491-499.

75. Keupp J, Rahmer J, Grässlin I, Mazurkewitz PC, Schaeffter T, Lanza GM, Wickline SA, Caruthers SD. Simultaneous dual-nuclei imaging for motion corrected detection and quantification of ¹⁹F imaging agents. *Magn Reson Med* 2011;66(4):1116-1122.
76. Zhang H, Zhang L, Myerson J, Bibee K, Scott M, Allen J, Sicard G, Lanza G, Wickline S. Quantifying the evolution of vascular barrier disruption in advanced atherosclerosis with semipermeant nanoparticle contrast agents. *Plos One* 2011;6(10):e26385.
77. Waters EA, Chen J, Yang X, Zhang H, Neumann R, Santeford A, Arbeit J, Lanza GM, Wickline SA. Detection of targeted perfluorocarbon nanoparticle binding using ¹⁹F diffusion weighted MR spectroscopy. *Magn Reson Med* 2008;60(5):1232-1236.
78. Flogel U, Ding Z, Hardung H, Jander S, Reichmann G, Jacoby C, Schubert R, Schrader J. In vivo monitoring of inflammation after cardiac and cerebral ischemia by fluorine magnetic resonance imaging. *Circulation* 2008;118(2):140-148.
79. Ebner B, Behm P, Jacoby C, Burghoff S, French BA, Schrader J, Flogel U. Early assessment of pulmonary inflammation by ¹⁹F MRI in vivo. *Circ Cardiovasc Imaging* 2010;3(2):202-210.
80. Hitchens TK, Ye Q, Eytan DF, Janjic JM, Ahrens ET, Ho C. ¹⁹F MRI detection of acute allograft rejection with in vivo perfluorocarbon labeling of immune cells. *Magn Reson Med* 2011;65(4):1144-1153.
81. Kadayakkara DK, Ranganathan S, Young WB, Ahrens ET. Assaying macrophage activity in a murine model of inflammatory bowel disease using fluorine-19 MRI. *Lab Invest* 2012;92(4):636-645.
82. Waiczies H, Lepore S, Janitzek N, Hagen U, Seifert F, Ittermann B, Purfurst B, Pezzutto A, Paul F, Niendorf T, Waiczies S. Perfluorocarbon particle size influences magnetic

- resonance signal and immunological properties of dendritic cells. *Plos One* 2011;6(7):e21981.
83. Giraudeau C, Flament J, Marty B, Boumezbeur F, Meriaux S, Robic C, Port M, Tsapis N, Fattal E, Giacomini E, Lethimonnier F, Le Bihan D, Valette J. A new paradigm for high-sensitivity ¹⁹F magnetic resonance imaging of perfluorooctylbromide. *Magn Reson Med* 2010;63(4):1119-1124.
84. Yu JX, Kodibagkar VD, Cui WN, Mason RP. F-19: A versatile reporter for non-invasive physiology and pharmacology using magnetic resonance. *Curr Med Chem* 2005;12(7):819-848.
85. Systems PM. *Basic Principles of MR Imaging*. Eindhoven, North Brabant, The Netherlands 1993. p 139.
86. Karam LR. Measurement traceability in medical physics. *J Med Phys* 2014;39(1):1-3.

Chapter 2. Principles of ^{19}F NMR Physics and Image Acquisition

with $^{19}\text{F}/^1\text{H}$ Dual-Tuned RF Coils

2.1 Principles of ^{19}F NMR Physics

2.1.1 NMR Background

To further understand the principles underlying ^{19}F nuclear magnetic resonance (NMR) physics, the basic concepts behind the NMR experiment will be summarized. As first theorized by Wolfgang Pauli, certain nuclei (collection of protons and neutrons at the core of an atom) possess an inherent angular momentum, or spin. All nuclei (or ‘spins’, which will be used here interchangeably) with an uneven atomic number have a characteristic spin quantum number (I) greater than zero. The spinning nature of these nuclei induces a magnetic field coincident with the axis of spin, and can be viewed as a magnetic moment (μ) (1). These magnetic moments can be imagined as tiny bar magnets that have the potential to interact with other magnetic fields.

Normally, the magnetic moments in a collection of nuclei will be randomly oriented, as determined by the principles of Brownian motion. However, when a static magnetic field is applied, these spins align either with (parallel) or against (antiparallel) the direction of the applied field. These orientations correspond to quantum mechanical energy states, with the number of energy levels being determined by the spin quantum number, I . As listed in Table 1.1, nuclei with $I = 1/2$ (e.g. ^1H , ^{19}F , ^{31}P , and ^{13}C) and $I = 3/2$ (e.g. ^{23}Na) have a net nuclear spin and are detectable by NMR (2).

In the presence of an applied magnetic field (B_0), the nuclear spins experience a torque, which causes them to rotate around the axis of the applied field with a precise frequency. This rotation, similar to the rotation of a spinning top in the presence of Earth’s gravitational field, is

called Larmor precession. The rate of precession is dependent on the specific physical characteristics of the isotope involved and the strength of the applied magnetic field, which is expressed as

$$\omega = \gamma * B_0 \quad [2.1]$$

where ω is the Larmor or resonance frequency (MHz), γ is a constant of proportionality (gyromagnetic or magnetogyric ratio) specific to the nucleus involved, and B_0 is the magnetic field strength measured in tesla (T) (3). Larmor precession is a resonance phenomenon, meaning a system of nuclei has a natural resonance, or frequency of oscillation, at which energy can be most efficiently transferred to the system. With a gyromagnetic ratio of 42.58 MHz/T, ^1H nuclei precess at 127.8 MHz at 3T, while the resonance frequency of ^{19}F nuclei ($\gamma = 40.08$ MHz/T) is 120.2 MHz (6% different). Therefore, ^1H and ^{19}F nuclei can be manipulated using electromagnetic energy at those specific frequencies, which lie in the radiofrequency (RF) spectrum (4).

When an external magnetic field is applied to a collection of nuclei, the parallel- or antiparallel-aligning spins have a nearly identical probability of occupying either orientation at room temperature. Luckily, however, there is a *slight* excess favoring the parallel (low-energy) orientation, only about 15 parts per million (ppm) with a 1.5 T magnetic field at 300 K, governed by the Boltzman distribution. This inequity between the two alignments contributes to the NMR signal, yielding a bulk magnetization (M), which although rather weak, can be strengthened by increasing the magnetic field (B_0) to 3T (or to higher field strengths such as 4.7T, 7T, or 11.7T).

To obtain information about the spins, they must be perturbed or excited, to induce a current in an RF coil by Faraday's law of induction. This is achieved by irradiating the spin system with an RF pulse, which is a short burst of radio frequency energy matching the Larmor

frequency of the nuclei of interest. In a rotating frame of reference (since the spins are precessing about the B_0 field in reality), this RF excitation pulse can be represented by an additional magnetic field (B_1), which is perpendicular to B_0 . This B_1 field rotates or ‘tips’ the initial magnetization (M_0) away from the longitudinal direction along B_0 and into the transverse plane (M_{xy}), at an angle that is a function of the amplitude and duration of the applied RF pulse, expressed as

$$\theta = \gamma * B_1 * t \quad [2.2]$$

where θ is the angle of rotation, B_1 is the amplitude of the RF pulse, γ is the gyromagnetic ratio, and t is the duration of the RF pulse. The angle of rotation, θ , is commonly referred to as the RF flip angle (FA), and careful consideration must be made to achieve accurate flip angles for quantitative ^{19}F MR (as seen in Chapter 4). The energy required to tip a nucleus is defined by the Planck equation:

$$E = h * \nu \quad [2.3]$$

where h is Planck’s constant (6.62×10^{-34} J-s), and ν is the frequency of the spin. This suggests that different energy, and hence coil power, might be required for ^1H and ^{19}F spins.

After excitation, the nuclei return to equilibrium, losing energy by emitting electromagnetic radiation and by transferring energy to the lattice or between them. This process is called relaxation and begins immediately after the RF pulse ends. During this relaxation process, both the longitudinal (M_z) and transverse (M_{xy}) components of the net magnetization return to their equilibrium values, when M_z is equal to the initial M_0 . These relaxation processes are independent of one another, and the transverse magnetization always disappears before, sometimes long before, the longitudinal magnetization is restored.

The time constant that describes how M_z returns to its equilibrium value is called the longitudinal (spin-lattice) relaxation time (T_1) (Figure 2.1, left), which is described in the following equation:

$$M_z = M_0(1 - e^{-t/T_1}). \quad [2.4]$$

The time constant that describes the return of the transverse magnetization (M_{xy}) to equilibrium is called the transverse (spin-spin) relaxation time (T_2) (Figure 2.1, right), which is described in the following equation:

$$M_{xy} = M_{xy,0} * e^{-t/T_2}. \quad [2.5]$$

The spin-spin relaxation time (T_2) is a result of the transfer of energy between nuclei in different energy states, as one nucleus absorbs energy from a neighboring nucleus. These interactions between individual spins create local magnetic field variations, which results in a gradual dephasing of the spins causing a decay in the magnitude of the transverse component of the net magnetization. This process is also sensitive to inhomogeneities in the applied magnetic field, which when combined with the exponential decay of spin-spin relaxation, is referred to as T_2^* , the effective transverse relaxation time (always smaller than T_2).

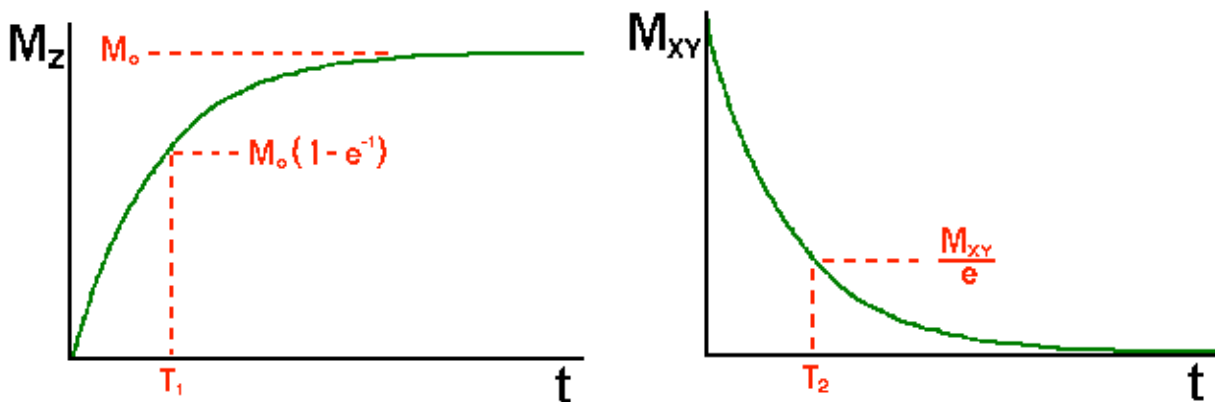


Figure 2.1 Left: Longitudinal (spin-lattice) relaxation, described by T_1 relaxation time. Right: Transverse (spin-spin) relaxation, described by T_2 relaxation time.

In a typical NMR measurement, the application of a 90° RF pulse causes the net magnetization vector to rotate into the transverse plane, inducing a signal in an RF detection coil after the excitation pulse is terminated. This signal, which is a result of the free precession of the net magnetization in the transverse plane, is called the free induction decay (FID) signal, since it gradually decays due to the aforementioned relaxation mechanisms (Figure 2.2).

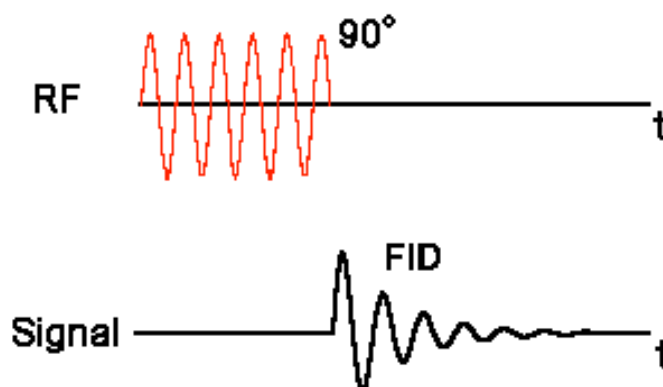


Figure 2.2 Timing diagram for a 90° RF pulse (**top**) followed by a free induction decay (FID) signal (**bottom**) of net magnetization in the transverse plane, detectable by a RF receiver coil.

When a Fourier transform is applied to this time-domain FID, the result is a NMR spectrum, which reveals the frequency components that make up the FID signal, typically reported in terms of chemical shift frequency in ppm (independent of B_0), rather than MHz. If each nucleus experiences the same local magnetic field, as is the case with perfluoro-15-crown-5-ether (PFCE: $C_{10}F_{20}O_5$), a single observed resonance peak is observed (Figure 2.3). When nuclei experience different local magnetic fields, as a result of their molecular structure, more complex spectral patterns can occur, which will be discussed in upcoming sections.

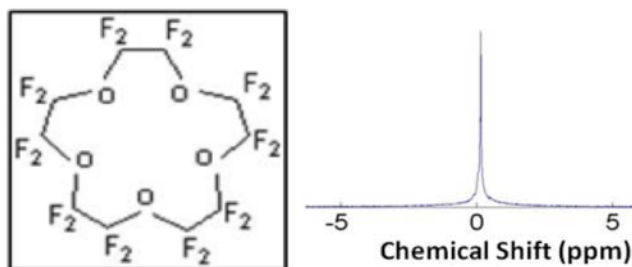


Figure 2.3 Left: Chemical structure of perfluoro-15-crown-5-ether (PFCE). ^{19}F NMR spectrum of PFCE, resulting in a single resonance peak since all ^{19}F nuclei experience the same local magnetic field.

Although there are more intricacies to nuclear magnetic resonance, this describes the basic process needed to excite and detect nuclear spins, which governs both ^1H and ^{19}F nuclei alike. MRI builds upon these NMR principles to create images of the spatial distribution of these spins, described even more briefly as follows. Gradient coils are used to change the static magnetic field strength in all three component directions (x, y, z), in any physical orientation. These gradient fields are used to encode spatial information into the spins by changing their frequency and phase, since the frequency at which the nuclei precess is dependent upon field strength (Eq. 2.1). This process generates a map of spatial frequencies, termed ‘k-space’, which when Fourier transformed, provides an image of the distribution of the spins. Several imaging schemes have been developed to generate MR signal, such as spin echo and gradient echo, as well as numerous mechanisms to generate contrast, some of which will be covered in later chapters.

2.1.2 J-coupling in ^{19}F MR of PFC NP

In NMR spectroscopy, there are two major mechanisms of spin-spin interactions. The strongest is the direct dipole-dipole interaction between nuclear spins, and the other is the indirect dipole-dipole interaction between nuclei mediated through electron spins. The first type

of interaction can affect NMR relaxation properties (e.g. T_1 and T_2) of nuclear spins, but it does not lead to a split resonance peak because fast molecular tumbling usually averages out its effect. The second type, however, generally results in a spectral peak split on the order of Hz with high-resolution NMR. The indirect dipole-dipole interaction is also called J-coupling or scalar coupling, because the coupling terms in the Hamiltonian of nuclear spins can be described as scalars (5,6).

The chemical structure and NMR spectrum of perfluorooctyl bromide (PFOB; $\text{CF}_3\text{-(CF}_2\text{)}_6\text{-CF}_2\text{Br}$) is shown in Figure 2.4, which exhibits a more complex spectral pattern than PFCE. PFOB contains three distinct groups of ^{19}F nuclei, termed ‘line groups’ since each group results in different spectral lines, which include CF_2Br , CF_3 , and $(\text{CF}_2)_6$. In a weak coupling system, in which the electron cloud between two nuclear spins is not dense, J-coupling is only related to the z component of the spins (M_z). J-coupling in most PFC molecules including PFOB are weak couplings (e.g. the coupling between the CF_3 and CF_2 groups, as well as the CF_2Br and CF_2 groups). The ^{19}F nuclear spins in CF_3 and the adjacent CF_2 group form a typical “A2B3” J-coupling system with a coupling constant of 12.3 Hz (7-9).

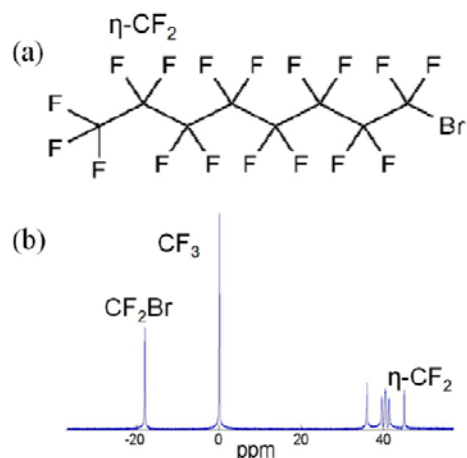


Figure 2.4 (a) Chemical structure of perfluorooctyl bromide (PFOB; $\text{CF}_3\text{-(CF}_2\text{)}_6\text{-CF}_2\text{Br}$). (b) Representative MR spectrum of PFOB. The J-coupling constant between CF_3 and the adjacent CF_2 group is 12.3 Hz.

Typical full width at half maximum (FWHM) of ^{19}F spectral peaks for *in vivo* MRI at 3T is around 100 Hz, which is an order of magnitude larger than the J-coupling frequency for PFOB for example. Therefore, instead of inducing splits in spectral peaks, J-coupling in ^{19}F MRI causes amplitude modulation of ^{19}F resonance peaks, i.e. J-modulation (6,10). J-modulation originates from the phase difference among different peaks in a J-coupling induced multiplet (a split in a spectral peak). As a result of J-modulation, the regular T_2 decay of ^{19}F nuclear spins is modulated into sinusoidal oscillations, the frequency of which is dependent on the J-coupling constant. Such an oscillating behavior dramatically shortens the apparent T_2 value (T_2') and reduces the detectable signal intensity in ^{19}F imaging (11). To achieve consistent quantitative ^{19}F MRI measurements of PFC NP emulsions, it is important to understand the effect of J-modulation on the PFOB- CF_3 group, which will be further explored in Chapter 3.

2.2 Image Acquisition with $^{19}\text{F}/^1\text{H}$ Dual-Tuned RF Coils

2.2.1 Introduction

To utilize nuclei other than hydrogen, MR systems require hardware tuned to the Larmor frequency of that nucleus. Fortunately, many 3T clinical scanners are prepared for such multi-nuclear transmit capabilities and simply require additional RF coils. Since the resonant frequencies of ^1H and ^{19}F are only about 6% different (127.8 MHz and 120.2 MHz, respectively at 3T), as seen in section 2.1, specialized RF coils can be designed to resonate at one or both frequencies.

Many early $^{19}\text{F}/^1\text{H}$ MR imaging techniques used single-frequency RF coils. A common approach was to use tunable coils, in which the coil had to be manually tuned to either the ^{19}F or ^1H frequency to maximize signal-to-noise ratio (SNR). There are several drawbacks to this

approach, which requires added time to the imaging study for manual tuning, as well as the potential for misregistration of the ^{19}F and ^1H images due to patient motion between scans (12). Alternatively, a two-coil setup with a volume coil for ^1H imaging and surface coil for ^{19}F imaging introduces inherent sensitivity profile differences at the two frequencies (13). Finally, the use of auto-tuned RF coils that can switch resonance frequencies with the assistance of an external program entails extra complexity, a higher associated cost of the imaging system, and the potential for tuning errors (14). The use of these single-frequency RF coils for $^{19}\text{F}/^1\text{H}$ MRI poses a number of limitations including challenges in simultaneously achieving high sensitivity and B_1 field homogeneity, and inaccurate co-registration of $^{19}\text{F}/^1\text{H}$ signals due to positional artifacts caused by coil retuning (15).

These limitations can be minimized with the use of dual-frequency, or dual-tuned, RF coils for multinuclear MRI/MRS (16). Dual-tuned RF coils offer several benefits, among them being user friendliness (i.e. no replacing coils between scans) without compromising sensitivity. Truly simultaneous $^{19}\text{F}/^1\text{H}$ image acquisition is possible since these coils can either transmit or receive at both frequencies at the same time. This dual-tuned feature can also add the possibility of calibrating the coil for tracer volumes of ^{19}F agent based on the ubiquitous and large field of view ^1H signal from anatomy, as seen in Chapter 4.

The commonly used shunting method and multiple poles method for designing dual-frequency coils work well when the two resonant frequencies are well separated, e.g. for ^1H (42.58 MHz/T) and ^{13}C (10.71 MHz/T). However, such methods are not well suited for designing $^{19}\text{F}/^1\text{H}$ MRI coils (17,18) because the gyromagnetic ratio of ^{19}F (40.08 MHz/T) is too close to that of ^1H (19). Several dual-frequency strategies have been proposed for MRI/MRS at close frequencies but each has limitations. A universal matching circuit for multi-nuclear NMR

has been proposed (20), but it requires multi-port inputs for multi-frequency imaging. Alternatively, several dual-frequency strategies for close and well-separated frequencies have been proposed based on the special resonant property of a birdcage resonator (21-23). In these designs, two crossed cages or two different modes of a birdcage are utilized to achieve the double resonance, so these techniques are only suitable for coils with birdcage geometry, and could lead to different B_1 field profiles at the two frequencies. Recently, a novel $^{19}\text{F}/^1\text{H}$ dual-frequency solenoid coil with identical field distribution at two frequencies at 3T has been proposed by researchers at Philips Research based on the coupled resonator model (24). However, it remains unknown whether this concept establishes a general RF design approach for such RF coils considering the various geometrical and electrical parameters required to fit the needs of diverse experimental situations (25).

This work explores the coupled resonator model as a technique to design and fabricate $^{19}\text{F}/^1\text{H}$ dual-tuned RF coils in diverse configurations. Due to the different impedances at the two resonance frequencies, matching for a dual-tuned coil remains a critical challenge in practical applications. Accordingly, the electrical properties of the coupled resonator model were considered and numerical calculations were executed to prove that a series capacitive matching network is effective in matching the coupled resonator to 50 Ohm at both ^{19}F and ^1H frequencies (18,26). A $^{19}\text{F}/^1\text{H}$ dual-tuned single-turn solenoid RF coil for *in vivo* imaging at 3T was designed and constructed to illustrate the feasibility of the model, and tested for imaging performance.

2.2.2 Methods

The following coupled resonator model for $^{19}\text{F}/^1\text{H}$ dual-tuned coils was largely established by Hockett et al. (27) and expanded upon by Hu et al. (28).

2.2.2.1 Coupled Resonator Model

In the coupled resonator model, the RF sample coil is connected to a secondary inductor and capacitor (LC) resonator with a coupling capacitor in series (Figure 2.5a). For nuclei with close resonance frequencies, such as ^1H and ^{19}F , the inductance of a MR sample coil can be treated as a constant value. Following the theoretical analysis proposed by Haase et al (29), when the secondary resonator is built with identical frequency to the sample coil, two possible oscillating modes are formed within the circuit, namely in-phase and anti-phase modes. When resonating in the in-phase mode, the two resonators of the circuit have equal electrical potentials, and thus the voltage and current across the coupling capacitor always remains zero. In this case, the coupling capacitor can be virtually removed and then the equivalent circuit of the coupled resonator can be drawn as Figure 2.5b with the resonance frequency

$$\omega_m = \gamma_H B = 1 / \sqrt{LC_{t1}}. \quad [2.6]$$

In contrast, for the anti-phase mode, the electrical potential at both sides of the coupling capacitor is opposite, so the voltage at the middle point of coupling capacitor remains zero. For circuit analysis, a virtual short wire can be added between the ground and the middle point of the coupling capacitor (Figure 2.5c), and thus it gives rise to a different resonant frequency

$$\omega_o = \gamma_F B = 1 / \sqrt{L(C_{t1} + 2C_c)}. \quad [2.7]$$

Given the gyromagnetic ratios of ^1H and ^{19}F , when

$$C_c / C_{t1} = 0.064, \quad [2.8]$$

the two frequencies of the coupled resonator correspond to ^1H and ^{19}F frequencies, in agreement with the analytic calculation of transfer impedance (27).

2.2.2.2 Impedance Matching

Impedance matching is critical in dual-tuned coil design because the circuit impedance could be different at the two resonant frequencies. For the coupled identical resonator model (Figure 2.6d), by inverting the admittance of the parallel components, the impedance of the coupled resonator is

$$Z_{hi} = \frac{X_L + r_1}{1 + (X_L + r)X_{C_{t1}}} \quad [2.9]$$

at high frequency or in-phase mode; and

$$Z_{lo} = \frac{X_L + r_1}{1 + (X_L + r)(2X_{C_c} + X_{C_{t1}})} \quad [2.10]$$

at low frequency or anti-phase mode.

In the dual-tuned coil design (Figure 2.5d), the coupled resonator is connected to the MR scanner at the end of the secondary resonator in series with a capacitor matching circuit. In this case, a small detuning of two resonators, which renders them slightly off-resonance, is able to introduce an extra degree of freedom and compensate for the impedance difference (29). To show the coupled resonator can always be matched to 50 Ohm with the use of appropriate values for tuning, coupling and matching capacitors, we numerically calculated several realistic circuit examples corresponding to various combinations of internal resistances of the sample coil and secondary resonator. We assumed that the sample coil with an inductance 47 nH, which is equal to the inductance of the secondary resonator, is designed to work at 3T for dual-frequency ^{19}F and ^1H imaging. A custom-developed program in MATLAB (MathWorks, Natick, MA, USA) was used to seek for the appropriate values of C_{t1} , C_{t2} , C_c , and C_m to match the circuit at both frequencies (120.2 MHz and 127.8 MHz). In the program, the preset values of C_{t1} , C_{t2} , C_c were first calculated according to Eqs. 2.6-2.8. Then, C_m was set to be a qualitatively correct value

according to Eqs. 2.9-2.10. Finally, a nonlinear root-seeking algorithm was carried out to vary all the capacitances around their preset values to successively achieve impedance matching.

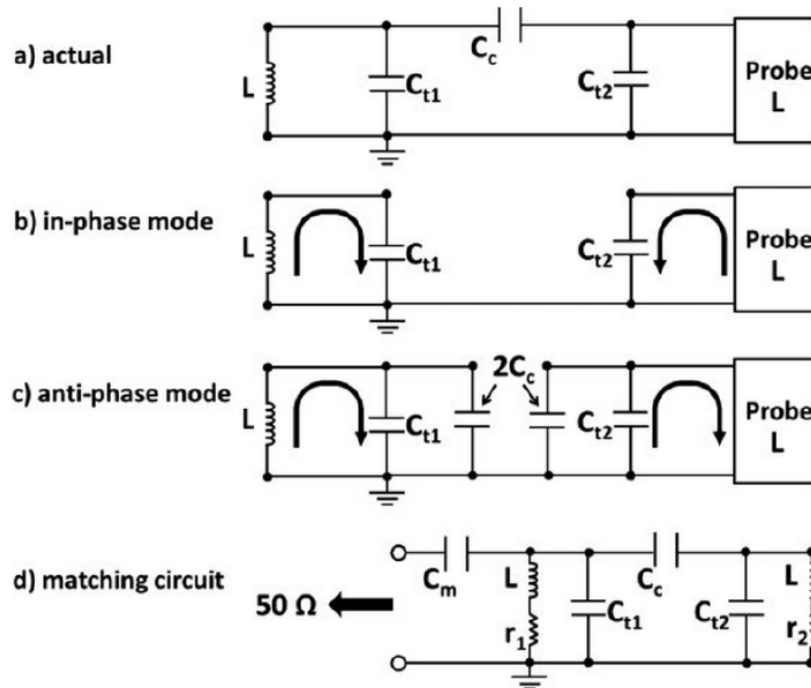


Figure 2.5 Schematic diagram of a coupled resonator circuit. (a) the resonator formed by capacitor C_{t2} and probe (with inductance L) is capacitively coupled, by capacitor C_c , to the secondary resonator formed by capacitor C_{t1} and inductor L . (b & c) the equivalent circuit of in-phase and anti-phase mode. (d) coupled resonator is capacitively matched to 50 Ohm with C_m . [Figure reprinted with permission from Hu et al. (30)]

2.2.2.3 Construction of Volume Coils for $^{19}\text{F}/^1\text{H}$ MRI at 3T

To the concept at 3T, two $^{19}\text{F}/^1\text{H}$ volume coils were designed and constructed, with the intention to be use for rat imaging. The first design was a transmit/receive single-turn solenoid coil (8 cm diameter, 11 cm length) and the second was a similar, but larger design (11.5 cm diameter, 14 cm length). Both coils were designed to work on a Philips 3T clinical whole-body scanner, with ^{19}F and ^1H resonant frequencies of 120.2 MHz and 127.8 MHz, respectively.

The smaller single-turn solenoid coil was constructed with adhesive copper tape on an acrylic tube 8 cm in diameter and 11 cm in length. The 1st resonant mode of the coil was tuned to

the ^1H frequency, 127.8 MHz (31). The secondary resonator was built with a tunable capacitor in parallel with a custom-made inductor, which has a diameter of 4 mm and the same inductance as the sample coil. The secondary resonator was positioned > 2 cm away from the sample coil to minimize inductive coupling between two circuits. The coupling between the sample coil and secondary resonators was implemented with another tunable capacitor in series with a fixed value capacitor on the other port for the purpose of balancing. The secondary loop also was tuned to resonance at 127.8 MHz. The value of the coupling capacitor was then adjusted to over-couple these two resonators giving rise to the second distinct frequency at 120.2 MHz (31). The feed point for this coil (connected to a custom T/R box that interfaces with the clinical Philips scanner) was located at the secondary resonator input and the whole circuit was matched to 50 Ohm with a tunable capacitor and fixed value capacitor. Figure 2.6 shows the circuit design as well as an electrical simulation of the resonance properties of the coil in SPICE software.

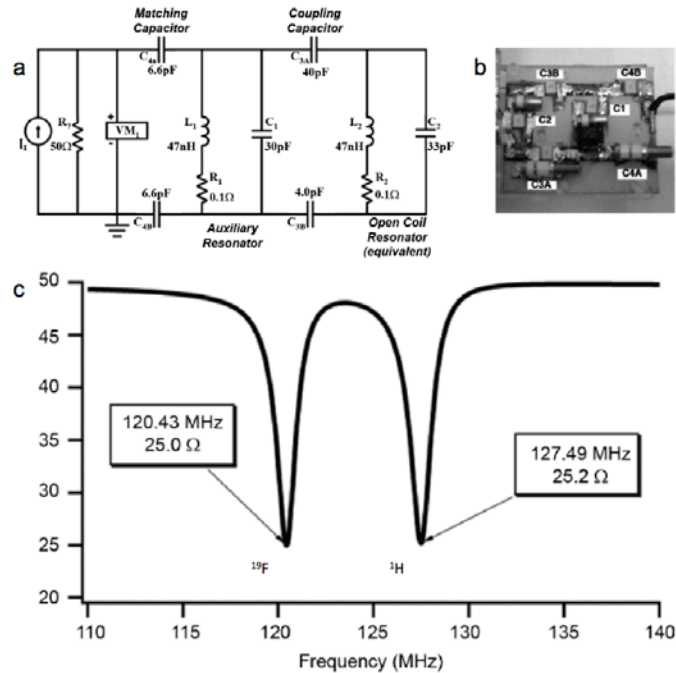


Figure 2.6 $^{19}\text{F}/^1\text{H}$ dual-tuned RF coil circuit. (a) Equivalent circuit diagram of two separate LCR resonators (L_1 , C_1 , R_1) and (L_2 , C_2 , R_2) electrically coupled via capacitor C_3 . (b) Image of second resonator circuit with coupling capacitors ($C3A$ and $C3B$) and matching capacitors ($C4A$ and

C4B) labeled. (c) Theoretical impedance magnitude output of a SPICE simulation of two capacitively coupled resonators. [Figure reprinted with permission from Hockett et al. (27)]

2.2.2.4 Bench Test of Electromagnetic Performance

Laboratory bench tests were performed on a network analyzer (Hewlett Packard 8751A). For the tuning and matching procedure, there are a total of four variable capacitors to be adjusted for each coil. Tuning capacitors for the sample coil and secondary resonator were first adjusted to tune the two resonators to the ^1H frequency, 127.8 MHz. Then the coupling and matching capacitors were adjusted to achieve the second ^{19}F frequency at 120.2 MHz, followed by matching the dual-tuned coil impedance to 50 Ohm. The coil return loss (S11) of two coils was tested by using a 300 ml tube filled with 1% saline to mimic the electrical load of a live rat. S21 measurements of the B_1 field produced by the sample coil were performed with a 10 mm shielded loop for signal pick up. These measurements were used to spread the capacitance of the coupled capacitor (C_1 , or C_{11} in Eq. 2.6) over the length of the solenoid.

2.2.2.5 Phantom and *In Vivo* Imaging

Imaging performance of the smaller (8 cm diameter) coil was tested with a 300 ml bottle of 1% saline. T_1 -weighted gradient echo (FFE) imaging was performed with the following parameters were: FOV 128 mm, 256×256 matrix, slice thickness = 2 mm, voxel size = 0.5×0.5×2 mm, $\alpha = 35^\circ$, TR/TE = 20.16/6.02 ms, 25 NSA, and a scanning time of 2.1 minutes. A signal intensity profile was calculated along the coronal direction of acquired images. RF field homogeneity was analyzed by acquiring B_1 maps with an actual flip angle imaging (AFI) sequence with the following parameters: 128 mm FOV, 256×256 matrix, 15 2-mm slices, 0.5×0.5×2 mm resolution, $\alpha = 70^\circ$, 2.8 min scan time.

The potential for ^{19}F MR molecular imaging was tested in a rat model of asthma. In accordance with institution approved protocols, an airway inflammation model was developed in brown Norway rats induced with injection of house dust mite (HDM) into the airway (32). After 14 days, the lungs were imaged 2h post-injection (i.v.) of 1.0 ml/kg $\alpha_v\beta_3$ -integrin targeted PFOB NP as previously described (33). To avoid signal contamination from inhaled fluorinated anesthesia, a xylazine (10mg/kg) / ketamine (85 mg/kg) i.m. injection was used for anesthesia induction, which was maintained with a ketamine i.v. infusion (18 mg/kg/hr). A radial 3D balanced UTE-SSFP sequence (as described in Chapter 3) was used with the 8 cm diameter $^{19}\text{F}/^1\text{H}$ dual-tuned transmit/receive solenoid coil with the following parameters: FOV = 140 mm, matrix 64^3 , isotropic voxel $\Delta x = 2.19$ mm, $\alpha = 30^\circ$, excitation bandwidth exBW = 5 kHz centered on the PFOB- CF_2 line group, pixel bandwidth pBW = 900 Hz, TR = 1.75 ms, TE = 90 μs (FID sampling), and a scanning time of 30 minutes.

2.2.3 Results

Photographs of dual-tuned $^{19}\text{F}/^1\text{H}$ solenoid coils are shown in Figure 2.7, along with the transmit/receive box that interfaces with the clinical scanner via a BNC connector.

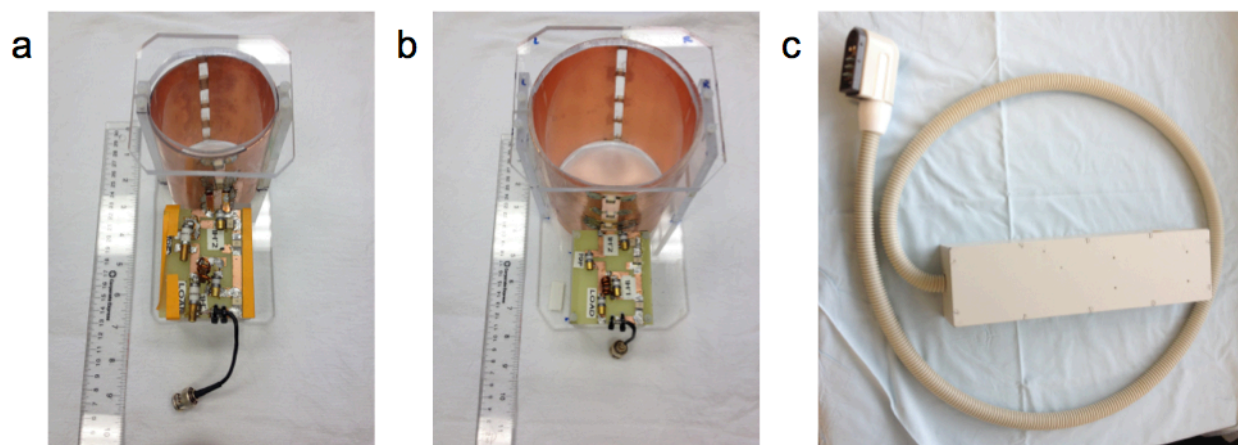


Figure 2.7 Photographs of single-turn solenoid RF coils. (a) Smaller coil (8 cm diameter). (b) Larger coil (11.5 cm diameter). (c) T/R box that interfaces with clinical scanner.

2.2.3.1 Bench Tests

The coil return loss (S11) of two coils was tested by using a 300 ml tube filled with 1% saline to mimic the electrical load of a live rat. Although the original images could not be saved due to older network analyzer software, Figure 2.8 shows representative log magnitude and Smith charts of the signal loss measurements of a different phantom (50 mL saline tube) captured with a newer network analyzer.

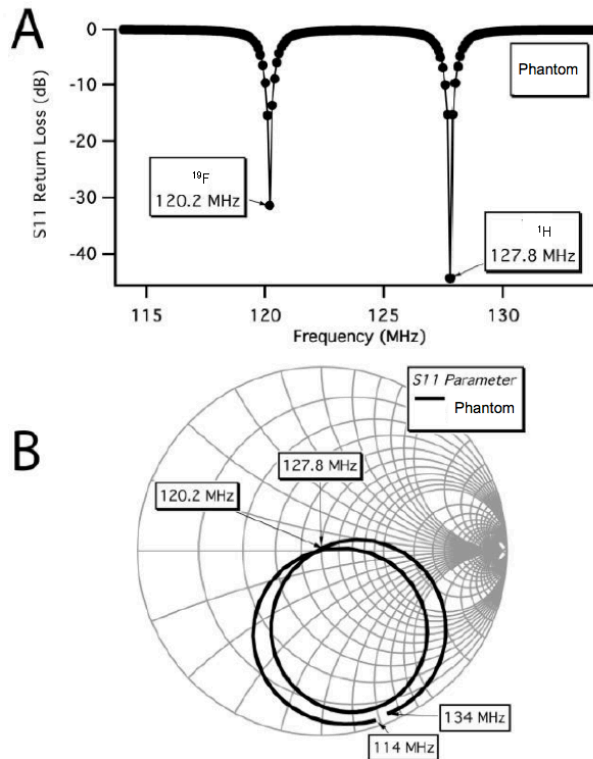


Figure 2.8 Simultaneous dual-frequency return loss (S11) of single-turn solenoid coil measured using network analyzer. Return loss, better than -30 dB, is observed at both the ^1H (127.8 MHz) and ^{19}F (120.2 MHz) resonance frequencies.

S21 measurements of the B_1 field produced by the smaller solenoid coil were used to spread the capacitance of the coupled capacitor over the length of the solenoid, as seen in Figure 2.9. This arrangement, proposed by an experience RF engineer, resulted in S21 measurements at 15 locations throughout the coil (measured as dB signal loss) that varied by no more than 2.1% at

the ^{19}F frequency and no more than 2.6% on the ^1H frequency (as opposed to 17% and 20% at both frequencies without spreading the capacitance out).

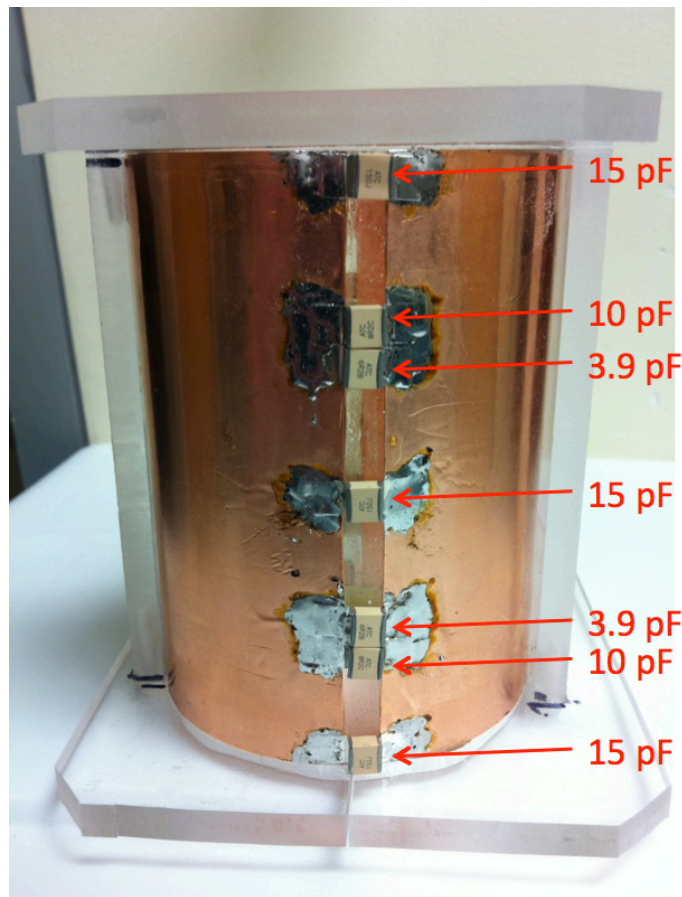


Figure 2.9 Arrangement of capacitors used to spread out the current in the 8 cm diameter $^{19}\text{F}/^1\text{H}$ dual-tuned single-turn solenoid coil.

2.2.3.2 Phantom and *In Vivo* $^{19}\text{F}/^1\text{H}$ Imaging

Figure 2.10 shows the ^1H imaging characteristics of the 8 cm diameter solenoid coil, with a cross-sectional T_1 -weighted FFE image and a profile drawn through the center of the image. Taking into account the inherent noise in this high-resolution image, it is apparent that the coil produces a very homogeneous RF field. This is supported by the AFI B_1 map (Figure 2.11), in which the ratio of the actual/requested flip angle produced by the coil is $119.76\% \pm 0.03\%$ (standard error of the mean).

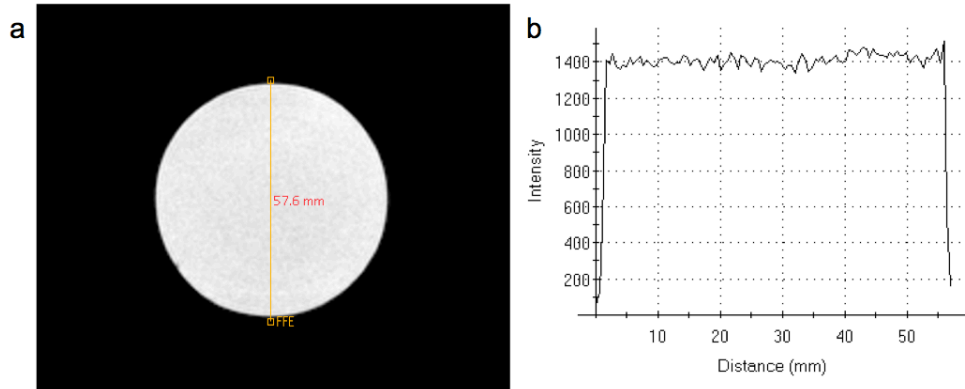


Figure 2.10 (a) T_1 -weighted ^1H FFE image of saline phantom using 8 cm diameter $^{19}\text{F}/^1\text{H}$ dual-tuned solenoid coil. (b) Signal intensity profile over the distance of the phantom, as indicated.

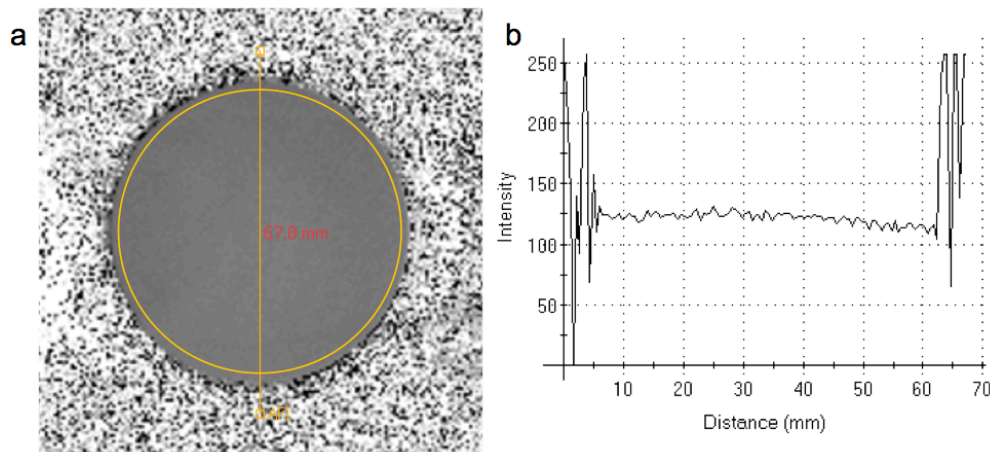


Figure 2.11 (a) AFI B_1 map of saline phantom using 8 cm diameter $^{19}\text{F}/^1\text{H}$ dual-tuned solenoid coil ($119.76\% \pm 0.03\%$ actual/requested flip angle). (b) AFI intensity profile over the distance of the phantom, as indicated.

Figure 2.12 displays the *in vivo* imaging capability of the 8 cm $^{19}\text{F}/^1\text{H}$ dual-tuned solenoid coil. When tuned to better than -30dB signal loss on both frequencies, the coil enables high-quality ^1H and ^{19}F images (Fig. 2.13a&b, respective) of $\alpha_v\beta_3$ -integrin targeted PFC NP in a rat lung model of asthma using a truly simultaneous $^{19}\text{F}/^1\text{H}$ balanced UTE-SSFP sequence.

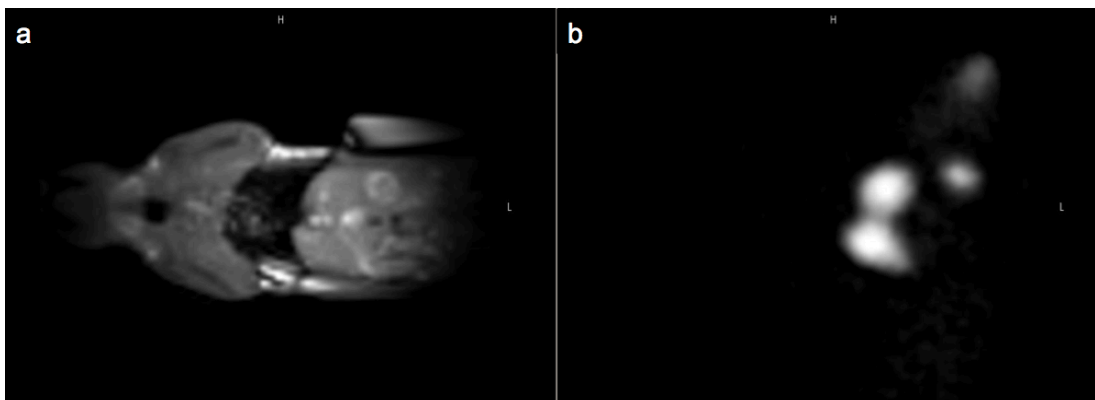


Figure 2.12 ^1H (a) and ^{19}F (b) images of a rat lung model of asthma using simultaneous $^{19}\text{F}/^1\text{H}$ imaging of $\alpha_v\beta_3$ -integrin targeted PFC NP.

2.2.4 Discussion

This work described a generalized strategy for designing and fabricating $^{19}\text{F}/^1\text{H}$ dual-tuned coils based on the coupled resonator approach. The single-turn solenoid coil tested here with phantom and *in vivo* imaging experiments on a clinical 3T scanner was shown to produce high-quality ^1H and ^{19}F images, with sensitive detection of PFC NP. A unique feature of this design is that it preserves the B_1 field homogeneity of the RF coil at both resonance frequencies. By eliminating the effects of patient motion between ^1H and ^{19}F image acquisition, this coil design enables direct co-registration of ^{19}F and ^1H images for localizing delivered ^{19}F PFC NP agents.

The coupled resonator paradigm for designing dual-tuned coils may be limited when imaging nuclei with well-separated frequencies. In this case, the frequency-dependent inductance of the sample coil will be significantly different at the two working frequencies. It will be difficult to construct a small copper loop inductor that has the same frequency-dependent inductance as the sample coil, and thus it will hinder the equivalence of the sample coil and the secondary resonator. The “in-phase” and “anti-phase” modes, as described previously, will not form as expected. Therefore, the strategy of using the coupled resonator model to fabricate a

dual-frequency MRI coil is only suitable for close Larmor frequencies, e.g. $^{19}\text{F}/^1\text{H}$ or possibly $^{13}\text{C}/^{23}\text{Na}$.

2.2.5 Conclusion

As the installed-base clinical scanners with multinuclear capabilities continues to grow, this coupled resonator dual-tuned coil design may help facilitate ultimate clinical adoption of simultaneous $^{19}\text{F}/^1\text{H}$ MR molecular imaging techniques.

2.3 Acknowledgements

I would like to thank Frank Hockett and Lance Hu, from whom I learned $^{19}\text{F}/^1\text{H}$ dual-tuned RF coil theory, and with whom I designed and constructed the single-turn solenoid coils. The construction and testing of the 8 cm diameter solenoid coil was performed by me.

2.4 References

1. Systems PM. Basic Principles of MR Imaging. Eindhoven, North Brabant, The Netherlands 1993. p 139.
2. Farrar TC, Becker ED. Pulse and Fourier transform NMR; introduction to theory and methods. New York,; Academic Press; 1971. xiv, 115 p. p.
3. Ackerman JJH. Course Lecture. CHEM 576 "Magnetic Resonance". 2010.
4. Caruthers SD. Course Lecture. BME 502 "Cardiovascular MRI - From Physics to Clinical Application". 2008.
5. Levitt M. Spin Dynamics: Basics of Nuclear Magnetic Resonance. Hoboken, NJ: John Wiley & Sons; 2008. 740 p.

6. Mason RP, Bansal N, Babcock EE, Nunnally RL, Antich PP. A novel editing technique for ¹⁹F MRI: molecule-specific imaging. *Magn Reson Imaging* 1990;8(6):729-736.
7. Sotak CH, Hees PS, Huang HN, Hung MH, Krespan CG, Reynolds S. A new perfluorocarbon for use in fluorine-19 magnetic resonance imaging and spectroscopy. *Magn Reson Med* 1993;29(2):188-195.
8. Stables LA, Kennan RP, Anderson AW, Gore JC. Density matrix simulations of the effects of J coupling in spin echo and fast spin echo imaging. *J Magn Reson* 1999;140(2):305-314.
9. Allerhand A, Gutowsky HS, Jonas J, Meinzer RA. Nuclear magnetic resonance methods for determining chemical-exchange rates. *J Am Chem Soc* 1966;88(14):3185-3193.
10. Babcock EE, Mason RP, Antich PP. Effect of homonuclear J modulation on ¹⁹F spin-echo images. *Magn Reson Med* 1991;17(1):179-188.
11. Giraudeau C, Flament J, Marty B, Boumezbeur F, Meriaux S, Robic C, Port M, Tsapis N, Fattal E, Giacomini E, Lethimonnier F, Le Bihan D, Valette J. A new paradigm for high-sensitivity ¹⁹F magnetic resonance imaging of perfluorooctylbromide. *Magn Reson Med* 2010;63(4):1119-1124.
12. Cron GO, Beghein N, Ansiaux R, Martinive P, Feron O, Gallez B. ¹⁹F NMR in vivo spectroscopy reflects the effectiveness of perfusion-enhancing vascular modifiers for improving gemcitabine chemotherapy. *Magn Reson Med* 2008;59(1):19-27.
13. Ikehira H, Girard F, Obata T, Ito H, Yoshitomi H, Miyazaki M, Nakajima N, Kamei H, Kanazawa Y, Takano H, Ito H, Tanada S, Sasaki Y. A preliminary study for clinical pharmacokinetics of oral fluorine anticancer medicines using the commercial MRI system ¹⁹F-MRS. *The British journal of radiology* 1999;72(858):584-589.

14. de Alejo RP, Garrido C, Villa P, Rodriguez I, Vaquero JJ, Ruiz-Cabello J, Cortijo M. Automatic tuning and matching of a small multifrequency saddle coil at 4.7 T. *Magn Reson Med* 2004;51(4):869-873.
15. Tomanek B, Volotovskyy V, Gruwel MLH, McKenzie E, King SB. Double-frequency birdcage volume coils for 4.7T and 7T. *Concepts Magn Reson B* 2005;26B(1):16-22.
16. Brix G, Schlicker A, Mier W, Peschke P, Bellemann ME. Biodistribution and pharmacokinetics of the (19)F-labeled radiosensitizer 3-aminobenzamide: assessment by (19)F MR imaging. *Magn Reson Imaging* 2005;23(9):967-976.
17. Hu S, Reimer J, Bell A. Single-input double-tuned circuit for double resonance nuclear magnetic resonance experiments. *Rev Sci Instrum* 1998;69(2).
18. Mispelter J, M L, A B. NMR probeheads for biophysical and biomedical experiments: theoretical principles & practical guidelines. Hackensack, NJ: Imperial College Press; 2006.
19. Lanza GM, Winter PM, Caruthers SD, Hughes MS, Hu G, Schmieder AH, Wickline SA. Theragnostics for tumor and plaque angiogenesis with perfluorocarbon nanoemulsions. *Angiogenesis* 2010;13(2):189-202.
20. Li Y, Logan TM, Edison AS, Webb A. Design of small volume HX and triple-resonance probes for improved limits of detection in protein NMR experiments. *J Magn Reson* 2003;164(1):128-135.
21. Lanz T, Ruff J, Weisser A, Haase A. Double tuned ²³Na ¹H nuclear magnetic resonance birdcage for application on mice in vivo. *Review of Scientific Instruments* 2001;72(5):2508-2510.

22. Fitzsimmons JR, Beck BL, Brooker HR. Double resonant quadrature birdcage. *Magn Reson Med* 1993;30(1):107-114.
23. Shen GX, Boada FE, Thulborn KR. Dual-frequency, dual-quadrature, birdcage RF coil design with identical b1 pattern for sodium and proton imaging of the human brain at 1.5 T. *Magn Reson Med* 1997;38(5):717-725.
24. Mazurkewitz P, Leussler C; Double resonant transmit receive solenoid coil for MRI. USA2009 Mar 15, 2007.
25. Doty FD, Entzminger G, Kulkarni J, Pamarthy K, Staab JP. Radio frequency coil technology for small-animal MRI. *NMR Biomed* 2007;20(3):304-325.
26. Alecci M, Romanzetti S, Kaffanke J, Celik A, Wegener HP, Shah NJ. Practical design of a 4 Tesla double-tuned RF surface coil for interleaved ¹H and ²³Na MRI of rat brain. *J Magn Reson* 2006;181(2):203-211.
27. Hockett FD, Wallace KD, Schmieder AH, Caruthers SD, Pham CTN, Wickline SA, Lanza GM. Simultaneous dual frequency ¹H and ¹⁹F open coil imaging of arthritic rabbit knee at 3T. *IEEE T Med Imaging* 2011;30(1):22-27.
28. Hu L, Hockett FD, Chen J, Zhang L, Caruthers SD, Lanza GM, Wickline SA. A generalized strategy for designing ¹⁹F/¹H dual-frequency MRI coil for small animal imaging at 4.7 Tesla. *J Magn Reson Imaging* 2011;34(1):245-252.
29. Haase J, Curro NJ, Slichter CP. Double resonance probes for close frequencies. *J Magn Reson* 1998;135(2):273-279.
30. Hu LZ, Hockett FD, Chen JJ, Zhang L, Caruthers SD, Lanza GM, Wickline SA. A Generalized Strategy for Designing F-19/H-1 Dual-Frequency MRI Coil for Small Animal Imaging at 4.7 Tesla. *J Magn Reson Imaging* 2011;34(1):245-252.

31. JM J. Electromagnetic analysis and design in magnetic resonance imaging. Boca Raton, FL: CRC Press; 1998.
32. Farhadi N, Ulrich K, Lamb D, Allen S, Douglas G, Whybrow L, Mori H, Janies J, Parker N, Adcock J, Dubray C, Hincks J, Taylor B, Evans S. Development of House Dust Mite Allergen-Induced Airway Inflammation Model in Brown Norway Rats; Modulation by Roflumilast and Fluticasone. C30 INFLAMMATORY AND IMMUNOLOGICAL MODELS OF ASTHMA, American Thoracic Society International Conference Abstracts: American Thoracic Society. p A4221.
33. Neubauer AM, Caruthers SD, Hockett FD, Cyrus T, Robertson JD, Allen JS, Williams TD, Fuhrhop RW, Lanza GM, Wickline SA. Fluorine cardiovascular magnetic resonance angiography in vivo at 1.5 T with perfluorocarbon nanoparticle contrast agents. *J Cardiovasc Magn Reson* 2007;9(3):565-573.

Chapter 3. Balanced UTE-SSFP for ^{19}F MR Imaging of Complex

Spectra

3.1 Introduction

Magnetic resonance methods are emerging for functional and quantitative physiological detection of nuclei other than hydrogen (1), all of which require specific optimization of imaging techniques and hardware. Sodium imaging has been successfully utilized in knee imaging (2,3), while hyperpolarized and non-hyperpolarized gases are also proving useful in lung imaging (4,5). Concomitant development of novel contrast agents has created possibilities for imaging a variety of nuclei, for example recently the multiple molecular species of liquid perfluorocarbons in nanoparticle formulations (6). Targeted perfluorocarbon (PFC) imaging agents profess the opportunity to target and quantify markers of disease in cardiovascular, oncological, and other applications. Some of the early work involved targeted cells, both *in vitro* and *in vivo*, and tracking the cells by detecting their unique fluorine signatures (7,8). Other techniques involve the accumulation of tracers by macrophages, which can then be imaged by their fluorine signals (9). Still other agents have been shown to target pathological tissues to detect and quantify biomarker concentration, as exemplified by $\alpha_v\beta_3$ -integrin targeting of angiogenesis in cancer and atherosclerosis (10-13). Moreover, commercial interest in such agents by pharmaceutical companies has been demonstrated by recent reports of angiogenesis targeting and imaging with ^{19}F compounds (14).

^{19}F magnetic resonance spectroscopy and imaging offer several advantages over hydrogen-based methods, including highly specific detection due to an absence of biological background signal, and the ability to quantify local concentration of fluorinated agents (15). As such, ^{19}F MRI bears a high potential for molecular imaging allowing the direct quantification of

targeted PFC nanoparticle (NP) emulsions (16). Previous *in vivo* reports of PFC NP have exploited the single resonance peak of perfluoro-15-crown-5-ether (PFCE; C₁₀F₂₀O₅) (17). However, perfluorooctyl bromide (PFOB; CF₃-(CF₂)₆-CF₂Br) is a more clinically-relevant NP core with a better understood human safety profile (18), but it exhibits a more complex spectrum with seven ¹⁹F resonance peaks and multiple relaxation conditions (19). Furthermore, although gadolinium (Gd) chelates have been shown to enhance the ¹⁹F signal through T₁ shortening (20,21), the absence of Gd is more attractive from a translational point of view, due to the risk of nephrogenic systemic fibrosis (NSF) associated with Gd agents (22-24).

While true for any non-proton contrast agent, fluorine-based agent detection incurs several inherent technical challenges. Many agents have short apparent T₂' relaxation times, which can vary across their spectral peaks (25). In addition, rich spectra and large chemical shifts (CS) like those found in PFOB add significant complexity that challenges optimal signal detection. Several methods have been developed to manage CS artifacts and cope with short apparent T₂' times encountered in multinuclear MR. Mastropietro et al. have recently optimized the sequence parameters of fast spin-echo (FSE/RARE) for some ¹⁹F reporters, but different fluorinated agents will likely require individual parameter tuning based on their spectral properties and the local environment (26). Single ¹⁹F resonances, such as the CF₃ line group in PFOB, have been utilized (27), but significant tradeoffs in SNR efficiency remain when other lines are ignored. Others have investigated chemical species separation using an iterative decomposition with echo asymmetry and least-squares estimation (IDEAL), which requires a complex δB_0 correction (28,29). In an effort to capture signal from all PFOB spins, echo-time encoding with relaxation correction has been implemented (30), in addition to pulse-phase encoding (PPE) (31). Lastly, chemical shift independent techniques like fluorine ultrafast turbo

spectroscopic imaging (F-uTSI) have been employed to register the entire ^{19}F spectrum (32,33), albeit with a significant acquisition time penalty.

Perhaps the most straightforward method to image complex ^{19}F spin systems in consideration of destructive phase interference is to acquire the signal before the spins dephase, as in ultra-short echo time (UTE) imaging (34). Line dephasing occurs over time, when the spin species of an imaging agent are subject to individual Larmor precession according to their respective chemical shift, which can lead to destructive signal overlay. In addition, transverse relaxation prevents a full signal recovery at later time points. Short echo time sequences like UTE offer the ability to capture these spins before line dephasing occurs, and thus retain their NMR signal to potentially boost the SNR (35). Balanced steady-state free precession (SSFP) is a technique in which each gradient pulse within one TR is compensated by a gradient pulse with an opposite polarity, resulting in a single, rephased magnetization vector (36). As such, the SSFP sequence retains much of the initial magnetization (M_0), which yields a steady state MR signal with high achievable SNR. Furthermore, the elimination of gradient-induced dephasing within each TR would further counteract the line dephasing that occurs in complex spectra.

Accordingly, a new technique—dual-frequency $^{19}\text{F}/^1\text{H}$ UTE with a balanced SSFP pulse sequence and 3D radial readout—was developed to permit highly sensitive detection of multi-resonant imaging labels like PFOB without the need for Gd. It was hypothesized that the $^{19}\text{F}/^1\text{H}$ UTE-SSFP pulse sequence with 3D radial acquisition would image PFOB NP with higher detection sensitivity than tradition Cartesian k-space filled ^{19}F sequences including gradient echo (GRE), balanced SSFP, and fast spin echo (FSE) on the PFOB $(\text{CF}_2)_6$ group, as well as the PFOB CF_3 peak sampled with FSE. The preclinical objective of this study was to image angiogenesis in a rabbit adenocarcinoma model with the simultaneous $^{19}\text{F}/^1\text{H}$ UTE-SSFP technique using $\alpha_v\beta_3$ -

targeted PFOB nanoparticles with and without Gd to establish the feasibility of high sensitivity MR molecular imaging of Gd-free, fluorine-based, clinically relevant contrast agents. Such a technique will be critical for the clinical implementation of targeted molecular MRI.

3.2 Methods

3.2.1 Pulse Sequence Design

To optimize pulse sequence parameters, the spectral characteristics and NMR relaxation properties of the PFOB molecule were analyzed (Figure 3.1). In addition to single ^{19}F resonance peaks for the PFOB CF_2Br and CF_3 groups, the CF_2 line group contains twelve of the seventeen fluorine nuclei, which result in five spectral components (at 3T: 0, ± 100 Hz, ± 500 Hz). As shown in Figure 3.1b, the five proximate chemical shift (CS) components of the CF_2 group, represented by different spin vectors (β , γ , δ , ϵ , ζ , ρ), lead to destructive signal overlay at larger echo times (e.g., 2.8 ms). However, all CS components remain within a phase range of $\pm 90^\circ$ for 0.5 ms and are not yet significantly affected by the apparent T_2' relaxation (10 ms) (37). Using a UTE-SSFP sequence with an echo time of 100 μs , a typical gradient performance of $200 \text{ Tm}^{-1}\text{s}^{-1}$ and a pixel bandwidth of 1 kHz, the FID readout requires ~ 0.6 ms resulting in a spatial resolution of ~ 1 mm, which is well suited for the detection and quantification of targeted PFOB-NP. During a fast FID readout, as in the balanced UTE-SSFP technique presented here, the relative signal from the CF_2 resonances remains above 60%, which cannot be recovered at later echo times.

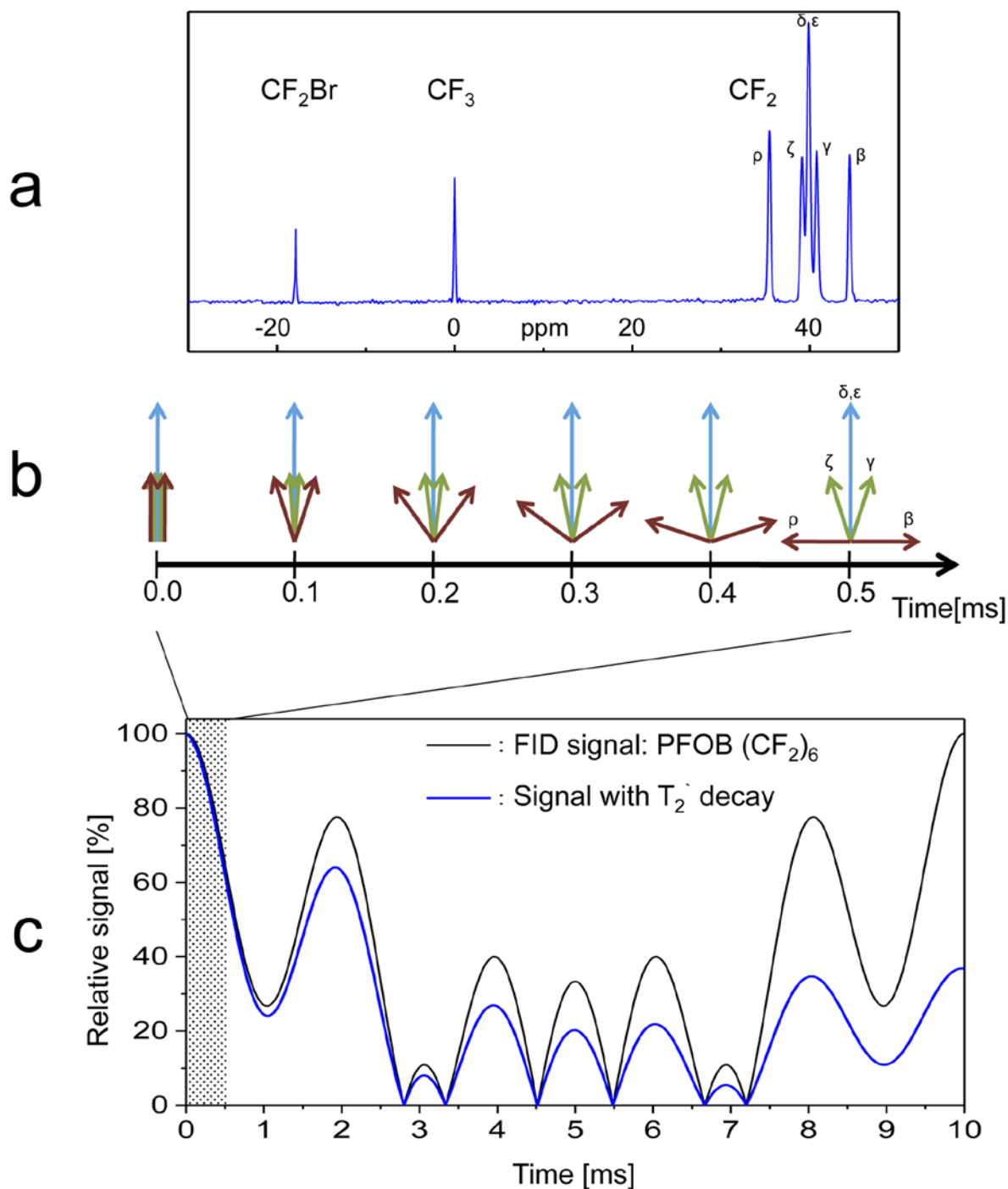


Figure 3.1 a: Perfluorooctyl bromide (PFOB: CF₃-(CF₂)₆-CF₂Br) ¹⁹F spectrum. **b:** All chemical shift components of PFOB CF₂ line group (β, γ, δ, ε, ζ, ρ) remain within a phase range of ± 90° for 0.5 ms. **c:** ¹⁹F signal evolution of the (CF₂)₆ line group with and without apparent T₂' relaxation. During a fast FID readout as in the balanced UTE-SSFP technique, the relative signal remains above 60%, which cannot be recovered for later echo times. [Figure reprinted from Goette, et al. *In press*]

A simultaneous 3D $^{19}\text{F}/^1\text{H}$ balanced UTE-SSFP pulse sequence was designed to capture these CF_2 resonances (Fig. 3.2). The sequence consists of simultaneous $^{19}\text{F}/^1\text{H}$ RF excitation (38) and subsequent FID acquisition at an ultra-short echo time, using balanced gradients with a Wong-type (39) radial readout trajectory. The UTE excitation and FID acquisition are designed to acquire the ^{19}F signal before dephasing develops, while the balanced SSFP gradients are designed to exploit the achievable high steady-state signal and to synergistically reduce extraneous line dephasing. The simultaneous ^1H excitation and acquisition is not necessarily part of the sensitive ^{19}F detection sequence but is beneficial for an efficient scan time and precise co-localization of fluorine signals with the underlying anatomy.

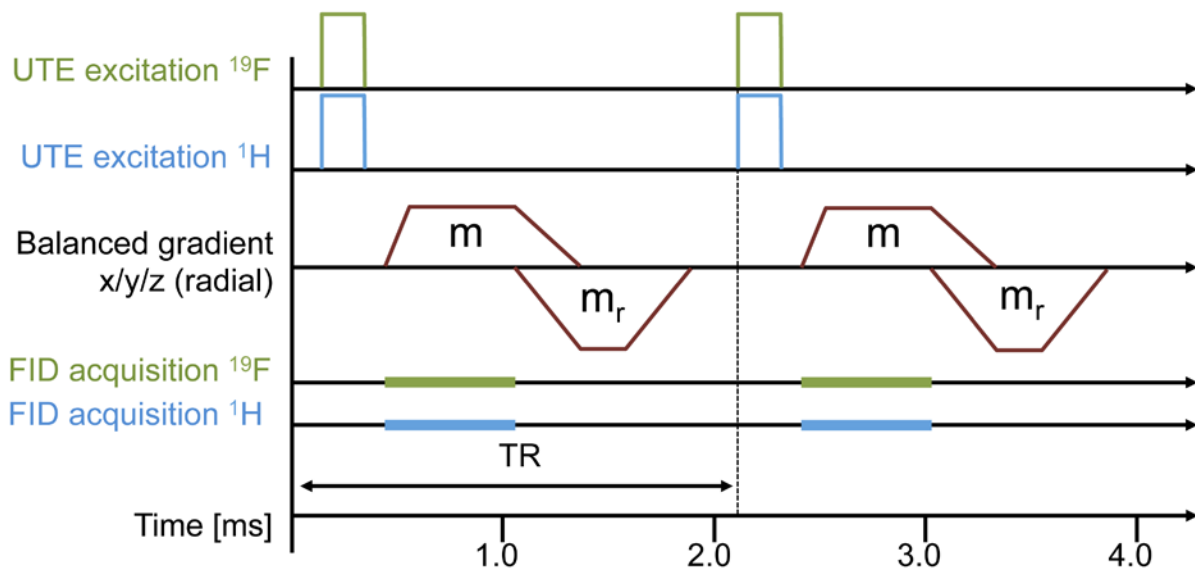


Figure 3.2 A simultaneous 3D $^{19}\text{F}/^1\text{H}$ balanced UTE-SSFP pulse sequence, consisting of simultaneous $^{19}\text{F}/^1\text{H}$ RF excitation and subsequent FID acquisition at an ultra-short echo time, using balanced gradients (m , m_r) with a Wong-type (39) radial readout trajectory. Logical gradient lobes (m , m_r) are superimposed into a single continuous gradient waveform when executed on the physical gradient coils. [Figure reprinted from Goette et al. *In press*]

3.2.2 Phantom Imaging Experiments

The study was performed on a 3T clinical whole-body scanner (Achieva, Philips Healthcare, The Netherlands), outfitted with a dual $^{19}\text{F}/^1\text{H}$ spectrometer system (38). Dual-resonant $^{19}\text{F}/^1\text{H}$ RF coils were used, which can either transmit or receive at both frequencies simultaneously (40).

Feasibility of balanced UTE-SSFP imaging was demonstrated in a phantom experiment using a bottle containing a flask (inner diameter 38 mm) filled with perfluorooctyl bromide ($\text{CF}_3\text{-(CF}_2\text{)}_6\text{-CF}_2\text{Br}$) surrounded by water. The simultaneous $^{19}\text{F}/^1\text{H}$ 3D balanced UTE-SSFP sequence with Wong-type radial readout was implemented using a $^{19}\text{F}/^1\text{H}$ dual-tuned transmit/receive small-animal solenoid coil (inner diameter 7 cm) with the following parameters: FOV = 128 mm, matrix 128^3 , isotropic voxel $\Delta x = 1.0$ mm, $\alpha = 30^\circ$, excitation bandwidth $\text{exBW} = 5$ kHz centered on the PFOB- CF_2 line group, pixel bandwidth $\text{pBW} = 900$ Hz, TR = 2.1 ms, TE = 90 μs (FID sampling), $T_{\text{exp}} = 71$ s.

The effect of the balanced gradient scheme on sequence performance was determined by acquiring an additional 3D radial UTE gradient-echo (GRE) data set using identical acquisition parameters ($\alpha = 30^\circ$), but without balanced gradients (TR = 3.6 ms). Additionally, a 3D radial UTE GRE sequence at Ernst angle ($\alpha = 5^\circ$) was tested, following determination of the T_1 relaxation time for the PFOB- CF_2 line group (840 ms) (41). The GRE sequences do not apply RF spoiling, such that the signal may be optimized at $\alpha > \alpha_E$, depending on the actual T_2 relaxation time. Slab-selective (10 mm) serial spectroscopic acquisitions were employed on both the CF_2 and CF_3 line groups of the PFOB phantom to determine T_1 using inversion recovery, FID sampling, and variable TI delay (10-2810 ms in 200 ms steps), as well as apparent T_2' using spin-echo TE delay (13-53 ms in 2 ms steps for CF_2 and 13-583 ms in 30 ms steps for CF_3).

For comparison to existing techniques, 3D gradient-echo (GRE), balanced SSFP, and fast spin-echo (FSE) sequences with Cartesian k-space sampling were used with identical FOV (128 mm) and spatial resolution ($1 \times 1 \times 1 \text{ mm}^3$ voxels). An elliptical restriction of the two phase encoding dimensions was applied to the 3D Cartesian sampling such that the actually sampled portion of k-space was similar to the radial sampling in the UTE and balanced UTE-SSFP sequences. Other gradient-echo imaging parameters included $\alpha = 30^\circ$, $\text{exBW} = 5 \text{ kHz}$, $\text{pBW} = 900 \text{ Hz}$, $\text{TR/TE} = 4.8/2.1 \text{ ms}$, $T_{\text{exp}} = 104 \text{ s}$. Balanced SSFP was used with $\alpha = 30^\circ$, $\text{exBW} = 5 \text{ kHz}$, $\text{pBW} = 900 \text{ Hz}$, $\text{TR/TE} = 4.2/2.1 \text{ ms}$, $T_{\text{exp}} = 89 \text{ s}$. Fast spin-echo parameters included $\alpha = 90^\circ$, FSE acceleration factor 116, $\text{pBW} = 660 \text{ Hz}$, $\text{exBW} = 2830 \text{ Hz}$, $\text{TR/TE} = 4000/7.4 \text{ ms}$, $T_{\text{exp}} = 1032 \text{ s}$. For further comparison to alternative line selection methods (27), a fast spin-echo sequence was performed on the CF_3 line using the same FSE parameters.

3.2.3 Sensitivity Comparisons

In the phantom imaging experiments, sensitivity was selected as a metric to compare imaging techniques to take into account SNR as well as scan time for each sequence. Detection sensitivity (S) was defined and calculated as:

$$S = \frac{\text{SNR}}{(\text{mol/voxel}) \times \sqrt{T_{\text{exp}}}} \quad [3.1]$$

where SNR is the achieved signal-to-noise ratio, T_{exp} is the duration of the sequence, and (mol/voxel) is the amount of PFOB agent within an imaging voxel. To assess the signal-to-noise ratio, ^{19}F signal I_0 was measured on the magnitude image in a rectangular region of interest (ROI) within the PFOB phantom. Noise was determined from the standard deviations $\sigma[\text{Re}]$ and $\sigma[\text{Im}]$

in a rectangular ROI at the border of real and imaginary images. An area separated from the phantom and free of coherent background signal in any sequence type (e.g., by signal blurring) was chosen. From this data, SNR was calculated as:

$$\text{SNR} = \frac{I_0}{\sqrt{\sigma[\text{Re}]^2 + \sigma[\text{Im}]^2}} \quad [3.2]$$

3.2.4 *In Vivo* Imaging Experiment

For *in vivo* validation, targeted PFOB NPs were imaged in rabbit models of cancer and atherosclerosis. All animal procedures were approved by the Animal Studies Committee of Washington University in St. Louis.

Oncological applications of this sequence were investigated with Male New Zealand White rabbits (~2 kg, n = 4) that were implanted in the popliteal fossa of the left hind leg with 2-3 mm VX2 adenocarcinoma tumors (National Cancer Institute, MD), which grew to ~15 mm within 2 weeks (42). Imaging was performed 3h post-injection of 1.0 ml/kg $\alpha_v\beta_3$ -integrin targeted NP with PFOB core as previously described (43), either with or without Gd-DTPA-bisoleate incorporated on the outer layer. To avoid signal contamination from inhaled fluorinated anesthesia, a xylazine (10mg/kg) / ketamine (85 mg/kg) i.m. injection was used for anesthesia induction, which was maintained with a ketamine i.v. infusion (18 mg/kg/hr). The radial 3D balanced UTE-SSFP sequence was implemented using a $^{19}\text{F}/^1\text{H}$ dual-tuned transmit/receive surface coil (7×12 cm) with the following parameters: FOV = 140 mm, matrix 64^3 , isotropic voxel $\Delta x = 2.19$ mm, $\alpha = 30^\circ$, excitation bandwidth exBW = 5 kHz centered on the PFOB-CF₂ line group, pixel bandwidth pBW = 900 Hz, TR = 1.75 ms, TE = 90 μs (FID sampling), and a scanning time of 30 minutes.

Additionally, cardiovascular applications of this sequence were investigated by inducing atherosclerosis in Male New Zealand White rabbits, which were fed high cholesterol chow for 20 weeks. Imaging was performed 2h post-injection of 1.0 ml/kg of the $\alpha_v\beta_3$ -targeted PFOB-NP. The simultaneous $^{19}\text{F}/^1\text{H}$ balanced UTE-SSFP sequence with 3D radial readout was acquired at six time points post-injection with the following parameters: FOV = 140mm, matrix 112^3 , isotropic voxel $\Delta x = 1.25\text{mm}$, $\alpha = 30^\circ$, excitation bandwidth $\text{exBW} = 9\text{kHz}$, pixel bandwidth $\text{pBW} = 900\text{Hz}$, TR = 2.0ms, TE = 100 μs (FID sampling), and a total scan time of 28 minutes.

For the *in vivo* experiments, the radial k-space data were reconstructed at full resolution for the ^1H component, and a lower resolution with higher signal-to-noise for the ^{19}F component. The latter was achieved by applying a flat k-space weighting to the data outside a radius corresponding to a percentage of the fully sampled sphere in k-space (20% of the Nyquist radius for the adenocarcinoma-implanted rabbits; 7% of the Nyquist radius for the atherosclerotic rabbits) and using the usual quadratic weighting for the center of k-space (44). Since most signal intensity is located close to the center of k-space, flat weighting of higher k-values does not lead to signal losses but reduces noise amplification in high k-values and thus further improves SNR at the expense of spatial resolution.

3.3 Results

The balanced UTE-SSFP pulse sequence was successfully implemented and run on a 3T whole-body scanner. Figure 3.3 shows a magnitude image of the phantom bottle containing PFOB, acquired with the balanced UTE-SSFP sequence, with ROI drawn to show locations for measuring ^{19}F signal (I_0), and the location of the noise calculation that was performed on the real and imaginary images to calculate SNR as per Eq. 3.2.

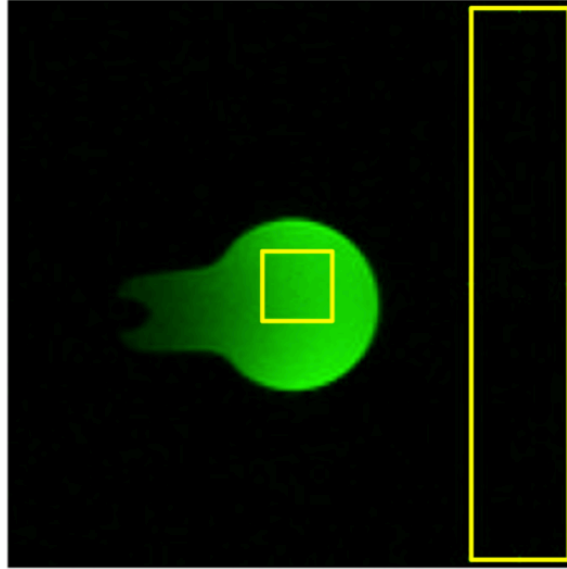


Figure 3.3 Magnitude ^{19}F image of sensitivity imaging phantom, showing PFOB signal acquired with balanced UTE-SSFP sequence. ROI show locations of ^{19}F signal (I_0) [middle], and noise [right] used for SNR calculations. [Figure reprinted from Goette et al. *In press*]

Table 3.1 summarizes the observed sensitivity for the investigated sequence types, as calculated by Eq. 3.1. With $S = 51 \mu\text{mol}_{\text{PFOB}}^{-1}\text{min}^{-1/2}$, the proposed balanced UTE-SSFP technique demonstrates a sensitivity of at least twice that of other sequence types. 3D UTE GRE sequences without balanced gradients at $\alpha = 30^\circ$ and $\alpha = 5^\circ$ (Ernst angle) exhibit substantially lower sensitivities (20 and $8 \mu\text{mol}_{\text{PFOB}}^{-1}\text{min}^{-1/2}$, respectively). Analysis of the spectroscopic series data revealed a T_1 of 840 ± 40 ms and 1000 ± 40 ms for the CF_2 and CF_3 peaks, respectively, and an apparent T_2' of 10 ± 1 ms and 230 ± 10 ms for the CF_2 and CF_3 peaks, respectively.

The second-best sequence is balanced SSFP with a Cartesian k-space trajectory ($23 \mu\text{mol}_{\text{PFOB}}^{-1}\text{min}^{-1/2}$), demonstrating the value of using balanced gradients for the detection of perfluorocarbons. For the CF_2 group, the proximate CS components lead to destructive signal overlay at larger echo times (e.g., 2.8 ms), which are difficult to separate with line selection techniques. The 3D gradient-echo acquisition demonstrates this signal loss ($\text{TE} = 2.1$ ms), with a measured sensitivity of $12 \mu\text{mol}_{\text{PFOB}}^{-1}\text{min}^{-1/2}$. Fast spin-echo techniques are typically highly SNR

efficient, but are not optimal for perfluorocarbons like PFOB ($16 \mu\text{mol}_{\text{PFOB}}^{-1}\text{min}^{-1/2}$), since the achievable echo times (here TE = 4.7 ms) do not allow full signal combination of the CF₂-group. Selecting the CF₃ group is possible, but this choice only uses 3 of the 17 available fluorine nuclei, which resulted in lowered sensitivity ($7 \mu\text{mol}_{\text{PFOB}}^{-1}\text{min}^{-1/2}$).

Table 3.1 Sensitivity of ¹⁹F MR Acquisition Techniques

PFOB Line(s)	¹⁹ F Sequence	Sensitivity ($\mu\text{mol}_{\text{PFOB}}^{-1}\text{min}^{-1/2}$) ^a
CF ₃	Cartesian fast spin-echo	7
	Cartesian gradient-echo ($\alpha=30^\circ$)	12
(CF ₂) ₆	Cartesian fast spin-echo	16
	Cartesian balanced SSFP ($\alpha=30^\circ$)	23
	Radial UTE gradient-echo ($\alpha=5^\circ$) ^b	8
	Radial UTE gradient-echo ($\alpha=30^\circ$)	20
	Radial balanced UTE-SSFP ($\alpha=30^\circ$)	51

^aSensitivity measured as $S = \text{SNR} \times (\text{mol}/\text{voxel})^{-1} \times T_{\text{exp}}^{-1/2}$, where SNR is the achieved signal-to-noise ratio, T_{exp} the sequence duration, and (mol/voxel) the amount of PFOB agent within an imaging voxel.

^bErnst angle calculated as $\alpha = \cos^{-1}(\exp(-\text{TR}/T_1))$, where TR = 3.6 ms, and T_1 was measured at 840 ms.

In vivo imaging of angiogenesis-targeted PFOB nanoparticles was successful in a rabbit model of cancer, demonstrating heterogeneous areas of neovasculature at the tumor rim (Fig. 3.4a&d, arrows) as expected in this established VX2 tumor model. On ¹H images, the bound nanoparticles that carry Gd give rise to T₁-based signal enhancement (Fig. 3.4d), whereas the Gd-free NP are invisible in ¹H MRI (Fig. 3.4a). The fluorinated core of this PFOB NP emulsion was imaged with the simultaneous ¹⁹F/¹H balanced UTE-SSFP sequence using parameters that were tested in the phantom experiment. For PFOB-NP both without and with Gd, the resultant ¹⁹F signal clearly elucidates the heterogeneous distribution of detected NP (Fig. 3.4b&e, respectively), which is overlaid on ¹H anatomy to demonstrate anatomical co-localization (Fig. 3.4c&f).

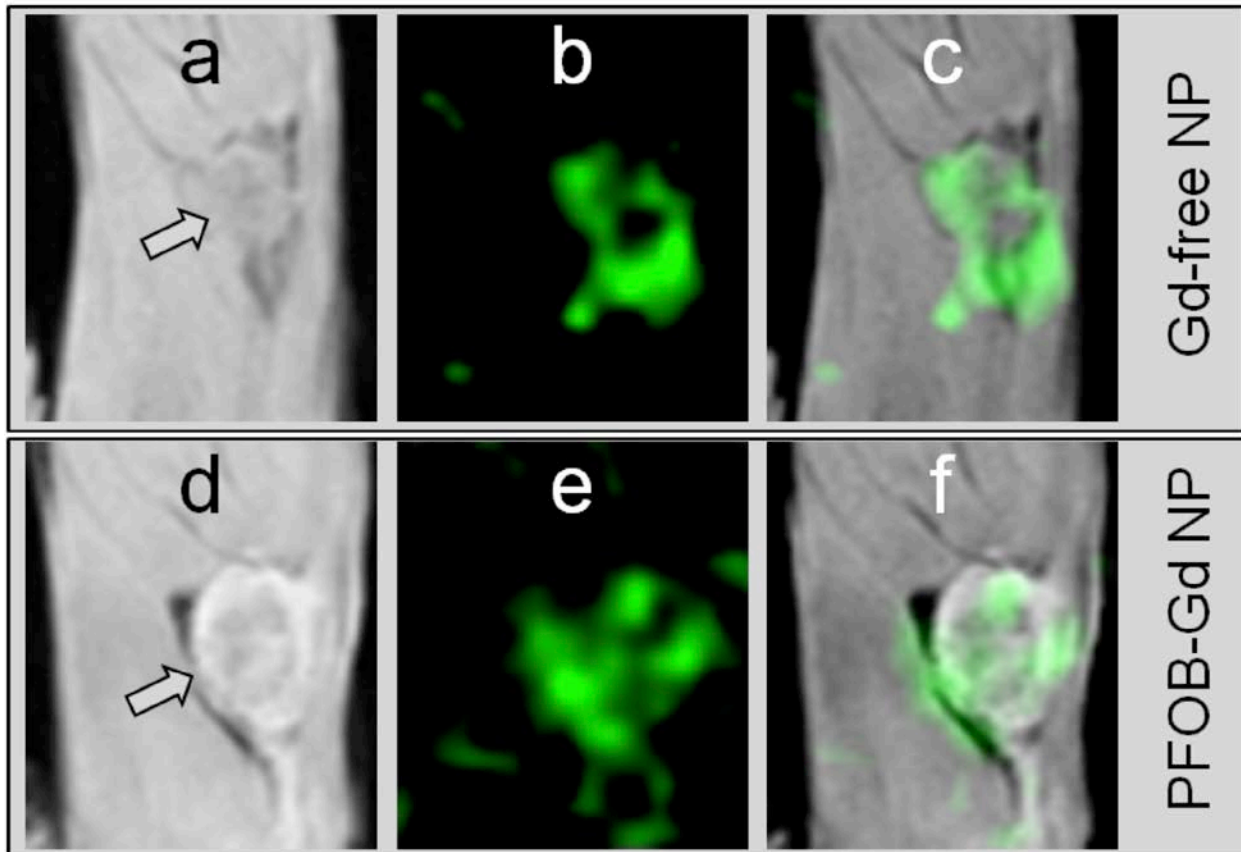


Figure 3.4 Molecular imaging of $\alpha_v\beta_3$ -integrin targeted NP on VX2 tumors (arrows) in rabbits by ^{19}F MRI. Gd-free (a,b,c) or Gd-containing (d,e,f) NP with a perfluorooctyl bromide (PFOB) core were used and imaged with a novel balanced UTE-SSFP based 3D radial sequence. ^1H images show T₁-based enhancement only with Gd NP (d), while the ^{19}F signal is clearly detected in both cases (b&e). Image overlays (c&f) demonstrate the anatomical co-localization. [Figure reprinted from Goette et al. *In press*]

In vivo imaging of atherosclerosis with angiogenesis-targeted PFOB nanoparticles was also successful using the $^{19}\text{F}/^1\text{H}$ balanced UTE-SSFP sequence. Figure 3.5a shows an example of the proton image quality in a selected slice at the aorta, which is robust against motion due to the simultaneous 3D radial acquisition. The isotropic voxels allow multi-planar reformatting for visualizing anatomy and prescribing ROIs for analyzing the directly corresponding ^{19}F NP signal. In this example, $\alpha_v\beta_3$ -targeted PFOB-NP were detected in the aorta ROI (Fig. 3.5b) in concentrations ranging from 10 to 16 mM.

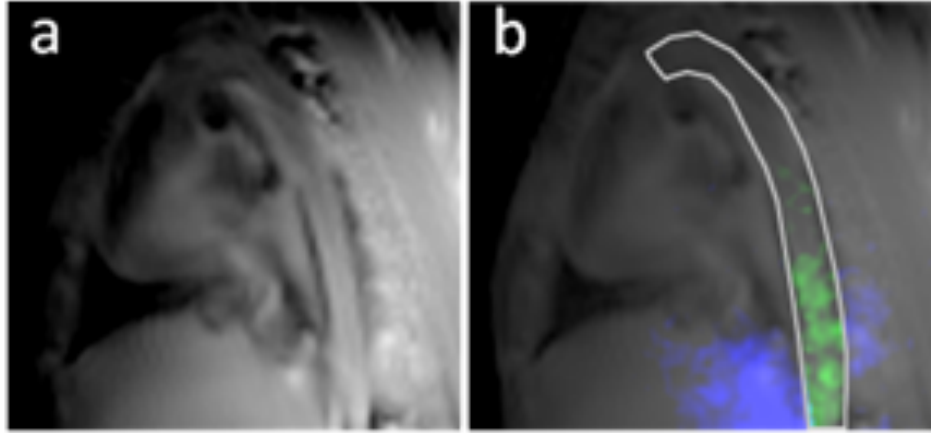


Figure 3.5 Simultaneous $^{19}\text{F}/^1\text{H}$ molecular imaging of angiogenesis targeted perfluorooctyl bromide nanoparticles in a rabbit model of atherosclerosis using 3D radial balanced UTE-SSFP. Proton image (a) with 1.25 mm isotropic voxels show anatomy, upon which ^{19}F image can be overlaid (b). The ROI in (b) is surrounding the aorta, which has a diameter of about 5 mm. The ^{19}F overlay within the aortic region is in green, and extra-aortic ^{19}F signal is blue.

3.4 Discussion

This study introduced and tested a novel pulse sequence, $^{19}\text{F}/^1\text{H}$ balanced UTE-SSFP with 3D radial readout, for the imaging of non-proton nuclei with complex spectra. The sequence was implemented on a clinical 3T scanner to enable detection of multi-resonant fluorine imaging labels like PFOB with high sensitivity as compared to traditional techniques. A majority of the PFOB fluorine nuclei (12 of 17) are located in the CF_2 resonances, which are distributed over a wide chemical shift range. Within the $90\ \mu\text{s}$ echo time of the balanced UTE-SSFP sequence however, we showed that dephasing does not lead to destructive superposition of these resonances, which serves to maximize the obtained signal. The signal gain by constructive addition of all CF_2 lines over-compensates the loss in SNR-efficiency imposed by 3D radial sampling (25%) and the FID readout, which requires twice the number of k-space lines, since all start at $k_{x,y,z} = 0$ (45). Point-spread function effects of the k-space sampling might change the actually sampled voxel volume and thus influence the sensitivity comparison. Because of the

chosen elliptical restriction of the phase encoding in Cartesian sampling, these effects were considered to be negligible.

The sensitivity obtained for the spoiled gradient-echo sequence using radial UTE readout allows separating the contributions of short echo times (reduced dephasing) and the use of balanced gradients. Without the spoiler gradients used in GRE, TR is decreased for the balanced case, which accounts for about 30% of the observed sensitivity gain (20 to 51 $\mu\text{mol}_{\text{PFOB}}^{-1}\text{min}^{-1/2}$). Thus, the application of balanced gradients can be estimated to result in a twofold sensitivity gain for the CF_2 line group. This result is similar to the sensitivity gain found by introducing balanced gradients in the Cartesian CF_2 acquisitions (12 to 23 $\mu\text{mol}_{\text{PFOB}}^{-1}\text{min}^{-1/2}$).

The experimental results show a substantial, 2.5-fold increase in the UTE GRE signal from Ernst angle ($\alpha_E = 5^\circ$ for $T_1 = 840$ ms) to $\alpha = 30^\circ$. According to GRE signal theory without RF spoiling (see e.g. (46), Eq. 4.22, $\text{TR} = 4.8$ ms, $T_1 = 840$ ms) this is only expected for species with actual T_2 values much larger than the measured apparent T_2' of 10 ms (consistent with (25)). At an estimated actual T_2 of 110 ms, the GRE signal theory predicts a 2.5-fold signal increase when changing from $\alpha = 5^\circ$ to 30° , while the signal gain would be lower at any significantly shorter T_2 . The apparent T_2' , as measured by multiple spin echo times, is known to be strongly influenced and shortened by homonuclear J-coupling (25). Recent work by Jacoby et al. (19) demonstrates this point, measuring the T_2 of emulsified PFOB, which varies over the CF_2 peaks from 75 to 80 ms; however, the narrow band excitation and refocusing used by this group likely does not completely eliminate the effects of J-coupling, leading to a measured T_2 that is still shorter than the actual T_2 of the CF_2 peaks. Additionally, Giraudeau et al. (27) have shown exceptionally high actual T_2 values of 400 to 900 ms for the PFOB CF_3 group when using narrow band refocussing in spin-echo to reduce J-coupling effects. Interestingly, the T_2 is shown

to increase at shorter echo time, which is hypothesized to be due to a reduced influence of the coupled (quantum) state on relaxation at shorter TE. Furthermore, the actual T_2 , and hence signal, depends on whether the PFOB is neat, encapsulated, or bound to a target (19,27). Our results suggest that an actual T_2 value (and not apparent T_2') is required to correctly model the signal gain obtained by flip angle optimization and by applying balanced gradients.

To further elucidate the cause for this observed signal increase in the balanced UTE-SSFP sequence, signal models (M_T denoting the modeled transverse magnetization) were generated for GRE (N-FFE, FAST, GRASS, FISP), balanced SSFP (B-FFE, R-FFE, true FISP), as well as RF spoiled GRE (T_1 -FFE, FLASH, SPGR) according to Vlaardingerbroek et al. (46) as follows:

$$E_1 = e^{-TR/T_1} \quad [3.3]$$

$$E_2 = e^{-TR/T_2} \quad [3.4]$$

GRE (N-FFE, FAST, GRASS, FISP) [Eq. 4.22 from (46)]:

$$M_T = \sin \alpha / (\cos \alpha + 1) * \left[(1 + \cos \alpha - A) / \sqrt{A^2 + B^2 + 1} \right] \quad [3.5]$$

$$A = [1 - E_1 * E_2^2 + \cos \alpha * (E_2^2 - E_1)] / (1 - E_1) \quad [3.6]$$

$$B = (1 + \cos \alpha) * E_2 \quad [3.7]$$

Balanced SSFP (B-FFE, R-FFE, true FISP) [Eq. 4.24 from (46)]:

$$M_T = \sin \alpha * (1 - E_1) / (1 - E_1 \cos \alpha - E_2 * (E_1 - \cos \alpha)) \quad [3.8]$$

RF-spoiled GRE (T_1 -FFE, FLASH, SPGR) [Eq. 4.16 from (46)]:

$$M_T = \sin \alpha * (1 - E_1) / (1 - E_1 \cos \alpha) \quad [3.9]$$

Figure 3.6 shows the result of this signal modeling, with transverse magnetization (M_T) plotted as a function of flip angle (α , degrees), using the measured T_1 of the PFOB CF_2 line group (840 ms) and the estimated actual T_2 of 110 ms. A 50% gain in signal is observed in the balanced SSFP (R-FFE) signal model at $\alpha = 30^\circ$, compared to the gradient echo signal (GRE, N-FFE). With RF-spoiled GRE (T_1 -FFE), the maximum signal occurs at the Ernst angle as expected; however, GRE remains rather T_2 -dependent, so the Ernst angle does not apply for this signal model. For the steady-state signal in both GRE and balanced SSFP, only the actual T_2 decay (not apparent T_2') is relevant for the signal build-up. This is because J-coupling only leads to destructive interference in the sum of the splitted components, but not to an accelerated relaxation of the transverse magnetization of each component.

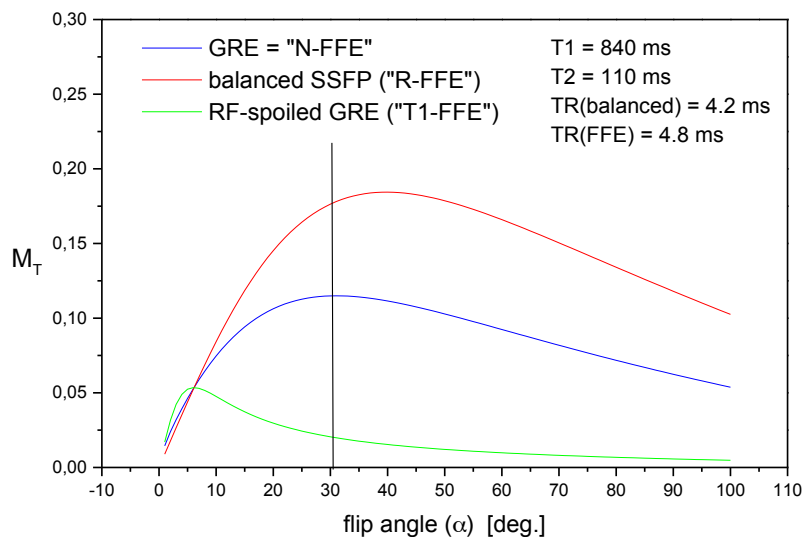


Figure 3.6 Modeled steady-state gradient echo signal as a function of flip angle (α) for balanced SSFP ("R-FFE", red line), GRE ("N-FFE", blue line), and RF-spoiled GRE ("T₁-FFE", green line) using an estimated actual T_2 of 110 ms.

The flip angle choice of $\alpha = 30^\circ$ in the present study was suggested by a previous study using a Cartesian GRE sequence on fibrin target bound PFOB nanoparticles (47), which showed a signal optimum at $\alpha = 30^\circ$ to 35° and a signal decay for larger flip angles. While a sequence comparison at a fixed flip angle, as performed in this study, is clearly demonstrating the respective signal gain by using ultra short echo time and balanced gradients, the individual optimum flip angle for each sequence type was not explored. Inserting the estimated actual T_2 of 110 ms (neat PFOB) into the signal theory for balanced SSFP (Eq. 3.8) allows one to estimate an optimum flip angle and to predict the signal gain by introducing balanced gradients as compared to GRE. According to this theory, balanced gradients at $\alpha = 30^\circ$ resulted in a 50% signal increase and the signal maximum would be expected at 40° , as seen in Figure 3.6. The actually observed signal gain (twofold) does not match this calculation, likely due to the fact that the actual T_2 is not well known and may depend on sequence parameters. A more detailed analysis of the actual T_2 relaxation of the PFOB CF_2 line group for neat and encapsulated PFOB forms would provide important information to optimize balanced UTE-SSFP sequences (e.g. flip angle choice). A flip angle of 30° could be a practical choice for in vivo applications of the proposed balanced UTE-SSFP technique for PFOB loaded nanoparticles, where T_2 relaxation may be faster due to restricted motion. The current parameter choice in balanced UTE-SSFP led to the successful observation of $\alpha_v\beta_3$ -integrin targeted NP with a PFOB core, as shown in the VX2 tumor model.

Although the focus of this work was on PFOB nanoparticle emulsions, the balanced UTE-SSFP technique offers several benefits for multinuclear imaging of many non-proton agents, such as perfluorodecalin ($C_{10}F_{18}$) or perfluorooctane (C_8F_{18}) (19,48). This pulse sequence is optimal for contrast agents with a short apparent T_2' relaxation, due to the ultra-short echo time and fast FID acquisition. Agents bound to molecular targets may be of particular interest,

since they exhibit reduced T_2' relaxation due to decreased molecular motion (47). In addition, the balanced SSFP approach yields high SNR, in particular for imaging labels with characteristically unfavorable long T_1 relaxation for gradient-echo methods due to M_0 saturation, as is the case with PFOB. Although T_1 -shortening of Gd has been shown to be beneficial in fluorine imaging, the balanced UTE sequence provides high signal even for PFOB-NP without Gd with a T_1 of about 1 second. Moreover, the balanced gradient technique is advantageous for the detection of agents with complex spectra due to the elimination of extraneous gradient-induced line dephasing. The combination of these two schemes offers a flexible pulse sequence for complex resonant structures, which can be customized to the agent of choice by altering offset frequency and excitation bandwidth to dial in a particular line group.

As shown in this study, the proposed balanced UTE-SSFP sequence can be combined with simultaneous dual-nuclei techniques for efficient anatomical localization and quantitative calibration of the non-proton signal. Once the complex spectral signal is acquired with this sequence, the 3D radially-filled k-space data can be directly reconstructed, and does not require post-processing as would chemical shift imaging. As an added benefit, the 3D radial data set offers the potential for multi-resolution reconstruction, allowing analysis of the ^{19}F and ^1H data at different spatial resolution (44). Note that the reconstruction of the ^{19}F data at a lower resolution and higher SNR was only performed for the in vivo experiment to demonstrate this capability in sparse molecular imaging environments; all ^{19}F data were reconstructed at full resolution in the phantom experiments when comparing balanced UTE-SSFP to existing techniques. Finally, this unique simultaneously acquired data provides an opportunity for motion correction of the non-proton signal with temporal sub-sampling of the ^1H data (38). Although a prototype dual $^{19}\text{F}/^1\text{H}$ spectrometer system was used for simultaneous acquisition in this study, a

similar ^{19}F UTE-SSFP sequence was also successfully implemented on a standard multinuclear scanner platform.

In this study, the balanced UTE-SSFP sequence was shown to be more sensitive than traditional acquisition techniques in the context of multinuclear imaging of contrast agents with short T_2 and complex spectra. However, some agents may not require advanced line combination, such as those with single resonance peaks. Application of the balanced UTE-SSFP sequence for such agents might result in decreased SNR-efficiency due to the 3D radial sampling and FID readout. In addition, the bandwidth of this technique may not be large enough to cover all lines of an agent, because of the large chemical shifts found in ^{19}F . Thus, a particular line group must be selected within a bandwidth of approximately 1-2 kHz, for an appropriate spatial resolution of the 3D radial readout with standard gradient systems. While advantageous for the detection of PFOB since a majority of ^{19}F spins are found in the CF_2 line group covering ~ 1 kHz, this bandwidth restriction may be a limitation for other chemical species. Another obstacle for this sequence was found in the classic balanced SSFP banding artifacts that were observed in both the ^1H and ^{19}F components in some images, but these were reduced by shortening TR and can be moved out of the region of interest by adjusting the offset frequency for the balanced signal.

3.5 Conclusion

Radial 3D balanced UTE-SSFP is a robust pulse sequence that yields high SNR, with detection sensitivity more than two-fold improved over more traditional techniques, while also alleviating problems associated with extended longitudinal relaxation times, short apparent T_2' , and complex spectral properties of imaging agents. This technique was demonstrated for dual-frequency $^{19}\text{F}/^1\text{H}$ MRI on a clinical scanner that allows highly sensitive *in vivo* detection of

multi-resonant imaging labels like perfluorooctyl bromide, which could play a central role in human translation of ^{19}F MR-based targeted molecular imaging. The synergistic combination of an optimized imaging technique and a gadolinium-free, biocompatible contrast agent should facilitate translation into clinical use.

3.6 Acknowledgements

I would like to thank the co-authors of the following manuscript: Goette MJ, Keupp J, Rahmer J, Lanza GM, Wickline SA, Caruthers SD. Balanced UTE-SSFP for ^{19}F MR Imaging of Complex Spectra. *Magn Reson Med*. *In press*. My role in the work was to develop the balanced UTE-SSFP sequence with Philips scientists Drs. Keupp, Rahmer, and Caruthers, test the sequence with the *in vivo* rabbit model of atherosclerosis, assemble all data and figures, and write the manuscript. I would also like to thank Todd A. Williams and John S. Allen for their help performing the animal experiments, and Angana Senpan for her help preparing the PFC NP emulsion.

3.7 References

1. Wijnen JP, van der Kemp WJ, Luttje MP, Korteweg MA, Luijten PR, Klomp DW. Quantitative ^{31}P magnetic resonance spectroscopy of the human breast at 7 T. *Magn Reson Med* 2012;68(2):339-348.
2. Li X, Majumdar S. Quantitative MRI of articular cartilage and its clinical applications. *J Magn Reson Imaging* 2013;38(5):991-1008.

3. Fan X, River JN, Muresan AS, Popescu C, Zamora M, Culp RM, Karczmar GS. MRI of perfluorocarbon emulsion kinetics in rodent mammary tumours. *Phys Med Biol* 2006;51(2):211-220.
4. Mills GH, Wild JM, Eberle B, Van Beek EJ. Functional magnetic resonance imaging of the lung. *Br J Anaesth* 2003;91(1):16-30.
5. Fain SB, Korosec FR, Holmes JH, O'Halloran R, Sorkness RL, Grist TM. Functional lung imaging using hyperpolarized gas MRI. *J Magn Reson Imaging* 2007;25(5):910-923.
6. Winter PM, Cai K, Caruthers SD, Wickline SA, Lanza GM. Emerging nanomedicine opportunities with perfluorocarbon nanoparticles. *Expert Rev Med Devic* 2007;4(2):137-145.
7. Ahrens ET, Flores R, Xu HY, Morel PA. In vivo imaging platform for tracking immunotherapeutic cells. *Nat Biotechnol* 2005;23(8):983-987.
8. Crowder KC, Hughes MS, Marsh JN, Barbieri AM, Fuhrhop RW, Lanza GM, Wickline SA. Sonic activation of molecularly-targeted nanoparticles accelerates transmembrane lipid delivery to cancer cells through contact-mediated mechanisms: Implications for enhanced local drug delivery. *Ultrasound Med Biol* 2005;31(12):1693-1700.
9. Ahrens ET, Zhong J. In vivo MRI cell tracking using perfluorocarbon probes and fluorine-19 detection. *NMR Biomed* 2013;26(7):860-871.
10. Carmeliet P. Mechanisms of angiogenesis and arteriogenesis. *Nat Med* 2000;6(4):389-395.
11. Morawski AM, Lanza GA, Wickline SA. Targeted contrast agents for magnetic resonance imaging and ultrasound. *Curr Opin Biotech* 2005;16(1 SPEC. ISS.):89-92.

12. Winter PM, Caruthers SD, Allen JS, Cai K, Williams TA, Lanza GM, Wickline SA. Molecular imaging of angiogenic therapy in peripheral vascular disease with $\alpha v\beta 3$ -integrin-targeted nanoparticles. *Magn Reson Med* 2010;64(2):369-376.
13. Schmieder AH, Caruthers SD, Zhang H, Williams TA, Robertson JD, Wickline SA, Lanza GM. Three-dimensional MR mapping of angiogenesis with $\alpha 5\beta 1(\alpha v\beta 3)$ -targeted theranostic nanoparticles in the MDA-MB-435 xenograft mouse model. *FASEB J* 2008;22(12):4179-4189.
14. Giraudeau C, Geffroy F, Meriaux S, Boumezbeur F, Robert P, Port M, Robic C, Le Bihan D, Lethimonnier F, Valette J. ^{19}F molecular MR imaging for detection of brain tumor angiogenesis: in vivo validation using targeted PFOB nanoparticles. *Angiogenesis* 2013;16(1):171-179.
15. Yu JX, Kodibagkar VD, Cui WN, Mason RP. F-19: A versatile reporter for non-invasive physiology and pharmacology using magnetic resonance. *Curr Med Chem* 2005;12(7):819-848.
16. Morawski AM, Winter PM, Yu X, Fuhrhop RW, Scott MJ, Hockett F, Robertson JD, Gaffney PJ, Lanza GM, Wickline SA. Quantitative "magnetic resonance immunohistochemistry" with ligand-targeted ^{19}F nanoparticles. *Magn Reson Med* 2004;52(6):1255-1262.
17. Keupp J, Caruthers SD, Rahmer J, Williams TA, Wickline SA, Lanza GM. Fluorine-19 MR molecular imaging of angiogenesis on Vx-2 tumors in rabbits using $\alpha v\beta 3$ -targeted nanoparticles. In Proceedings of the 17th Annual Meeting of ISMRM, Honolulu, Hawaii, USA, 2009. p. 223.

18. Ruiz-Cabello J, Barnett BP, Bottomley PA, Bulte JW. Fluorine (¹⁹F) MRS and MRI in biomedicine. *NMR Biomed* 2011;24(2):114-129.
19. Jacoby C, Temme S, Mayenfels F, Benoit N, Krafft MP, Schubert R, Schrader J, Flogel U. Probing different perfluorocarbons for in vivo inflammation imaging by ¹⁹F MRI: image reconstruction, biological half-lives and sensitivity. *NMR Biomed* 2014;27(3):261-271.
20. Lee H, Price RR, Holburn GE, Partain CL, Adams MD, Cacheris WP. In vivo fluorine-19 MR imaging: relaxation enhancement with Gd-DTPA. *J Magn Reson Imaging* 1994;4(4):609-613.
21. Neubauer AM, Myerson J, Caruthers SD, Hockett FD, Winter PM, Chen JJ, Gaffney PJ, Robertson JD, Lanza GM, Wickline SA. Gadolinium-Modulated F-19 Signals From Perfluorocarbon Nanoparticles as a New Strategy for Molecular Imaging. *Magn Reson Med* 2008;60(5):1066-1072.
22. Sadowski EA, Bennett LK, Chan MR, Wentland AL, Garrett AL, Garrett RW, Djamali A. Nephrogenic systemic fibrosis: risk factors and incidence estimation. *Radiology* 2007;243(1):148-157.
23. Boyd AS, Zic JA, Abraham JL. Gadolinium deposition in nephrogenic fibrosing dermopathy. *J Am Acad Dermatol* 2007;56(1):27-30.
24. Grobner T. Gadolinium—a specific trigger for the development of nephrogenic fibrosing dermopathy and nephrogenic systemic fibrosis? *Nephrol Dial Transplant* 2006;21(4):1104-1108.

25. Sotak CH, Hees PS, Huang HN, Hung MH, Krespan CG, Raynolds S. A new perfluorocarbon for use in fluorine-19 magnetic resonance imaging and spectroscopy. *Magn Reson Med* 1993;29(2):188-195.
26. Mastropietro A, De Bernardi E, Breschi GL, Zucca I, Cametti M, Soffientini CD, de Curtis M, Terraneo G, Metrangolo P, Spreafico R, Resnati G, Baselli G. Optimization of rapid acquisition with relaxation enhancement (RARE) pulse sequence parameters for ¹⁹F-MRI studies. *J Magn Reson Imaging* 2013. doi 10.1002/jmri.24347.
27. Giraudeau C, Flament J, Marty B, Boumezbeur F, Meriaux S, Robic C, Port M, Tsapis N, Fattal E, Giacomini E, Lethimonnier F, Le Bihan D, Valette J. A new paradigm for high-sensitivity ¹⁹F magnetic resonance imaging of perfluorooctylbromide. *Magn Reson Med* 2010;63(4):1119-1124.
28. Reeder SB, Wen Z, Yu H, Pineda AR, Gold GE, Markl M, Pelc NJ. Multicoil Dixon chemical species separation with an iterative least-squares estimation method. *Magn Reson Med* 2004;51(1):35-45.
29. Yu H, Shimakawa A, McKenzie CA, Brodsky E, Brittain JH, Reeder SB. Multiecho water-fat separation and simultaneous R2* estimation with multifrequency fat spectrum modeling. *Magn Reson Med* 2008;60(5):1122-1134.
30. Keupp J, Schaeffter T. Efficient ¹⁹F imaging of multi-spectral-line contrast agents: aliasing serves to minimize time encoding. In *Proceedings of the 14th Annual Meeting of ISMRM, Seattle, Washington, USA, 2006*. p. 913.
31. Keupp J, Wickline SA, Lanza GM, Caruthers SD. Hadamard-type pulse-phase encoding for imaging of multi-resonant fluorine-19 nanoparticles in targeted molecular MRI. In *Proceedings of the 18th Annual Meeting of ISMRM, Stockholm, Sweden, 2010*. p. 982.

32. Yildirim M, Keupp J, Nicolay K, Lamerichs R. Chemical shift independent imaging of ¹⁹F contrast agents using ultrafast MRSI (F-uTSI). In Proceedings of the 15th Annual Meeting of ISMRM, Berlin, Germany, 2007. p. 1249.
33. Lamerichs R, Yildirim M, Nederveen AJ, Stoker J, Lanza GM, Wickline SA, Caruthers SD. In vivo 3D ¹⁹F fast spectroscopic imaging (F-uTSI) of angiogenesis on Vx-2 tumors in rabbits using targeted perfluorocarbon emulsions. In Proceedings of the 18th Annual Meeting of ISMRM, Stockholm, Sweden, 2010. p. 457.
34. Rahmer J, Bornert P, Groen J, Bos C. Three-dimensional radial ultrashort echo-time imaging with T2 adapted sampling. *Magn Reson Med* 2006;55(5):1075-1082.
35. Schmid F, Holtke C, Parker D, Faber C. Boosting ¹⁹F MRI—SNR efficient detection of paramagnetic contrast agents using ultrafast sequences. *Magn Reson Med* 2013;69(4):1056-1062.
36. Scheffler K, Lehnhardt S. Principles and applications of balanced SSFP techniques. *Eur Radiol* 2003;13(11):2409-2418.
37. Lee HK, Nalcioglu O, Buxton RB. Correction of chemical-shift artifacts in ¹⁹F imaging of PFOB: a robust signed magnitude method. *Magn Reson Med* 1992;23(2):254-263.
38. Keupp J, Rahmer J, Grässlin I, Mazurkewitz PC, Schaeffter T, Lanza GM, Wickline SA, Caruthers SD. Simultaneous dual-nuclei imaging for motion corrected detection and quantification of ¹⁹F imaging agents. *Magn Reson Med* 2011;66(4):1116-1122.
39. Wong STS, Roos MS. A strategy for sampling on a sphere applied to 3D selective RF pulse design. *Magn Reson Med* 1994;32(6):778-784.

40. Hockett FD, Wallace KD, Schmieder AH, Caruthers SD, Pham CTN, Wickline SA, Lanza GM. Simultaneous dual frequency 1H and 19F open coil imaging of arthritic rabbit knee at 3T. *IEEE T Med Imaging* 2011;30(1):22-27.
41. Ernst RR, Anderson WA. Application of Fourier Transform Spectroscopy to Magnetic Resonance. *Rev Sci Instrum* 1966;37(1):93-102.
42. Hu G, Lijowski M, Zhang H, Partlow KC, Caruthers SD, Kiefer G, Gulyas G, Athey P, Scott MJ, Wickline SA, Lanza GM. Imaging of Vx-2 rabbit tumors with $\alpha v\beta 3$ - integrin-targeted 111In nanoparticles. *Int J Cancer* 2007;120(9):1951-1957.
43. Neubauer AM, Caruthers SD, Hockett FD, Cyrus T, Robertson JD, Allen JS, Williams TD, Fuhrhop RW, Lanza GM, Wickline SA. Fluorine cardiovascular magnetic resonance angiography in vivo at 1.5 T with perfluorocarbon nanoparticle contrast agents. *J Cardio Magn Reson* 2007;9(3):565-573.
44. Rahmer J, Keupp J, Caruthers SD, Lips O, Williams TA, Wickline SA, Lanza GM. Dual resolution simultaneous 19F/1H in vivo imaging of targeted nanoparticles. In *Proceedings of the 17th Annual Meeting of ISMRM, Honolulu, Hawaii, USA, 2009*. p. 612.
45. Lauzon ML, Rutt BK. Effects of polar sampling in k-space. *Magn Reson Med* 1996;36(6):940-949.
46. Vlaardingerbroek MT, Boer JAd. *Magnetic resonance imaging : theory and practice*. New York, NY: Springer; 2003. 499 p.
47. Keupp J, Schmieder AH, Wickline SA, Lanza GM, Caruthers SD. Target-binding of perfluoro-carbon nanoparticles alters optimal imaging parameters using F-19 molecular

- MRI: a study using fast in vitro screening and in vivo tumor models. In Proceedings of the 18th Annual Meeting of ISMRM, Stockholm, Sweden, 2010. p. 1929.
48. Srinivas M, Cruz LJ, Bonetto F, Heerschap A, Figdor CG, de Vries IJ. Customizable, multi-functional fluorocarbon nanoparticles for quantitative in vivo imaging using ^{19}F MRI and optical imaging. *Biomaterials* 2010;31(27):7070-7077.

Chapter 4. Improved Quantitative ^{19}F MR Molecular Imaging with Flip Angle Calibration and B_1 -Mapping Compensation

4.1 Introduction

MR molecular imaging with the use of ligand-targeted contrast agents has proven capable of noninvasively detecting the presence of cellular indicators of biological processes for many classes of pathologies (1-4). Common exogenous contrast mechanisms have employed either paramagnetic or superparamagnetic readouts based on the composition of the core materials of nanoparticulate agents that function by altering the local relaxation properties of protons in T_1 or T_2/T_2^* weighted images to reveal local changes in MRI contrast indicative of a binding event (5). Of the paramagnetic agents, one of the first to become useful for a broad range of imaging applications was a perfluorocarbon core nanoparticle decorated with several hundred thousand gadolinium atoms with the use of conventional chelating chemistries, and a smaller population of molecular targeting ligands (e.g., antibodies, small molecules, peptides, etc.) covalently coupled into a surrounding lipid/surfactant monolayer (6-9). Further model-based efforts have been pursued to quantify these sparse binding events in attempts to compute the concentrations of the targeted epitopes (10). Yet all of these approaches that rely on indirect readouts of binding through altered proton relaxation suffer from high background proton signals, susceptibility artifacts (11), potential toxicities of the contrast agent itself (12,13), and most importantly, the need for both pre- and post-contrast images to accurately delineate *changes* in local contrast (14,15).

For some time, it has been appreciated that the ability to create local MRI contrast based on detection of alternative nuclei such as fluorine (^{19}F) might offer a direct and quantifiable

readout of molecular binding events (16-18). Fluorine exhibits well-known advantages of being a high signal nucleus with a natural abundance of its stable isotope, favorable toxicity profiles, a convenient gyromagnetic ratio close to that of protons (D: ~6%) (19), and a unique spectral signature with no detectable background at clinical field strengths (20). However, clinical development of this approach has been slowed by the need to deposit sufficient concentrations of the contrast material within a voxel to yield a detectable signal, and by the lack of imaging hardware and software (e.g., coils, multinuclear spectrometers, pulse sequences, etc.). Over the past 15 years, our own efforts in ^{19}F contrast agent development and imaging at 1.5 and 3T with the assistance of commercial partners have yielded translatable solutions to many of these imaging hardware needs (21,22), while simultaneously validating the utility of the PFC-core nanoparticle agents as targetable molecular imaging probes (23-25).

However, for ^{19}F MRI to mature as a truly robust whole body detection approach for quantifying molecular binding events noninvasively, additional obstacles must be overcome. Although ^{19}F MRI is potentially quantitative in nature because ^{19}F spin density (and signal) is linearly correlated to the deposition and resultant concentration PFC NPs at a particular site in the body (17), the imaging chain of a clinical MR system comprises many steps that can confound absolute signal calibration, even when specialized transmit/receive (T/R) coils are used (26). Coil tuning and RF drive power (i.e., flip angle) settings must be calibrated and center frequency determined for ^{19}F tracers that are in miniscule concentrations lending little signal on which to perform these measures that drive not only image quality, but ultimately accuracy. ^{19}F MRI also is susceptible to imaging artifacts, such as motion, partial volume, and eddy currents, all of which can degrade image quality and produce quantification errors (21). Lastly, B_1 -field inhomogeneities that are inherent to many transmit and receive RF coils must be accounted for

(27,28). Because the concentration of PFC NPs within a voxel is determined by a comparison to an external standard of known ^{19}F concentration, local differences in the B_1 field between the targeted region of interest and the location of the standard may lead to errors in the quantified ^{19}F signal.

This study pursues additional measures that are intended to improve accuracy for in vivo quantitative ^{19}F MR molecular imaging, including flip angle calibration (between the relevant ^1H and ^{19}F nuclei of interest), and B_1 field mapping compensation to offset anticipated RF inhomogeneities. Herein, we hypothesize that the RF power settings that are typically optimized for ^1H might also be used to determine the correct RF power settings for ^{19}F signals acquired with $^{19}\text{F}/^1\text{H}$ dual-tuned RF coils. Furthermore, a solution to overcome inhomogeneities associated with RF coils is proposed that relies on mapping the B_1 field on the ^1H signal and then performing an image-based correction to the ^{19}F and ^1H data by signal modeling, which is then tested in phantom and in vivo experiments in a cancer model in rabbits for tumor angiogenesis targeting.

4.2 Methods

4.2.1 Magnetic Resonance Spectroscopy

All magnetic resonance spectroscopy and imaging data were acquired on a 3T clinical whole-body scanner (Achieva, Philips Healthcare, The Netherlands) with a dual $^{19}\text{F}/^1\text{H}$ spectrometer system (21). Dual-resonant $^{19}\text{F}/^1\text{H}$ RF coils were used, which can either transmit or receive at both resonance frequencies simultaneously (29). Three dual-tuned coils were used for the MRS experiment including a single loop rectangular surface coil (7×12 cm, Philips Healthcare, The Netherlands), a custom-built semi-cylindrical coil (13 cm diameter, 15 cm

length), and a custom-built single-turn solenoid coil (11.5 cm diameter, 14 cm length) (Fig. 4.1). Before each MRS experiment, the $^{19}\text{F}/^1\text{H}$ coils were tuned to resonate at both the fluorine and hydrogen frequencies (120.1 and 127.7 MHz, respectively at 3T) on a network analyzer (National Instruments, Austin, TX, USA) at -30 dB signal loss or better.

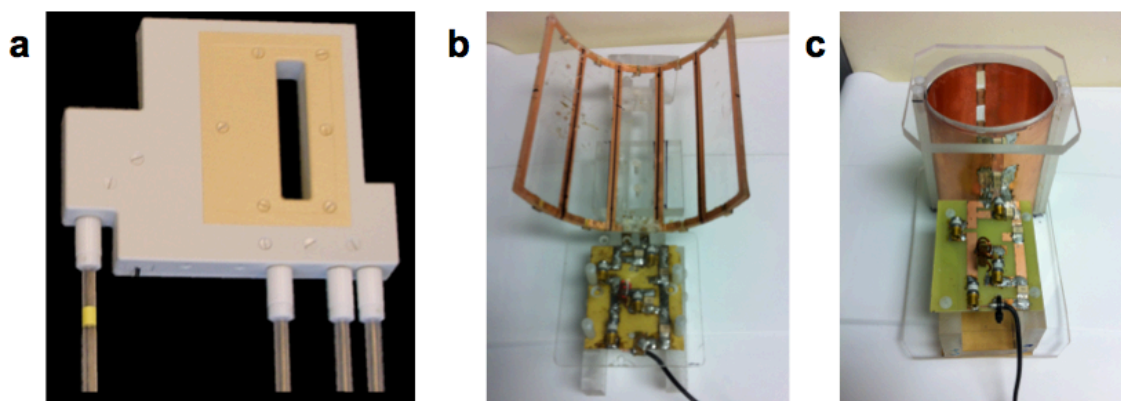


Figure 4.1 $^{19}\text{F}/^1\text{H}$ dual-tuned RF coils. (a) Single loop rectangular surface coil (7×12 cm, Philips Healthcare, Best, The Netherlands). (b) Custom-built 6-element semi-cylindrical coil (15 cm diameter), and (c) single-turn solenoid coil (11.5 cm diameter, 14 cm length). [Figure reprinted from Goette, et al. *In review*]

4.2.2 PFC NP Formulation and Phantom Setup

A nontargeted perfluoro-15-crown-5-ether (PFCE: $\text{C}_{10}\text{F}_{20}\text{O}_5$) NP emulsion was prepared as previously published (30), which was composed of 20% (v/v) PFCE (Exflour Research Corp., Round Rock, TX, USA), 2.0% (w/v) surfactant commixture, and 1.7% (w/v) glycerin, with water comprising the remaining balance. An MRS point source phantom was created by filling a 1 mL clear glass shell vial (6 mm inner diameter, National Scientific, Rockwood, TN, USA) with 50 mM PFCE NP emulsion in 2% agar (0.2 mL volume, 5 mm height in vial), with 2% agar comprising the rest of the volume. The phantom was positioned in a 1 L beaker filled with 275 mL 1.0% saline using a custom-built holder allowing translational movement in two directions (± 18 mm) at three different heights (9 mm, 15 mm, and 27 mm) above the surface and semi-cylindrical coils, and within the solenoid coil.

4.2.3 Power Setting Optimization and Flip Angle Calibration

Flip angle sweep experiments were performed on the ^{19}F and ^1H frequencies independently to determine optimal RF output settings for flip angle calibration. Slice-selective spectroscopic echo sampling was first performed on the ^{19}F signal as a single series, sweeping the flip angle setting from 10° to 210° in 10° -increments with the following parameters: 10 mm slice, 8 kHz excitation BW centered on single PFCE peak, TR/TE = 2000/2.6 ms, 4 NSA, scan time 4 min, automated power optimization preparation phase turned off. Peak power settings were adjusted according to the offset between real and requested 90° pulse, and the sequence was repeated in an iterative fashion until the optimal power setting was achieved, denoted by a maximum spectral height at the requested 90° pulse (Fig. 4.2a).

After acquiring a similar data set at this same power setting on the ^1H channel for comparison, the process was repeated at the ^1H frequency until an optimal power setting was achieved, which was then compared to the ^{19}F setting. This experiment was repeated in triplicate with the phantom located at 15 distinct locations for each coil, with replicates occurring on separate days after detuning and retuning the coils.

Optimized RF power settings for the ^{19}F and ^1H nuclei were depicted with a 3D ball plot in MATLAB (MathWorks, Natick, MA), with both spherical radius and color representing peak power (W) for each nucleus, averaged over each replicate. A ratio of $^{19}\text{F}/^1\text{H}$ peak power at each phantom location is also visualized with a ball plot, and a global average of $^{19}\text{F}/^1\text{H}$ peak power from all locations is reported for each RF coil, termed flip angle calibration ratio.

4.2.4 MRI Phantom Setup and B₁-Mapping Compensation

Two fluorine-containing phantoms were created to design and test a B₁-mapping compensation technique to correct for RF inhomogeneities in ¹⁹F MRI with ¹⁹F/¹H dual-tuned coils. A discrete sample phantom was made with two 5 mL glass vials (inner diameter 15 mm) filled with 1.0 M sodium fluoride (NaF) in 2% agar, aligned 2 cm apart in 200 mL bottle of 1.0% saline. A homogeneous ¹⁹F phantom consisted of a 300 mL glass bottle (inner diameter 6 cm) filled with 1.0 M NaF in 2% agar.

A simultaneous ¹⁹F/¹H 2D balanced FFE (bFFE) imaging sequence was used to generate transverse ¹⁹F and ¹H images of the phantoms, with identical parameters as follows: 140 mm FOV, matrix 64×64, 4 mm slice thickness, 2.18×2.18×4 mm resolution, exBW = 4 kHz centered on the single NaF peak, pBW = 500 Hz, α = 25°, TR/TE = 3.64/1.82 ms, NSA = 1000, 3.8 min scan time. The B₁ field was mapped using an actual flip angle imaging (AFI) sequence with the following parameters for both phantoms: 140 mm FOV, matrix 64×64, 13 4-mm slices, 2.18×2.18×4 mm resolution, α = 70°, TR/TE = 13.43/2.23 ms, 1.0 min scan time.

To correct for RF inhomogeneities present in the simultaneous ¹⁹F/¹H bFFE image acquisition, the sequence was modeled following rephased gradient echo theory as per Eq. 4.24 in Vlaardingerbroek et al. (31) as

$$M_T = M_0 \sin \alpha_{nom} \sqrt{E_2} \frac{1 - E_1}{1 - E_1 E_2 - (E_1 - E_2) \cos \alpha_{nom}}, \quad [4.1]$$

where α_{nom} is the nominal flip angle and $E_{1,2} = e^{-TR/T_{1,2}}$. From this signal model, a calibration factor (ρ) can be defined as

$$\rho = \sin(AFI * \alpha_{nom}) \frac{1 - E_1}{1 - E_1 E_2 - (E_1 - E_2) \cos(AFI * \alpha_{nom})}, \quad [4.2]$$

where AFI represents the voxel values from the B_1 map ($\alpha_{\text{requested}}/\alpha_{\text{nominal}}$). A spatially dependent calibration mask was calculated from Eq. 4.2 in MATLAB and used to compensate the ^1H and ^{19}F signal intensities of the bFFE molecular imaging sequence by dividing each image by ρ , on a voxel-by-voxel basis.

4.2.5 *In Vivo* ^{19}F MRI Experiment

An in vivo ^{19}F MR imaging study was performed at 3T with the $^{19}\text{F}/^1\text{H}$ dual-tuned single loop surface coil previously mentioned (7×12 cm). In accordance with institution-approved protocols, New Zealand White Rabbits (2 kg) (n = 3) were implanted with a VX2 adenocarcinoma tumor (2-3 cm) in the hind leg (30), and allowed to grow for two weeks prior to imaging to achieve a tumor size ~ 15 mm. An $\alpha_v\beta_3$ -integrin-targeted PFCE NP emulsion (20 vol%) was injected intravenously and allowed to circulate 3 hours before imaging. To avoid signal contamination from inhaled fluorinated anesthesia, a ketamine (85 mg/kg) / xylazine (10mg/kg) i.m. injection was used for anesthesia induction, which was maintained with a ketamine i.v. infusion (18 mg/kg/hr).

A simultaneous $^{19}\text{F}/^1\text{H}$ balanced UTE-SSFP imaging sequence with Wong-type 3D radial readout trajectory (32) was used with the following parameters: 140 mm FOV, matrix 96^3 , isotropic voxel $\Delta x = 1.46$ mm, $\text{exBW} = 4$ kHz centered on the PFCE peak, $\text{pBW} = 400$ Hz, $\alpha = 30^\circ$, $\text{TR/TE} = 2.32/0.13$ ms, $\text{NSA} = 56$, 35 min scan time. For this in vivo experiment, the radial k-space data were reconstructed at full resolution for the ^1H component and a lower resolution with higher signal-to-noise for the ^{19}F component. The latter was achieved by applying flat k-space weighting to the data outside a radius corresponding to 23% of the fully sampled sphere in k-space (23% of the Nyquist radius) and using the usual quadratic weighting for the center of k-

space (33,34). After anatomical colocalization of ^{19}F signal was confirmed with the simultaneously acquired ^1H image, a high-resolution gradient echo ^1H image was used to display the overlaid ^{19}F signal with the following parameters: FOV = 128×128 mm, matrix = 256×256, slice thickness = 4 mm, voxel size = 0.5×0.5×4 mm, $\alpha = 35^\circ$, TR/TE = 25.16/7.02 ms, 23 NSA, and a scanning time of 2.5 minutes.

The B_1 field was mapped with an AFI sequence with the following parameters: 140 mm FOV, 96×96 matrix, 15 1.46-mm slices, 1.46×1.46×1.46 mm resolution, $\alpha = 70^\circ$, TR/TE = 16.0/2.93 ms, 1.9 min scan time. Because balanced UTE-SSFP follows the same balanced gradient echo theory as the bFFE sequence in the phantom experiment, a spatially dependent calibration mask (ρ) was calculated from Eq. 4.2 in MATLAB and used to compensate the ^1H and ^{19}F signal intensities on a voxel-by-voxel basis. Importantly, the same correction scheme was performed on the imaging slice that contained the fluorine standard (150 mM $_{^{19}\text{F}}$ PFCE NP in agar) to which the in vivo bound PFC NP ^{19}F signal was compared for quantification.

4.2.6 Statistical Analysis

MR spectroscopy and imaging data were analyzed with analysis of variance (ANOVA) or student t-tests as appropriate with MATLAB. For all statistical tests, $p < 0.05$ denotes statistical significance. Standard errors of the mean are reported for MRS and MRI measurements, and used to display error bars. Measures of ^{19}F image homogeneity were calculated as a root-mean-square value over all ^{19}F signal-containing voxels.

4.3 Results

4.3.1 Power Setting Optimization and Flip Angle Calibration

Power settings were optimized for ^{19}F and ^1H nuclei, such that a requested 90° flip angle yielded a maximum spectral height in FA sweep measurements of a PFC NP point source phantom. Figure 4.2 shows a representative FA sweep that was optimized for ^{19}F (top), and the resultant ^1H FA sweep (bottom) using the same power setting (peak power = 122.9 W), which obviously was too high for ^1H , yielding a maximum ^1H spectral height at 20° .

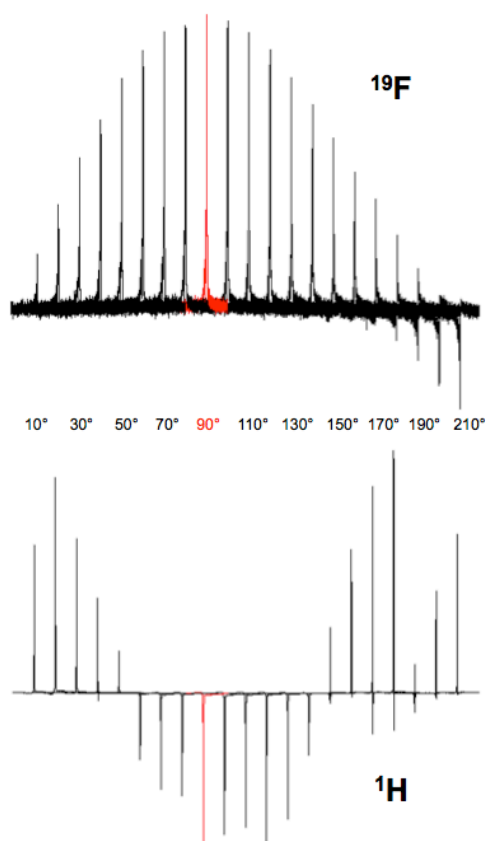


Figure 4.2 Representative flip angle sweep (10° - 210°) on ^{19}F nucleus (**top**) and ^1H nucleus (**bottom**) using the same power setting (peak power = 122.9 W) with a $^{19}\text{F}/^1\text{H}$ dual-tuned surface coil indicating correct power settings for ^{19}F , but too high for ^1H . [Figure reprinted from Goette, et al. *In review*]

Power settings for ^{19}F and ^1H nuclei are depicted in a 3D ball plot (Fig. 4.3), in which the spherical radius and color correspond to the requested peak power (W) for a point source PFCE

NP phantom at 15 distinct locations in the FOV of the surface coil, averaged over three replicates. These plots exemplify the need for higher power settings to accurately measure sources farther away from a surface coil, as well as the obvious difference in optimal power settings between ^{19}F and ^1H nuclei. However, a ratio of optimum $^{19}\text{F}/^1\text{H}$ power requirements yields a spatially independent calibration value for the surface coil (1.48 ± 0.06).

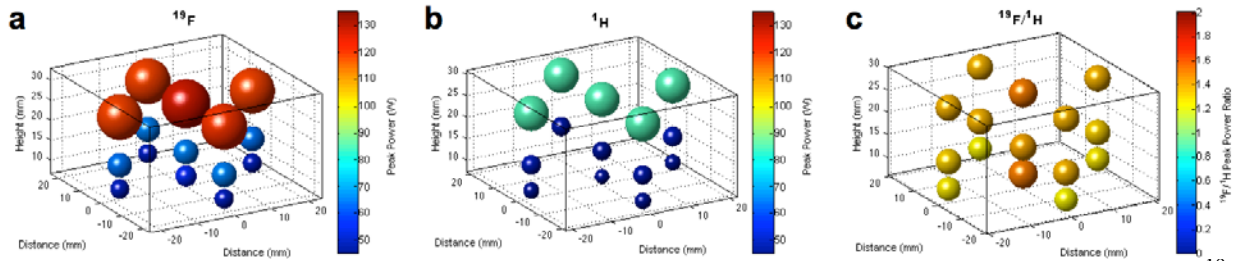


Figure 4.3 3D Ball plot representation of optimized RF power settings (peak power, W) for ^{19}F (a) and ^1H (b) nuclei using a $^{19}\text{F}/^1\text{H}$ dual-tuned surface coil and a point source phantom of PFCE NP emulsion. (c) Ratio of optimum $^{19}\text{F}/^1\text{H}$ power setting yields a spatially independent calibration value (1.48 ± 0.06 for surface coil). [Figure reprinted from Goette, et al. *In review*]

Figure 4.4 displays the MRS phantom data for all three $^{19}\text{F}/^1\text{H}$ dual-tuned coils, with averaged measurements from all five locations at each height (9, 15, 27 mm). Optimized ^{19}F peak power was significantly different than was the ^1H power requirement at each height for each coil ($p < 0.05$ in all cases). Taking a ratio of $^{19}\text{F}/^1\text{H}$ power settings for the semi-cylindrical coil yielded a calibration value of 1.71 ± 0.02 , and 1.92 ± 0.03 for the single-turn solenoid coil.

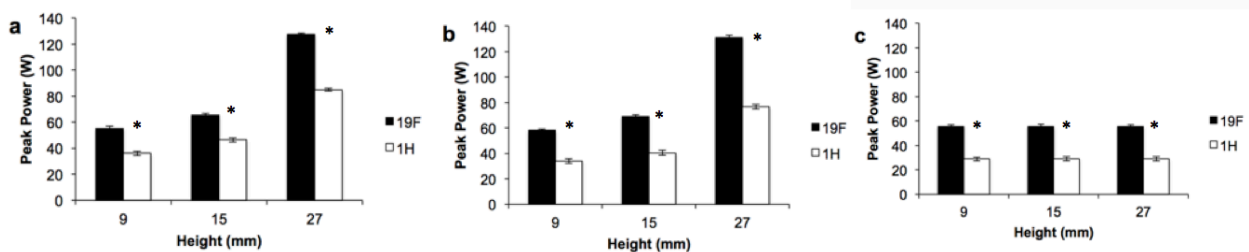


Figure 4.4 Power settings (peak power, W) needed to optimize 90° flip angle for ^{19}F and ^1H signals from point source phantom at 9 mm, 15 mm, and 27 mm above $^{19}\text{F}/^1\text{H}$ dual-tuned surface coil (a), semi-cylindrical coil (b), and within single-turn solenoid coil (c). [Figure reprinted from Goette, et al. *In review*]

4.3.2 B₁-Mapping Compensation in Phantom Experiments

Figure 4.5 demonstrates a technique for B₁-mapping compensation of ¹⁹F MRI using the ¹H signal in a phantom containing two vials of 1.0 M NaF in agar, imaged with a simultaneous ¹⁹F/¹H bFFE sequence and a ¹⁹F/¹H dual-tuned surface coil. Before correction, the ¹⁹F image (Fig. 4.5a) and ¹⁹F/¹H overlay image (Fig. 4.5b) exhibit the effects of the inhomogeneous RF field produced by the surface coil. Mean signal intensity in the vial closest to the coil was 2537 ± 176 arbitrary units (a.u.), while the ¹⁹F signal from the identical vial 2 cm further from the coil was 66.0% lower (863 ± 40 , $p < 0.001$). The B₁-field was mapped using the ¹H signal with actual flip angle imaging (% actual/requested FA) (Fig. 5c), and input into Eq. 4.2 to create a correction ratio (Fig. 4.5d). This factor was used to correct both ¹⁹F and ¹H signal intensities, as displayed in Figure 5e&f. After correction, the mean signal intensity in the vial closest to the coil (2621 ± 156 a.u.) was not significantly different ($p = 0.85$) than that in the vial farther from the coil (2681 ± 129 a.u.).

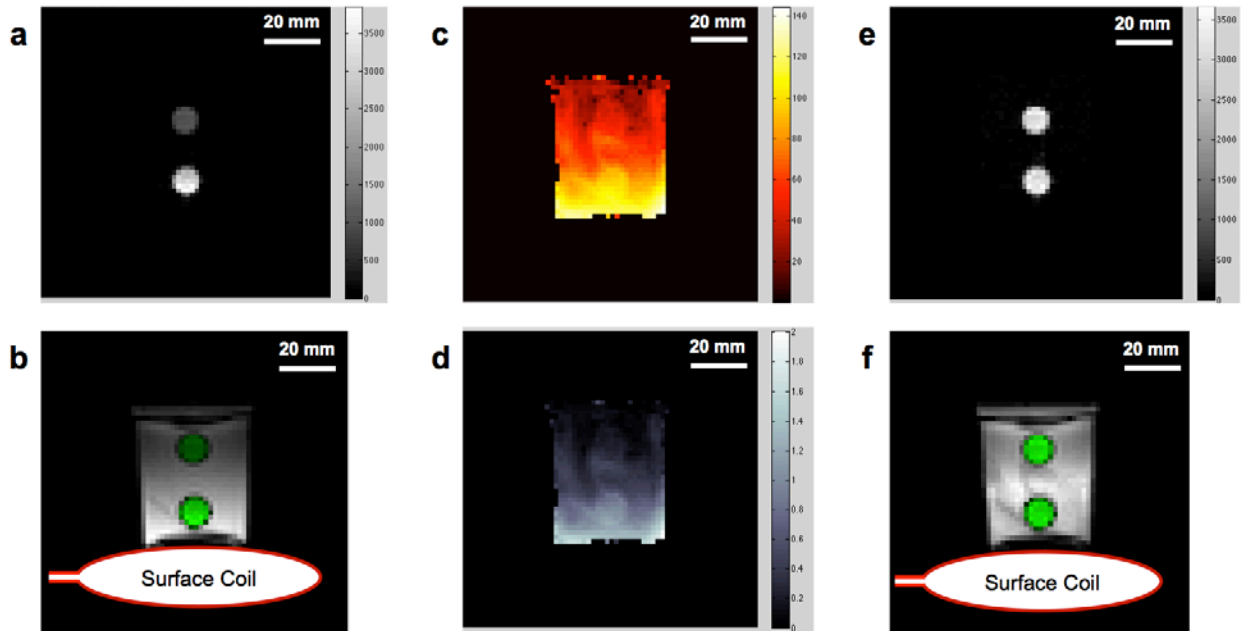


Figure 4.5 ¹⁹F MRI of phantom with two vials of 1.0 M NaF in agar using a simultaneous ¹⁹F/¹H bFFE sequence and a ¹⁹F/¹H dual-tuned surface coil. Before correction, ¹⁹F image (a) and ¹⁹F/¹H overlay image (b) illustrate the inhomogeneous RF field produced by the surface coil, resulting

in a mean signal intensity of 2537 ± 31 a.u. and 863 ± 7 a.u. in each vial. ^1H B_1 -field was mapped with actual flip angle imaging (% actual/requested FA) (c), and input into bFFE signal model to create a correction factor (d), which was used to compensate ^{19}F and ^1H signal intensities. The corrected ^{19}F image (e) and $^{19}\text{F}/^1\text{H}$ overlay image (f) demonstrate the image-based compensation technique, resulting in a mean signal intensity of 2621 ± 27 a.u. and 2681 ± 23 a.u. in each vial. [Figure reprinted from Goette, et al. *In review*]

Figure 4.6 shows the results of the one-way ANOVA analysis of the phantom before and after correction.

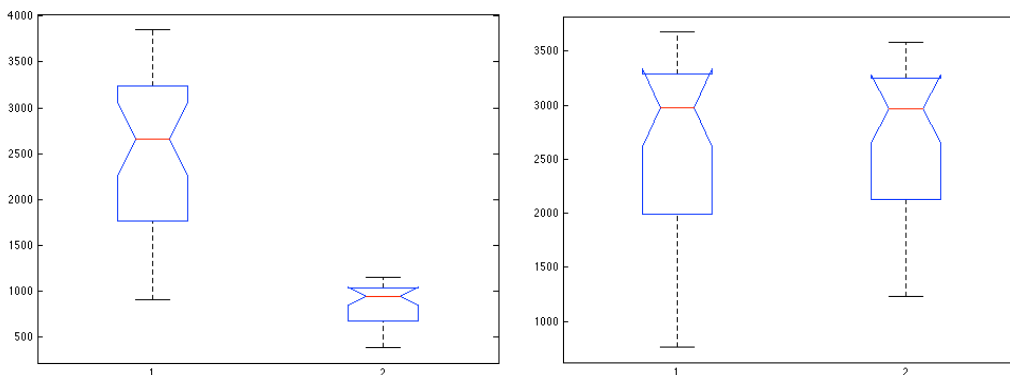


Figure 4.6 One-way ANOVA analysis of the ^{19}F signal intensity from phantom of two PFC NP vials (1: closer to coil; 2: farther away) before (left) and after (right) B_1 -mapping compensation.

Figure 4.7 shows the B_1 -field compensation applied to a homogeneous phantom of 1.0 M NaF in 2% agar. Before correction, the ^{19}F (Fig. 4.7a) and $^{19}\text{F}/^1\text{H}$ overlay images (Fig. 4.7b) display the inhomogeneity of the surface coil, with a mean signal intensity of 1145 ± 35 and a RMS value of 1320. B_1 -mapping compensation with AFI and calculated correction ratio (Fig. 4.7c&d), yielded a more homogeneous corrected ^{19}F image (Fig. 4.7e), as measured by a mean signal intensity of 2332 ± 29 and a RMS value of 1157.

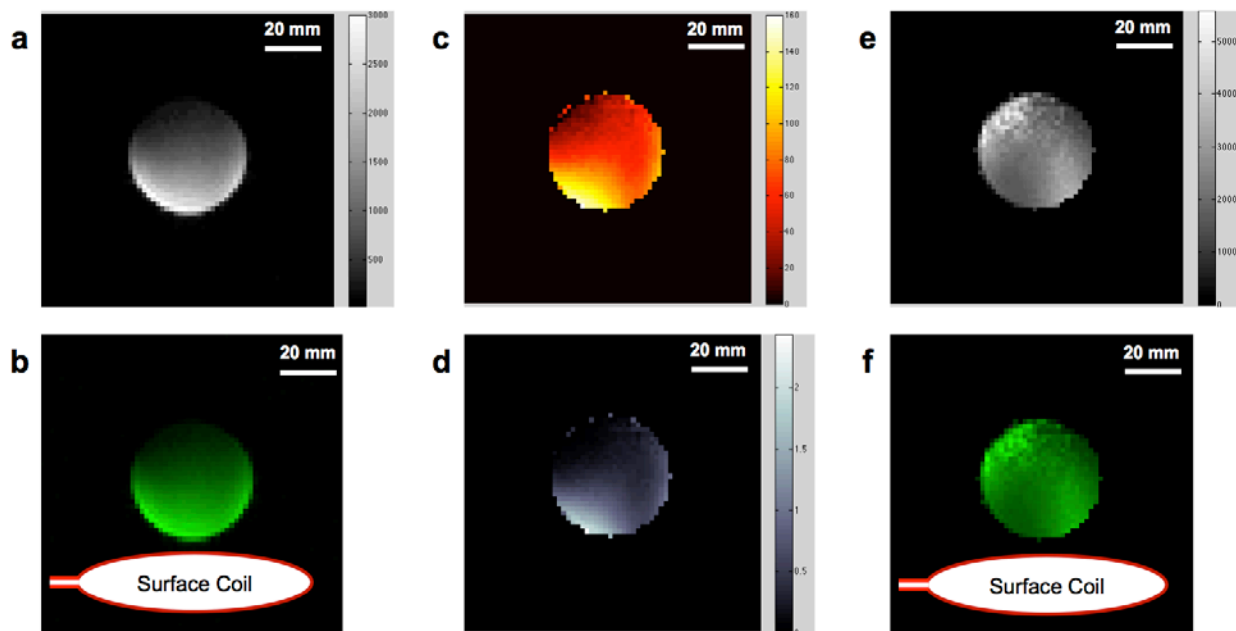


Figure 4.7 ^{19}F MRI of a homogeneous phantom (1.0 M NaF in 2% agar) imaged with a simultaneous $^{19}\text{F}/^1\text{H}$ bFFE sequence and a $^{19}\text{F}/^1\text{H}$ dual-tuned surface coil. Before correction, the ^{19}F image (a) and $^{19}\text{F}/^1\text{H}$ overlay image (b) illustrate the inhomogeneous RF field produced by the surface coil. ^1H B_1 -field was mapped with actual flip angle imaging (% actual/requested FA) (c), and input into bFFE signal model to create correction ratio (d), which was used to correct ^{19}F and ^1H signal intensities. The corrected ^{19}F image (e) and $^{19}\text{F}/^1\text{H}$ overlay image (f) demonstrate the image-based compensation technique. [Figure reprinted from Goette, et al. *In review*]

4.3.3 *In Vivo* ^{19}F MRI Experiment

PFC NP targeted to the tumor neovasculature provided a highly localized ^{19}F signal as expected (Fig. 4.8, tumor enhancement circled in red). In the uncorrected ^{19}F image superimposed on a high-resolution ^1H image of the rabbit anatomy (Fig. 4.8a), the concentration of PFC NP localized to the tumor was measured at $20.0 \pm 0.12 \text{ mM}_{^{19}\text{F}}$, when compared to an external standard ($150 \text{ mM}_{^{19}\text{F}}$). By using the AFI B_1 -field map and calibration mask (Fig. 4.8b&c) to compensate the ^{19}F image for inhomogeneities introduced by the RF surface coil, local targeted PFC NP was calculated at $25.5 \pm 0.10 \text{ mM}_{^{19}\text{F}}$, or a 27.5% increase ($p < 0.05$).

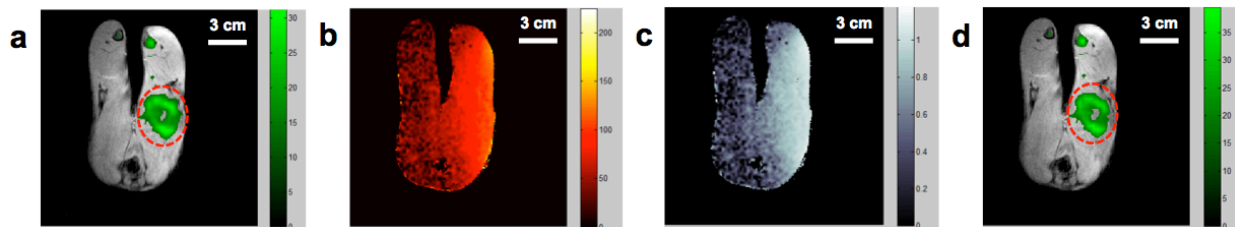


Figure 4.8 B₁-mapping compensation of in vivo cancer model in rabbit with the use of $\alpha_v\beta_3$ -integrin-targeted PFC NP nanoparticles captured by ^{19}F MRI with a $^{19}\text{F}/^1\text{H}$ dual-tuned surface coil (located at image right). In the uncorrected ^{19}F image overlaid on the high-resolution ^1H image (a), PFC NP concentration was quantified as $20.0 \pm 0.12 \text{ mM}_{^{19}\text{F}}$, compared to an external standard of known concentration ($150 \text{ mM}_{^{19}\text{F}}$). Illustrated are: B₁-field mapping with AFI (% actual/requested FA) (b) and calibration mask calculated from a balanced UTE-SSFP signal model (c). In the corrected ^{19}F image overlaid on the high-resolution ^1H image, PFC NP concentration was quantified as $25.5 \pm 0.10 \text{ mM}_{^{19}\text{F}}$. [Figure reprinted from Goette, et al. *In review*]

4.4 Discussion

This study describes a strategy to more accurately quantify sparse ^{19}F MR signals from targeted perfluorocarbon nanoparticle emulsions by means of ^{19}F flip angle calibration that utilizes the abundant ^1H signal, and a ^1H image-based B₁-mapping correction to the ^{19}F and ^1H images. The requisite peak power to achieve a requested flip angle for ^{19}F and ^1H nuclei was shown to be different for three $^{19}\text{F}/^1\text{H}$ dual-tuned RF coils. However, a ratio of the two optimized power settings results in a spatially independent calibration ratio that was unique to each coil. Once established, the coil-dependent calibration ratio can be used to set the power settings for ^{19}F imaging based on the ^1H signal for all imaging with the coil, regardless of location within the field of view. For sparse fluorine signals as would be expected in clinical MR molecular imaging, power settings and calibrations cannot be performed easily on the ^{19}F nuclei a priori. However, ^{19}F flip angle calibration can be performed based on the rich ^1H signal by multiplying the ^1H -derived power settings by the calibration ratio before any ^{19}F contrast agent is even introduced.

This work also demonstrated the utility of an image-based B_1 -mapping compensation to correct signal intensities for simultaneously acquired ^1H and ^{19}F images. The deleterious effects of coil inhomogeneities on quantitative ^{19}F MRI were demonstrated in a phantom experiment where two significantly different signal intensities were demonstrated for identical fluorine samples with the use of a $^{19}\text{F}/^1\text{H}$ dual-tuned surface coil. However, the proposed B_1 -mapping compensation technique corrected the signal intensity for both the ^{19}F and ^1H images, thereby removing the effects of the inhomogeneous RF field. This method was further tested in a homogeneous fluorine phantom, which corrected for the characteristic signal drop-off observed with surface coils, as a consequence of employing the proposed B_1 correction technique to improve ^{19}F image homogeneity. Finally, the preclinical utility of this correction technique was tested with an in vivo cancer model of the B_1 compensation technique that apparently improved the measurement accuracy of bound $\alpha_v\beta_3$ -integrin-targeted PFC NP with ^{19}F imaging. Unfortunately, independent direct comparison of ^{19}F signals to tissue levels of PFC NP is technically complex due to extraction difficulties and PFC volatility, but given the clear benefit of the compensations in phantoms, we propose that the derived answers will be more satisfactory following correction.

This study was performed with $^{19}\text{F}/^1\text{H}$ dual-tuned coils, which consist of the same coil elements, and hence generate the same B_1 field for both ^{19}F and ^1H nuclei (29). The observed difference in requisite power settings between the two nuclei demonstrates the effective difference in detection sensitivity of these dual-resonant coils, because they are electrically tuned in the same manner for both nuclei. However, this difference is consistent for each coil, and allows for the determination of a specific coil-dependent calibration ratio. Notably, this property is likely unique to dual-resonant coils, which cannot be replicated with single-tuned coils or

other double-frequency coils with significantly different geometry between ^{19}F and ^1H resonator elements. On the other hand, although the B_1 correction technique using ^1H -derived B_1 maps to correct ^{19}F and ^1H images also benefits from the use of dual-tuned RF coils, this technique should apply to single-tuned coils if the B_1 fields for the two nuclei are the same. In the future, additional testing with both dual-tuned and single-tuned coils would be valuable to determine translatability of this technique to such coils.

4.5 Conclusion

In conclusion, this study devised and tested a new approach to overcome certain challenges for accurate *in vivo* quantitative ^{19}F MR molecular imaging, which comprises a combination of flip angle calibration between ^1H and ^{19}F nuclei, and B_1 -mapping compensation to offset RF inhomogeneities. Correction techniques such as this one should facilitate improved accuracy and repeatability of measurements of non-proton molecular imaging agents used in preclinical and clinical trials at routine field strengths.

4.6 Acknowledgements

I would like to thank the co-authors of the following manuscript: Goette MJ, Lanza GM, Caruthers SD, Wickline SA. New Approaches for *In Vivo* Quantitative ^{19}F MR Molecular Imaging using Flip Angle Calibration and B_1 -Mapping Compensation. *J Magn Reson Imaging*. *In review*. My role in the work was to design the power setting optimization and flip angle calibration technique, develop the B_1 -correction method, test the technique with the phantom and *in vivo* rabbit model of cancer, assemble all data and figures, and write the manuscript. I would also like to thank Todd A. Williams and John S. Allen for their help with the animal model and

imaging, Frank D. Hockett for his help designing and constructing the custom-built RF coils, Angana Senpan for her help preparing the PFC NP emulsion, and Jochen Keupp for his insightful discussions on fluorine MR.

4.7 References

1. Weissleder R, Mahmood U. Molecular imaging. *Radiology* 2001;219(2):316-333.
2. Wickline SA, Lanza GM. Nanotechnology for molecular imaging and targeted therapy. *Circulation* 2003;107(8):1092-1095.
3. Wickline SA, Neubauer AM, Winter PM, Caruthers SD, Lanza GM. Molecular imaging and therapy of atherosclerosis with targeted nanoparticles. *J Magn Reson Imaging* 2007;25(4):667-680.
4. Wickline SA, Mason RP, Caruthers SD, Chen J, Winter PM, Hughes MS, Lanza GM. Fluorocarbon agents for quantitative multimodal molecular imaging and targeted therapeutics. In: Weissleder R, Ross BD, Rehemtulla A, Gambhir SS, editors. *Molecular Imaging: Principles and Practice*. Shelton, CT: Peoples Medical Publishing House-USA; 2010. p 542-573.
5. Mikawa M, Kato H, Okumura M, Narazaki M, Kanazawa Y, Miwa N, Shinohara H. Paramagnetic water-soluble metallofullerenes having the highest relaxivity for MRI contrast agents. *Bioconjugate Chem* 2001;12(4):510-514.
6. Lanza GM, Lorenz CH, Fischer SE, Scott MJ, Cacheris WP, Kaufmann RJ, Gaffney PJ, Wickline SA. Enhanced detection of thrombi with a novel fibrin-targeted magnetic resonance imaging agent. *Acad Radiol* 1998;5 Suppl 1:S173-176; discussion S183-184.

7. Flacke S, Fischer S, Scott MJ, Fuhrhop RJ, Allen JS, McLean M, Winter P, Sicard GA, Gaffney PJ, Wickline SA, Lanza GM. Novel MRI contrast agent for molecular imaging of fibrin: implications for detecting vulnerable plaques. *Circulation* 2001;104(11):1280-1285.
8. Lanza GM, Winter PM, Caruthers SD, Morawski AM, Schmieder AH, Crowder KC, Wickline SA. Magnetic resonance molecular imaging with nanoparticles. *J Nucl Cardiol* 2004;11(6):733-743.
9. Neubauer AM, Winter P, Caruthers S, Lanza G, Wickline SA. Magnetic resonance molecular imaging and targeted therapeutics. In: Kwong RY, editor. *Contemporary Cardiology: Cardiovascular magnetic resonance imaging*. Totowa, NJ: Humana Press; 2007. p 639-662.
10. Morawski AM, Winter PM, Crowder KC, Caruthers SD, Fuhrhop RW, Scott MJ, Robertson JD, Abendschein DR, Lanza GM, Wickline SA. Targeted nanoparticles for quantitative imaging of sparse molecular epitopes with MRI. *Magn Reson Med* 2004;51(3):480-486.
11. Bulte JW, Kraitchman DL. Iron oxide MR contrast agents for molecular and cellular imaging. *NMR Biomed* 2004;17(7):484-499.
12. Sadowski EA, Bennett LK, Chan MR, Wentland AL, Garrett AL, Garrett RW, Djamali A. Nephrogenic systemic fibrosis: risk factors and incidence estimation. *Radiology* 2007;243(1):148-157.
13. Boyd AS, Zic JA, Abraham JL. Gadolinium deposition in nephrogenic fibrosing dermopathy. *J Am Acad Dermatol* 2007;56(1):27-30.

14. Winter PM, Morawski AM, Caruthers SD, Fuhrhop RW, Zhang H, Williams TA, Allen JS, Lacy EK, Robertson JD, Lanza GM, Wickline SA. Molecular imaging of angiogenesis in early-stage atherosclerosis with $\alpha v\beta 3$ -integrin-targeted nanoparticles. *Circulation* 2003;108(18):2270-2274.
15. Schmieder AH, Caruthers SD, Zhang H, Williams TA, Robertson JD, Wickline SA, Lanza GM. Three-dimensional MR mapping of angiogenesis with $\alpha 5\beta 1(\alpha v\beta 3)$ -targeted theranostic nanoparticles in the MDA-MB-435 xenograft mouse model. *FASEB J* 2008;22(12):4179-4189.
16. Mason RP, Antich PP, Babcock EE, Gerberich JL, Nunnally RL. Perfluorocarbon imaging in vivo: a ^{19}F MRI study in tumor-bearing mice. *Magn Reson Imaging* 1989;7(5):475-485.
17. Morawski AM, Winter PM, Yu X, Fuhrhop RW, Scott MJ, Hockett F, Robertson JD, Gaffney PJ, Lanza GM, Wickline SA. Quantitative "magnetic resonance immunohistochemistry" with ligand-targeted ^{19}F nanoparticles. *Magn Reson Med* 2004;52(6):1255-1262.
18. Chen JJ, Lanza GM, Wickline SA. Quantitative magnetic resonance fluorine imaging: today and tomorrow. *Wiley Interdiscip Rev Nanomed Nanobiotechnol* 2010;2(4):431-440.
19. Reid DG, Murphy PS. Fluorine magnetic resonance in vivo: a powerful tool in the study of drug distribution and metabolism. *Drug Discov Today* 2008;13(11-12):473-480.
20. Foster MA. *Magnetic resonance in medicine and biology*. New York, NY: Pergamon Press; 1984. 244 p.

21. Keupp J, Rahmer J, Grässlin I, Mazurkewitz PC, Schaeffter T, Lanza GM, Wickline SA, Caruthers SD. Simultaneous dual-nuclei imaging for motion corrected detection and quantification of ^{19}F imaging agents. *Magn Reson Med* 2011;66(4):1116-1122.
22. Rahmer J, Bornert P, Groen J, Bos C. Three-dimensional radial ultrashort echo-time imaging with T2 adapted sampling. *Magn Reson Med* 2006;55(5):1075-1082.
23. Caruthers SD, Winter PM, Wickline SA, Lanza GM, Keupp J. MR molecular imaging of angiogenesis using targeted perfluorocarbon nanoparticles. *MedicaMundi* 2010;54(2):5-13.
24. Ahrens ET, Zhong J. In vivo MRI cell tracking using perfluorocarbon probes and fluorine-19 detection. *NMR Biomed* 2013;26(7):860-871.
25. Barnett BP, Ruiz-Cabello J, Hota P, Ouwerkerk R, Shablott MJ, Lauzon C, Walczak P, Gilson WD, Chacko VP, Kraitchman DL, Arepally A, Bulte JW. Use of perfluorocarbon nanoparticles for non-invasive multimodal cell tracking of human pancreatic islets. *Contrast Media Mol Imaging* 2011;6(4):251-259.
26. Hu L, Hockett FD, Chen J, Zhang L, Caruthers SD, Lanza GM, Wickline SA. A generalized strategy for designing $^{19}\text{F}/^1\text{H}$ dual-frequency MRI coil for small animal imaging at 4.7 Tesla. *J Magn Reson Imaging* 2011;34(1):245-252.
27. Keupp J, Mazurkewitz PC. Simultaneous $^{19}\text{F}/^1\text{H}$ imaging for Quantification : Calibration and Sensitivity Assessment. In *Proceedings of the Annual Meeting of ISMRM, 2007*. p. 1334.
28. Sung K, Daniel BL, Hargreaves BA. Transmit B_1^+ field inhomogeneity and T1 estimation errors in breast DCE-MRI at 3 tesla. *J Magn Reson Imaging* 2013;38(2):454-459.

29. Hockett FD, Wallace KD, Schmieder AH, Caruthers SD, Pham CTN, Wickline SA, Lanza GM. Simultaneous dual frequency 1H and 19F open coil imaging of arthritic rabbit knee at 3T. *IEEE T Med Imaging* 2011;30(1):22-27.
30. Hu G, Lijowski M, Zhang H, Partlow KC, Caruthers SD, Kiefer G, Gulyas G, Athey P, Scott MJ, Wickline SA, Lanza GM. Imaging of Vx-2 rabbit tumors with $\alpha\text{v}\beta\text{3}$ - integrin-targeted ^{111}In nanoparticles. *Int J Cancer* 2007;120(9):1951-1957.
31. Vlaardingerbroek MT, Boer JAd. *Magnetic resonance imaging : theory and practice*. New York, NY: Springer; 2003. 499 p.
32. Wong STS, Roos MS. A strategy for sampling on a sphere applied to 3D selective RF pulse design. *Magn Reson Med* 1994;32(6):778-784.
33. Glover GH, Pauly JM, Bradshaw KM. Boron-11 imaging with a three-dimensional reconstruction method. *J Magn Reson Imaging* 1992;2(1):47-52.
34. Rahmer J, Keupp J, Caruthers SD, Lips O, Williams TA, Wickline SA, Lanza GM. Dual resolution simultaneous 19F/1H in vivo imaging of targeted nanoparticles. In *Proceedings of the 17th Annual Meeting of ISMRM, Honolulu, Hawaii, USA, 2009*. p. 612.

Chapter 5. Novel *In Vivo* Applications of ¹⁹F MR Molecular Imaging at 3T

The third aim of this thesis was to evaluate the potential for clinical translation with *ex vivo* and *in vivo* preclinical experiments. To successfully translate the techniques presented in this work, and the work of many other molecular imaging scientists, into the clinic to help diagnose and treat diseases in humans, there must be thorough testing and validation with controlled animal experiments. In addition to the oncological applications of improved ¹⁹F MR molecular imaging of $\alpha_v\beta_3$ -integrin-targeted PFC NPs presented in Chapter 4, two more potentially translatable applications are presented here: renal perfusion imaging and atherosclerotic plaque imaging. Importantly, translation of both of these applications to humans requires their implementation at clinical field strengths, so a clinical 3T MR scanner is used instead of a small animal scanner at a higher field strength.

5.1 Imaging Renal Perfusion in Acute Kidney Injury at 3T

5.1.1 Introduction

Acute kidney injury (AKI) affects a significant portion of hospitalized patients in the United States and has an attendant mortality of up to 76.8% (1). AKI is characterized by reduced renal blood flow and abnormal intrarenal oxygenation as a consequence of inflammatory signaling molecules that affect tubular function and renal microcirculation (2). Noninvasive imaging of intrarenal perfusion in AKI patients could be useful for diagnosing the extent of damage, as well as monitoring response to therapy. However, in many cases the use of contrast agents is restricted due to associated renal toxicity (3), and no specific agents have been approved to target the well-defined molecular mechanisms involved in AKI (4).

While arterial spin labeling (ASL) has been reported as a noninvasive technique to measure renal perfusion in AKI (5), there are challenges to accurate perfusion quantification such as variations in blood T_1 (6), which is often present in AKI subjects with abnormal intrarenal oxygenation. Recently, perfluorocarbon (PFC) nanoparticle (NP) emulsions have been evaluated as a promising nontoxic agent for MR molecular imaging of renal damage and perfusion on an 11.7T Varian small animal MR scanner (7). Furthermore, ^{19}F MR using a $^{19}\text{F}/^1\text{H}$ dual-tuned RF coil has been utilized to directly image and quantify the fluorinated core of PFC NP emulsions at clinical field strengths (8), where the signal is directly proportional to local blood volume. In this study, we investigated the imaging of renal perfusion using simultaneous $^{19}\text{F}/^1\text{H}$ MRI of PFC NPs in an ischemia/reperfusion rat model of AKI at 3T.

5.1.2 Methods

All protocols, including animal handling, surgery, and treatment, as well as MRI procedures were approved by the Animal Studies Committee of Washington University in St. Louis. Under anesthesia with ketamine (85 mg/kg) and xylazine (13 mg/kg), adult male Sprague Dawley rats ($n = 6$) (Harlan Laboratories, USA) underwent a surgical procedure to induce unilateral warm ischemia, followed by reperfusion. Following a laparotomy to expose the vasculature of the left kidney, the left renal artery was ligated and either permanently occluded ($n = 2$) or occluded for 45 min followed by reperfusion ($n = 2$). Age-matched normal rats were included as controls ($n = 2$). Animal body temperature was maintained at 37°C using a small animal heating system. The surgical wound was then closed in layers, after which the animal recovered and was returned to its cage. Following recovery for 24 hr, the injured kidney and

contralateral control kidney were imaged either *in vivo* or excised, fixed in 10% formalin, and imaged *ex vivo*.

A nontargeted perfluoro-15-crown-5-ether (PFCE: C₁₀F₂₀O₅) nanoparticle emulsion (20 vol%) was prepared as previously published (9), and injected i.v. into the tail vein (3 ml/kg) 5 min before imaging or excision. MR data were acquired on a 3T clinical whole-body scanner (Achieva, Philips Healthcare, Best, The Netherlands) with a dual ¹⁹F/¹H spectrometer system and a dual-tuned transmit/receive solenoid RF coil (7 cm diameter for *in vivo*; 4 cm diameter for *ex vivo*). Following ¹⁹F/¹H flip angle calibration (as seen in Chapter 4), a simultaneous 2D ¹⁹F/¹H balanced FFE (bFFE) imaging sequence was used with the following parameters: 140 mm FOV (cross-sectional images: 64 mm FOV), matrix 64×64, 3 mm slice thickness, exBW = 4 kHz centered on the single PFCE peak, pBW = 500 Hz, $\alpha = 25^\circ$, TR/TE = 4.198/2.10 ms, NSA = 500, 5 min scan time. The low-resolution ¹H images (not shown) were used to confirm kidney visualization and anatomical coregistration. For display, higher-resolution ¹H images were acquired with a 2D TSE sequence and similar geometry: 140 mm FOV (cross-sectional image: 64 mm FOV), matrix 256×256, 3 mm slice thickness, TR/TE = 500/27.8 ms, NSA = 4, 2 min scan time. The B₁ field was mapped (on ¹H) using an actual flip angle imaging (AFI) sequence with geometry matching the cross-sectional images: 64 mm FOV, matrix 64×64, 7 3-mm slices, 1×1×3 mm resolution, $\alpha = 70^\circ$, 40 s scan time. Renal perfusion in the cortex and medulla was measured in the injured kidney by quantification of local PFC NP concentration via comparison to an external standard of known PFCE concentration (comprising 150 mM_{19F} PFCE NP in 2% agar).

5.1.3 Results

Figure 5.1 demonstrates the feasibility to image renal perfusion *in vivo* with ^{19}F MRI at 3T. Fig. 5.1a shows the anatomical ^1H image along the long-axis of the permanently occluded left kidney and the normally perfused right kidney. Functional ^{19}F image (Fig. 5.1b) shows the blood pool PFCE signal in the same animal with kidney locations outlined in red (arrow: injured left kidney). The coregistered ^1H (gray scale, Fig. 5.1c) and ^{19}F (color coded in green) image shows no PFCE signal, reflecting no perfusion to the occluded left kidney, but normal perfusion to the right kidney. Additional ^{19}F signal is observed in the vasculature as well as the liver and spleen, which are included in the mechanism by which the PFCE particles are cleared.

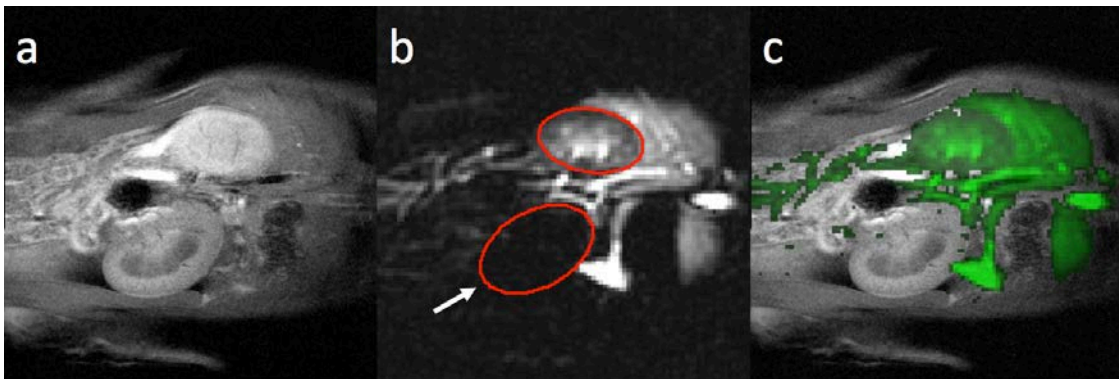


Figure 5.1 (a) ^1H TSE image of unilateral permanent occlusion of renal artery in rat left kidney. (b) ^{19}F bFFE image of PFCE NP emulsion injected i.v. (3 ml/kg). Location of kidneys outlined in red (arrow: injured left kidney). (c) ^{19}F image false-colored in green overlaid on ^1H image.

Figure 5.2 demonstrates the capability of ^{19}F MRI to distinguish cortical (C) from medullary (M) renal perfusion, labeled in (Fig. 5.2a), *in vivo* at 3T (b-g). Compared to a normal control rat (b&c), the permanently occluded left kidney (d) shows no discernable signal, and the 45-min injured kidney shows lower medullary signal (f) than its contralateral control (g). The *in vivo* AKI imaging is supported by *ex vivo* imaging that qualitatively shows lower medullary signal in the injured kidney (h) as compared to its contralateral control (i).

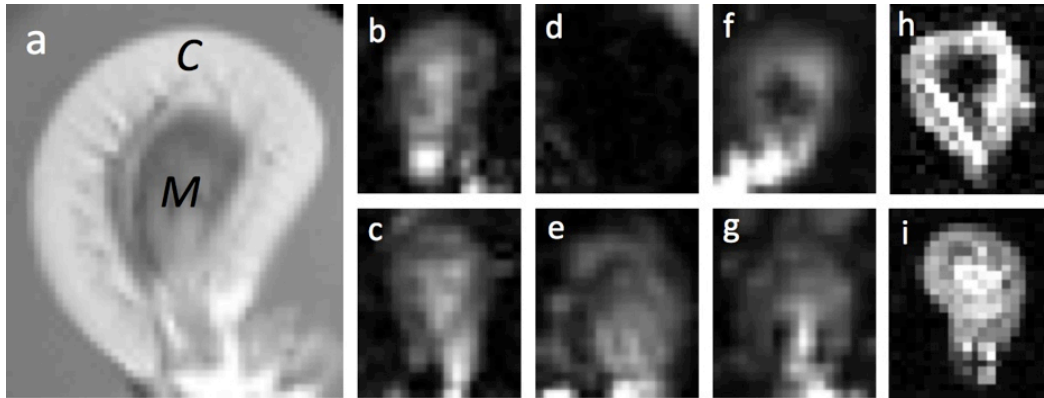


Figure 5.2 (a) ^1H TSE image of *ex vivo* rat kidney cross-section showing cortex [C] and medulla [M]. *In vivo* rat kidney cross sections showing renal perfusion via ^{19}F imaging of PFCE NP emulsion (3 ml/kg) in the following: (b, c) normal controls-L, R; (d, e) permanently occluded-L, contralateral control-R; (f, g) ischemia/reperfusion-L, contralateral control-R. (h, i) *Ex vivo* ^{19}F imaging of ischemia/reperfusion-L, contralateral control-R.

After feasibility of renal imaging with ^{19}F MRI of PFC NPs at 3T was established with proof of concept *in vivo* and *ex vivo* results, the ability to quantitate renal perfusion was tested in an additional *in vivo* experiment. Figure 5.3 displays the results of this *in vivo* warm ischemia/reperfusion rat model of AKI. A ^1H cross-sectional image of the rat (Fig. 5.3a) shows the left, injured kidney (with cortex, corticomedullary junction, and medulla delineable) and the external ^{19}F standard outlined in red. ^{19}F MR imaging with a $^{19}\text{F}/^1\text{H}$ bFFE sequence can be used to quantify circulating PFCE NPs (3 ml/kg for 5 min) (Fig. 5.3b); by comparison to the external ^{19}F PFCE standard (150 $\text{mM}_{^{19}\text{F}}$), lower renal perfusion is observed in the medulla (63.8 ± 10.9 $\text{mM}_{^{19}\text{F}}$) than in the cortex (82.8 ± 6.9 $\text{mM}_{^{19}\text{F}}$) of the injured left kidney.

Colocalization of the ^{19}F signal in the kidney and external standard are confirmed by overlaying the ^{19}F signal (green) on the ^1H signal in Figure 5.3c, which shows additional ^{19}F signal in the vasculature, spine, and likely a portion of the spleen. A B_1 map of the same imaging slice (Fig. 5.3d) demonstrates the homogeneity of the RF field produced by the $^{19}\text{F}/^1\text{H}$ dual-tuned solenoid coil, with the percent actual/requested flip angle achieved in the ^{19}F standard (95.2 ± 6.0 %) nearly the same as in the kidney (95.9 ± 3.4 %), as measured by actual flip angle imaging

(AFI). As such, B₁-mapping compensation (as presented in Chapter 4) was not needed here since it yielded the same quantitative results as the non-compensated image.

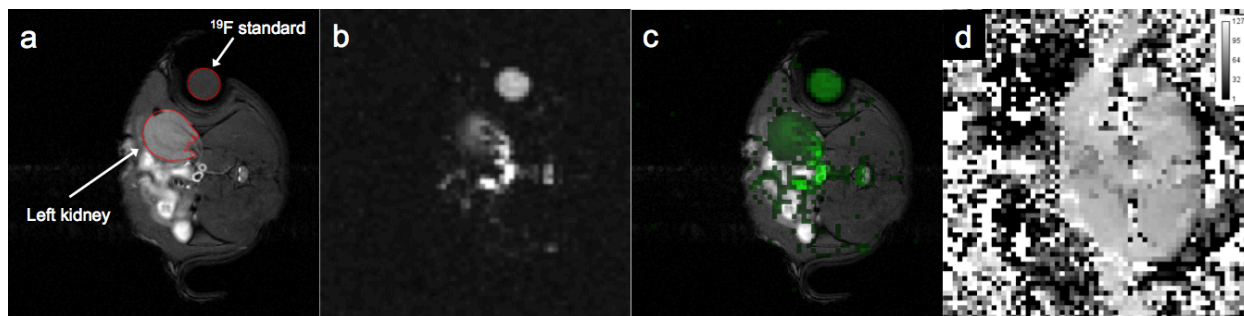


Figure 5.3 (a) Cross-sectional ¹H image of rat anatomy, showing left injured kidney in an ischemia/reperfusion model of AKI and external ¹⁹F standard outlined in red. (b) ¹⁹F MR image using simultaneous ¹⁹F/¹H bFFE sequence of PFCE NP emulsion (3 ml/kg) circulating for 5 min. Compared to external PFCE standard (150 mM_{19F}), ¹⁹F signal was quantified in the kidney, which showed lower renal perfusion in the medulla (63.8 ± 10.9 mM_{19F}) than in the cortex (82.8 ± 6.9 mM_{19F}). (c) ¹⁹F image overlaid in green on ¹H image showing colocalization of standard and renal ¹⁹F signal. (d) B₁ map using AFI (% actual/requested flip angle) demonstrating that nearly the same flip angle was achieved in the ¹⁹F standard (95.2 ± 6.0 %) as in the kidney (95.9 ± 3.4 %) with the ¹⁹F/¹H dual-tuned solenoid coil.

Although homogeneous in the plane transverse to the long axis of the coil, the RF field produced along the solenoid coil's long axis (Figure 5.4) exhibits a characteristically inhomogeneous B₁ field outside the well-defined field of view. This highlights the need for appropriate placement of the animal inside the solenoid coil, which is confirmed with a series of scout scans at the beginning of an imaging experiment.

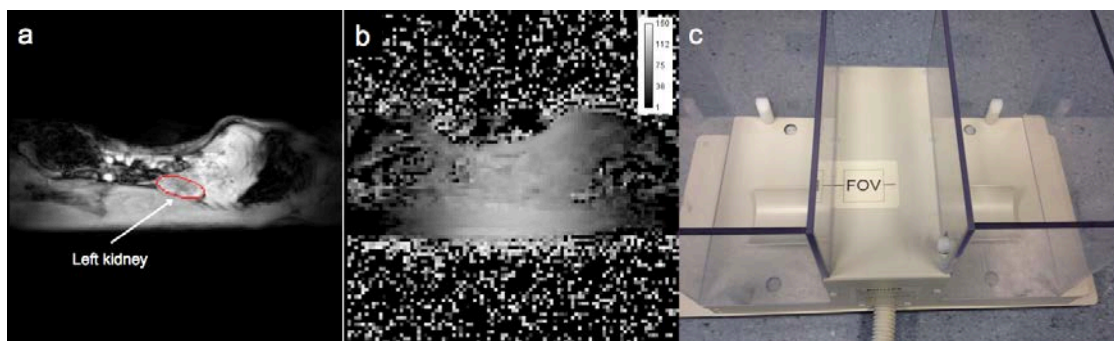


Figure 5.4 (a) Long-axis ¹H image of rat anatomy, showing left injured kidney in an ischemia/reperfusion model of AKI outlined in red. (b) B₁ map using AFI (% actual/requested flip angle) showing homogeneous RF field within field-of-view (FOV) (~ 5 cm long) of ¹⁹F/¹H dual-tuned solenoid coil (c), which falls off outside coil FOV.

5.1.4 Discussion

These data confirm that renal perfusion can be imaged at clinical field strengths with simultaneous $^{19}\text{F}/^1\text{H}$ MRI of circulating PFC NPs. ^{19}F MRI of injured kidneys qualitatively reveals reduced signal from PFC NPs in the medulla as compared with contralateral controls, denoting decreased local renal perfusion. Furthermore, qualitative *in vivo* and *ex vivo* imaging results are confirmed by quantitative ^{19}F MRI, which show reduced medullary renal perfusion by comparison to an external ^{19}F standard.

Interestingly, the B_1 field produced by this solenoid coil, when properly placed in the coil FOV, is quite homogeneous and did not necessitate B_1 -mapping compensation. Instead of invalidating the B_1 -mapping compensation technique of Chapter 4 (especially since the flip angle calibration technique was still necessary here), this suggests that small, homogeneous $^{19}\text{F}/^1\text{H}$ dual-tuned solenoid coils can be used for small animal experiments, as in this rat experiment, without the need for post-processing. However, when the imaging geometry requires a non-solenoidal coil, as in human kidney imaging applications, this technique will be valuable to ensure quantitative ^{19}F renal imaging results match those found in preclinical settings.

5.1.5 Conclusion

This study presented and validated a technique to use quantitative ^{19}F MRI to detect accumulation of circulating PFC NPs as a means to measure local renal perfusion, which was importantly shown at 3T. The ability to noninvasively image and quantify renal perfusion at clinical field strengths affords many other potentially translatable applications of kidney imaging with ^{19}F MRI in the clinic. Recent work by this group has demonstrated that direct targeting and pharmaceutical knockdown of activated thrombin at the sites of acute kidney injury with a

selective PFC NP-based thrombin inhibitor, PPACK (phenylalanine-proline-arginine-chloromethylketone), improves kidney reperfusion and protects renal function after transient warm ischemia (Chen, Vemuri, Goette, et al. *In review*). Additionally, ^{19}F MR has been shown to exploit variations in blood pool T_1 relaxation to quantify renal oxygenation, because ^{19}F T_1 is inversely proportional to the local oxygen content ($p\text{O}_2$) (7,10). Thus, ^{19}F MR with PFC NP emulsions offers a promising opportunity to image and quantify renal perfusion in AKI on clinical MR scanners.

5.2 Quantifying the Impact of Diet-Induced Atherosclerotic Plaque Erosions with ^{19}F MRI

5.2.1 Introduction

Atherosclerosis is the leading cause of death in the developed world, manifesting high morbidity and mortality as a consequence of recurrent acute vascular events that are nearly unpredictable in individuals despite maximal medical therapy (11,12). Recent focus on the pathophysiology of atherosclerosis has shifted to the wide array of inflammatory cell types and necrotic debris that engage a host of prothrombotic signaling events resulting in acute focal clotting and vascular obstruction, unstable angina, and infarction (13,14). Pathological studies on victims of acute coronary syndromes (15,16) have suggested that these acute vascular events are a consequence of plaque erosions in 33% of cases, which are not necessarily associated with plaque ruptures (17,18).

Disruption of the normally anti-thrombotic endothelial layer in an atherosclerotic vessel results in exposure of circulating blood elements to a reservoir of inflammatory cell types, lipids, cytokines, and coagulation factors that contribute to a pro-inflammatory hypercoagulable state (19). Early descriptions of the “vulnerable plaque” by Ambrose and others were expressed in

terms of a propensity to focal thrombosis rather than morphological or biochemical descriptors (20,21). Yet regardless of the definition, there are still no predictive data that delineate endothelial barrier disruption in patients with atherosclerosis and their related propensity to focal thrombosis, because no generally applicable noninvasive techniques are available for their detection prior to death and autopsy.

We recently reported the development of a long-term dietary regimen and an MR molecular imaging approach for the detection and quantification of plaques accumulating semipermeant PFC nanoparticles at 11.7 T, as a potential diagnostic surrogate for endothelial barrier disruption (22). ^{19}F MRI allowed specific localization and quantification of the concentration of PFC NPs in endothelial barrier disrupted plaques in older rabbits *ex vivo*, as well as in human carotid endarterectomy samples that were incubated *ex vivo* with the PFC NPs. Our goal here is to quantify the presence of diet-induced erosions by passive accumulation of nontargeted PFC NP emulsion in an *in vivo* atherosclerotic animal model at clinical field strength. Accordingly, we show that atherosclerotic plaque erosions are detectable by ^{19}F MRI at 3T, suggesting a clinically translatable strategy for quantitative plaque staging in terms of endothelial barrier disruption.

5.2.2 Methods

5.2.2.1 Atherosclerotic Animal Model

All procedures were performed with approval from the Washington University Animal Studies Committee. Male New Zealand White rabbits were maintained on a Western diet, consisting of 0.25% cholesterol feed (Cat. 9433, TestDiet, St. Louis, MO) for 9 months. This hyperlipidemic rabbit model has been consistently shown to generate significant atherosclerotic

plaque burden throughout arterial vessels (23). For control images without plaque development, young rabbits were fed normal chow. Both control and atherosclerotic rabbits were anesthetized and given a 1 ml/kg intravenous bolus of nontargeted PFC nanoparticles 2-3 hours prior to ^{19}F MRI.

5.2.2.2 *In Vivo* ^{19}F MR Molecular Imaging

The imaging study was performed on a 3T clinical whole-body scanner (Achieva, Philips Healthcare, The Netherlands), outfitted with a dual $^{19}\text{F}/^1\text{H}$ spectrometer system (24). A dual-resonant $^{19}\text{F}/^1\text{H}$ surface RF coil was used (15×15 cm), which can either transmit or receive at both resonance frequencies simultaneously (25). Imaging was performed 3h post-injection of 1.0 ml/kg PFC NP with perfluoro-15-crown-5-ether (PFCE; $\text{C}_{10}\text{F}_{20}\text{O}_5$) core as previously described (26). To avoid signal contamination from inhaled fluorinated anesthesia, a xylazine (10mg/kg) / ketamine (85 mg/kg) i.m. injection was used for anesthesia induction, which was maintained with a ketamine i.v. infusion (18 mg/kg/hr). A 2D simultaneous $^{19}\text{F}/^1\text{H}$ bFFE sequence was used with the following parameters: FOV = 128×128 mm, matrix = 96×96, slice thickness = 20 mm, voxel size = 1.33×1.33×20 mm, $\alpha = 25^\circ$, exBW = 5 kHz centered on single PFCE peak, pBW = 500 Hz, TR/TE = 14/1.72 ms, 1000 NSA, and a scanning time of 33 minutes.

Employing the above technique without alteration, however, would yield ^{19}F signal from both the PFC NP located in the plaque as well as the circulating blood pool. Although some protocols have been used to selectively eliminate certain ^{19}F NMR peaks, such as chemical shift selective (CHESS) saturation (27), or to generate contrast by saturation recovery as in blood flow-enhanced-saturation-recovery (BESR) (28), no protocols were found to selectively eliminate ^{19}F signal in flowing blood. Selective saturation of spins with the regional saturation

technique (REST) is typically used to eliminate ^1H signal from fat surrounding a particular region of interest, and was investigated here as a method to eliminate ^{19}F signal from the blood pool, leaving only ^{19}F signal from PFC NPs in plaque erosions. Two parallel saturation bands 30-mm in thickness both 10-mm proximal and distal to the imaging slice were applied to eliminate ^{19}F signal from the blood pool, using REST slabs at the PFCE resonance frequency, after testing to confirm REST slab effectiveness on ^{19}F nuclei.

The imaging slice was centered on the abdominal aorta, located 2-3 cm distal to the renal artery via an angiogram consisting of a multi-2D time-of-flight gradient echo sequence with the following parameters: FOV = 100×78 mm, matrix = 112×112 , slice thickness = 2 mm, $\alpha = 60^\circ$, TR/TE = 13.54/4.06 ms, 4 NSA, and a scanning time of 3 minutes. After anatomical colocalization of ^{19}F signal was confirmed with the simultaneously acquired ^1H image, a high-resolution gradient echo ^1H image was used to display the overlaid ^{19}F signal with the following parameters: FOV = 128×128 mm, matrix = 256×256 , slice thickness = 4 mm, voxel size = $0.5\times 0.5\times 4$ mm, $\alpha = 35^\circ$, TR/TE = 25.16/7.02 ms, 23 NSA, and a scanning time of 2.5 minutes.

5.2.2.3 Histology

Histological sections were created from samples of the fat-fed and control rabbit aortas, and analyzed for lipid content by light microscopy with an oil red O stain (29). Sections of rabbit aorta from hyperlipidemic and normal rabbits were frozen in O.C.T. media and cryosectioned into 8 μm slices, dried, and fixed in 10% formalin. After rinsing with 60% isopropanol, sections were stained with a freshly prepared 0.3% oil red O (Sigma-Aldrich, St. Louis, MO) working solution in isopropanol for 15 min, followed by another 60% isopropanol rinse (30). Nuclei were lightly stained with alum haematoxylin and rinsed with distilled water, and finally the sections

were mounted on slides with aqueous mountant. Microscopy was performed under 100X magnification.

5.2.3 Results

Figure 5.5 shows the proof-of-concept experiment to refine the *in vivo* ^{19}F MRI protocol in a control rabbit. Within three minutes of the 1 ml/kg nontargeted PFC NP emulsion injection (instead of the typical 2-3 hour circulation time), ^{19}F MR imaging was performed to test the coil performance and effectiveness of REST slab saturation. Figure 5.5a shows a long-axis view of the rabbit, with ^{19}F signal detectable in the aorta, liver, and kidney, confirmed with colocalization in the $^{19}\text{F}/^1\text{H}$ overlay image (Fig. 5.5c). A REST slab perpendicular to the imaging slice (Fig. 5.5e) was used to saturate the ^{19}F spins from the aorta and liver, which was successful, as seen in Figure 5.5b&d. However, since the saturation band was applied in the imaging slice, all ^{19}F signal was eliminated from that portion of the image. Figure 5.6 displays resultant cross-sectional ^{19}F images using one parallel saturation band proximal to the imaging slice in the control rabbit, which successfully eliminates only aortic ^{19}F signal from circulating PFC NPs.

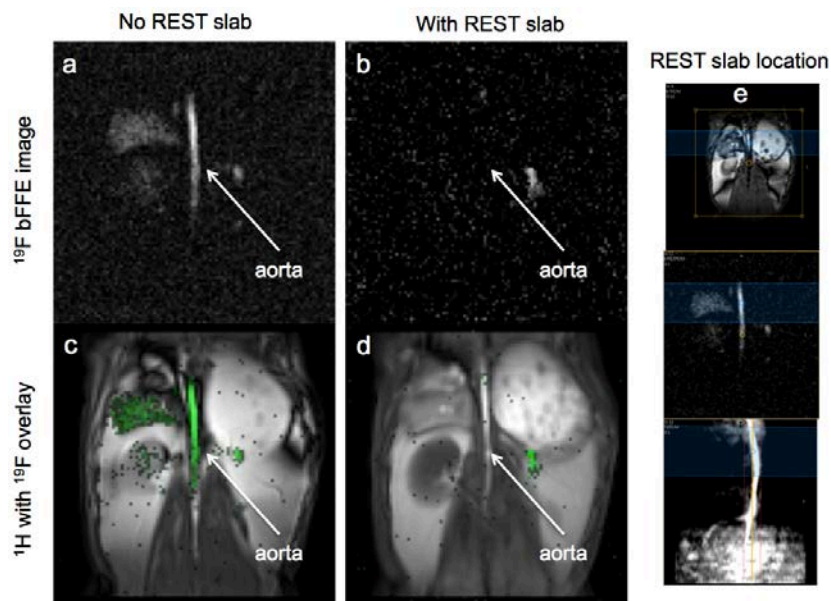


Figure 5.5 ^{19}F MRI of 1 ml/kg PFC NP emulsion injected into normal chow rabbit 3 min prior to imaging. (a) ^{19}F bFFE image without REST slab shows long-axis view of the rabbit, with ^{19}F signal detectable in aorta, liver, and kidney, confirmed with colocalization in $^{19}\text{F}/^1\text{H}$ overlay image (c). A REST slab perpendicular to the imaging slice eliminates ^{19}F signal from image (b & d). REST slab and imaging slice location (e).

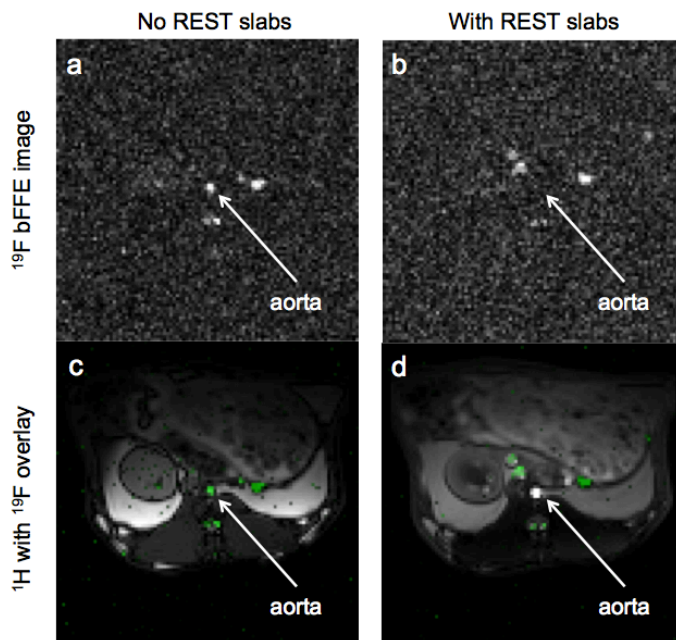


Figure 5.6 Cross-sectional ^{19}F MR images without (a) and with (b) one parallel REST slab proximal to the imaging slice, which eliminates only aortic ^{19}F signal from circulating PFC NPs, confirmed with ^{19}F overlays (green) on ^1H images (c & d).

Upon further investigation with other experimental iterations, it was determined that two 30-mm thick REST slabs 10-mm proximal and distal to a cross-sectional imaging slice would provide optimum saturation of ^{19}F signal from flowing aortic and venous blood, while allowing for sensitive ^{19}F MR detection of PFC NPs in plaque. The position of these REST slabs can be seen in Figure 5.7, which also shows an overlay of the angiogram that was used for slice positioning in the control and atherosclerotic rabbits.

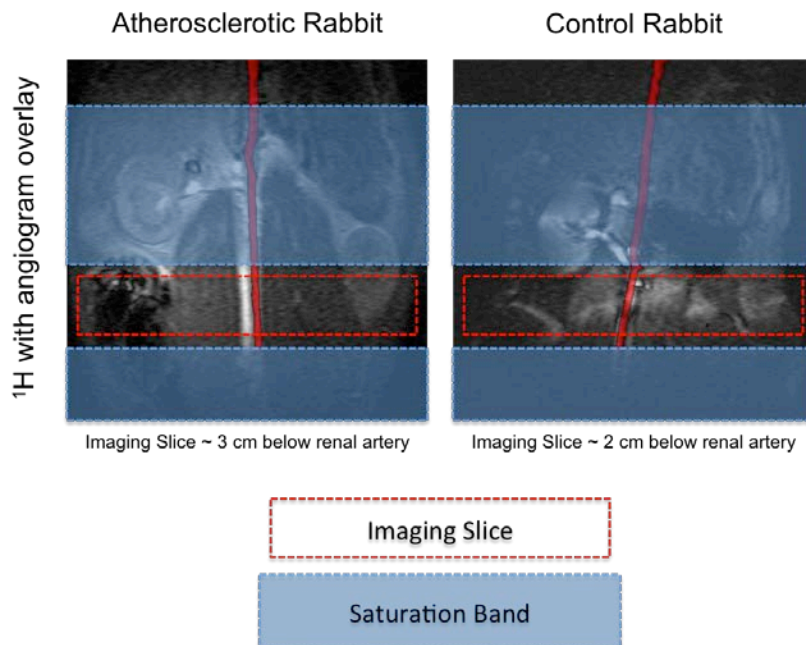


Figure 5.7 Locations of saturation bands used to eliminate ^{19}F signal from flowing blood proximal and distal to imaging slice (which continued beyond the image FOV). Aorta, shown in red, was imaged with a time-of-flight angiogram. [Figure reprinted from Palekar, Goette, et al. *In preparation*]

To demonstrate the potential for *in vivo* delineation of endothelial barrier disruption with a clinical 3T MRI scanner, ^{19}F MRI was performed on rabbits with or without diet-induced atherosclerotic plaque and erosions (Fig. 5.8). Proton images of abdominal cross-sections (Fig. 5.8a&d) show the position of the aorta in rabbits fed normal chow and Western diet, respectively. Figure 5.8e shows the ^{19}F MR signature after PFC NP circulation for 180 minutes in the hyperlipidemic rabbit. Compared to an external standard of PFCE NP in agar (150

mM_{19F}), the aortic plaque ^{19F} signal was quantified as 26.1 mM_{19F}. Note the suppression of luminal blood ^{19F} signal in normal chow rabbit (Fig. 5.8b) due to saturation band placement (Fig. 5.7), indicating that no signal arises from the circulating PFC NP in the blood pool. Figure 5.8c&f displays ^{19F}/^{1H} overlays showing the aortic and adjacent vena cava wall ^{19F} signal (green) emanating from PFC NP permeating into arterial plaques, and interestingly into inflamed venous structures under the same hyperlipidemic drive (31,32). Figure 5.8c demonstrates that in a healthy rabbit, no measurable nanoparticle retention occurs in the aorta or vena cava. Figure 5.8g&h shows representative oil red O stains of the previously imaged regions of interest showing aortic lipid-containing plaque elements in the normal chow rabbit and cholesterol fed rabbit, respectively.

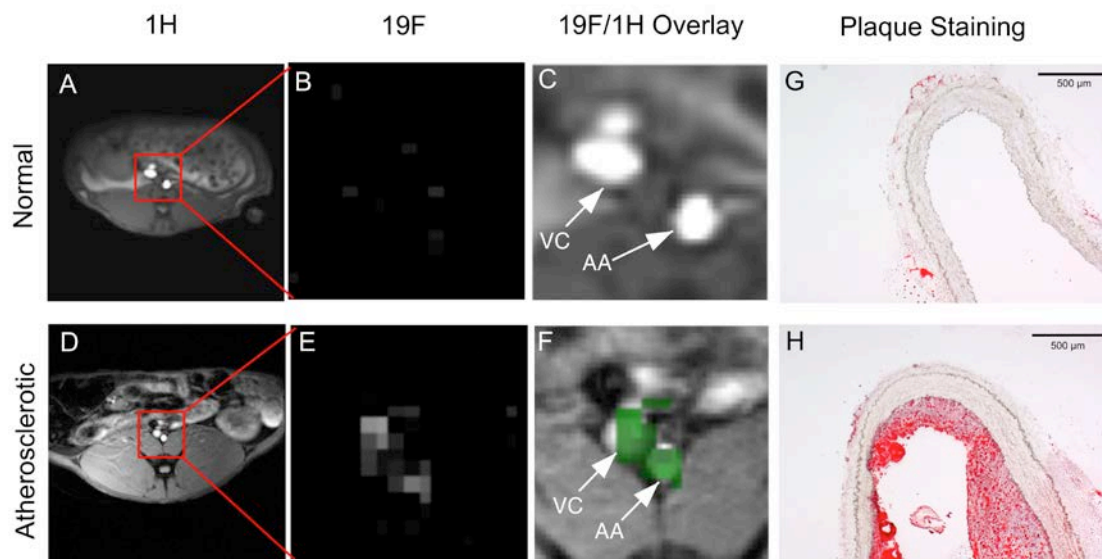


Figure 5.8 Cross-sectional ^{1H} images of (a) normal chow rabbit and (d) cholesterol fed rabbit showing location of abdominal aorta (red box). ^{19F} bFFE images of PFCE nanoparticle ^{19F} signal in the region of interest for (b) normal chow rabbit and (e) cholesterol fed rabbit. Saturation bands proximal and distal to imaging slice eliminate ^{19F} signal from blood. ^{19F} signal (green) overlaid on ^{1H} image showing ^{19F} signal colocalization for the region of interest in a (c) normal chow rabbit and (f) cholesterol fed rabbit, demonstrating deposition of PFC-NP only in inflamed abdominal aorta (AA) and vena cava (VC). Representative oil red O stains of the imaged area showing plaque elements in (g) normal chow rabbit and (h) cholesterol fed rabbit. Scale bars denote 500 μm. [Figure reprinted from Palekar, Goette, et al. *In preparation*]

5.2.4 Discussion

These data show that atherosclerotic plaque erosions infiltrated by passive accumulation of nontargeted PFC NP emulsion are detectable by ^{19}F MRI of at 3T. Two REST slabs, at a frequency matching that of the PFCE NPs, parallel to the cross-sectional imaging slice successfully eliminated ^{19}F signal from the blood pool, allowing for the direct imaging and quantification of accumulated emulsion. Quantification was performed by comparison of the isolated ^{19}F signal from the aortic plaque to an external standard of known concentration at the same distance away from the $^{19}\text{F}/^1\text{H}$ dual-tuned coil. Although the RF field was not mapped for this study, a B_1 -mapping compensation as presented in Chapter 4 would ensure accuracy and repeatability of these measurements over time and across sites.

Note that the voxel size required for recording a sufficient ^{19}F signal to enable fluorine MRI necessarily yields a comparatively low-resolution ^{19}F image in the rabbit (Fig. 5.8b&e), as contrasted with the ^1H image. However, the ability to image voxels containing PFC NP at 3T on a multispectral clinical scanner in rabbits suggests that this approach might be sufficient for human MRI where higher voxel fluorine concentrations might be achieved to enhance sensitivity due to the greater masses of tissues involved. The present results also suggest potential for adding value in the detection of individuals prone to thrombosis based on delineation of the "anatomical burden of atherosclerosis," as recently discussed by Mancini et al (33) as a predictor of vascular outcomes, with the use of non-invasive MRI quantification of biocompatible nanoparticles bearing a direct relationship to hypercoagulability.

5.2.5 Conclusion

This study demonstrated the potential to image atherosclerotic plaque erosions with accumulation of nontargeted PFC NP at clinical field strengths. Although further *in vivo* evaluation will be required to assess translational relevance of this approach, the *in vivo* 3T ¹⁹F MRI data obtained in this and other settings suggests feasibility (26,34).

5.3 Acknowledgements

For the renal imaging work (section 5.1), I would like to thank the co-authors of the following manuscript: Anti-thrombin nanoparticles improve kidney reperfusion and protect kidney function after ischemia/reperfusion injury. Chen J*, Vemuri C*, Palekar RU, Gaut JP, Goette MJ, Hu L, Zhang H, Wickline SA. *Kidney Int. In review* (*both authors contributed equally to the work). My role in the work was to assist Dr. Chandu Vemuri, a vascular surgeon in the Department of Surgery at Washington University, with the unilateral ischemia/reperfusion model in mice, as well as a bilateral ischemia/reperfusion model in rats. For this paper, the mouse kidneys were imaged at 11.7T by Dr. Junjie Chen, and the rat kidneys were not imaged, but used for immunohistochemistry. The data presented in section 5.1, with unilateral complete occlusion and ischemia/reperfusion in rats (i.e. Figures 5.1 – 5.4), were separate from the data presented in the paper. With assistance from Drs. Vemuri and Chen as well as John S. Allen for the animal handling and surgery, all data presented and discussed in this section (5.1) were acquired, processed, and written by me.

For the atherosclerosis imaging work (section 5.2), I would like to thank the co-authors of the following manuscript: Functional Delineation of Diet-Induced Atherosclerotic Plaque Endothelial Disruption and Hypercoagulable Erosions With Semi-Permeable Nanoparticles.

Palekar RU, Jallouk AP, Goette MJ, Myerson JW, Allen JS, Akk A, Chen J, Yang L, Tu Y, Miller MJ, Pham CTN, Wickline SA, Pan H. *J Am Coll Cardiol. In preparation.* My role in the work was to acquire and process the MR images for Figures 5.7 and 5.8, which were used in the manuscript. The histological images presented in Figure 5.8g&h were acquired by RU Palekar. The data presented in Figures 5.5 and 5.6 were not presented in the paper, and were acquired, processed, and discussed by me.

5.4 References

1. Waikar SS, Liu KD, Chertow GM. Diagnosis, epidemiology and outcomes of acute kidney injury. *Clin J Am Soc Nephrol* 2008;3(3):844-861.
2. Sutton TA, Fisher CJ, Molitoris BA. Microvascular endothelial injury and dysfunction during ischemic acute renal failure. *Kidney Int* 2002;62(5):1539-1549.
3. Thomsen HS, Morcos SK, Almen T, Bellin MF, Bertolotto M, Bongartz G, Clement O, Leander P, Heinz-Peer G, Reimer P, Stacul F, van der Molen A, Webb JA, Committee ECMS. Nephrogenic systemic fibrosis and gadolinium-based contrast media: updated ESUR Contrast Medium Safety Committee guidelines. *Eur Radiol* 2013;23(2):307-318.
4. Jo SK, Rosner MH, Okusa MD. Pharmacologic treatment of acute kidney injury: why drugs haven't worked and what is on the horizon. *Clin J Am Soc Nephrol* 2007;2(2):356-365.
5. Zimmer F, Zöllner FG, Hoeger S, Klotz S, Tsagogiorgas C, Krämer BK, Schad LR. Quantitative Renal Perfusion Measurements in a Rat Model of Acute Kidney Injury at 3T: Testing Inter- and Intramethodical Significance of ASL and DCE-MRI. *Plos One* 2013;8(1):e53849.

6. Wu WC, St Lawrence KS, Licht DJ, Wang DJ. Quantification issues in arterial spin labeling perfusion magnetic resonance imaging. *Top Magn Reson Imaging* 2010;21(2):65-73.
7. Hu L, Chen J, Yang X, Senpan A, Allen JS, Yanaba N, Caruthers SD, Lanza GM, Hammerman MR, Wickline SA. Assessing intrarenal nonperfusion and vascular leakage in acute kidney injury with multinuclear $^1\text{H}/^{19}\text{F}$ MRI and perfluorocarbon nanoparticles. *Magn Reson Med* 2013.
8. Caruthers SD, Winter PM, Wickline SA, Lanza GM, Keupp J. MR molecular imaging of angiogenesis using targeted perfluorocarbon nanoparticles. *MedicaMundi* 2010;54(2):5-13.
9. Hu G, Lijowski M, Zhang H, Partlow KC, Caruthers SD, Kiefer G, Gulyas G, Athey P, Scott MJ, Wickline SA, Lanza GM. Imaging of Vx-2 rabbit tumors with $\alpha\text{v}\beta 3$ - integrin-targeted ^{111}In nanoparticles. *Int J Cancer* 2007;120(9):1951-1957.
10. Mason RP, Jeffrey FM, Malloy CR, Babcock EE, Antich PP. A noninvasive assessment of myocardial oxygen tension: ^{19}F NMR spectroscopy of sequestered perfluorocarbon emulsion. *Magn Reson Med* 1992;27(2):310-317.
11. Stone GW, Maehara A, Lansky AJ, de Bruyne B, Cristea E, Mintz GS, Mehran R, McPherson J, Farhat N, Marso SP, Parise H, Templin B, White R, Zhang Z, Serruys PW, Investigators P. A prospective natural-history study of coronary atherosclerosis. *N Engl J Med* 2011;364(3):226-235.
12. Saric M, Kronzon I. Aortic atherosclerosis and embolic events. *Curr Cardiol Rep* 2012;14(3):342-349.

13. Croce K, Libby P. Intertwining of thrombosis and inflammation in atherosclerosis. *Curr Opin Hematol* 2007;14(1):55-61.
14. Demetz G, Ott I. The Interface between Inflammation and Coagulation in Cardiovascular Disease. *Int J Inflamm* 2012;2012:860301.
15. Farb A, Burke AP, Tang AL, Liang TY, Mannan P, Smialek J, Virmani R. Coronary plaque erosion without rupture into a lipid core. A frequent cause of coronary thrombosis in sudden coronary death. *Circulation* 1996;93(7):1354-1363.
16. Arbustini E, Dal Bello B, Morbini P, Burke AP, Bocciairelli M, Specchia G, Virmani R. Plaque erosion is a major substrate for coronary thrombosis in acute myocardial infarction. *Heart* 1999;82(3):269-272.
17. Ambrose JA. In search of the "vulnerable plaque": can it be localized and will focal regional therapy ever be an option for cardiac prevention? *J Am Coll Cardiol* 2008;51(16):1539-1542.
18. Sakakura K, Nakano M, Otsuka F, Ladich E, Kolodgie FD, Virmani R. Pathophysiology of atherosclerosis plaque progression. *Heart Lung Circ* 2013;22(6):399-411.
19. Mackman N. Triggers, targets and treatments for thrombosis. *Nature* 2008;451(7181):914-918.
20. Kullo IJ, Edwards WD, Schwartz RS. Vulnerable plaque: pathobiology and clinical implications. *Ann Intern Med* 1998;129(12):1050-1060.
21. Ambrose JA, Winters SL, Stern A, Eng A, Teichholz LE, Gorlin R, Fuster V. Angiographic morphology and the pathogenesis of unstable angina pectoris. *J Am Coll Cardiol* 1985;5(3):609-616.

22. Zhang H, Zhang L, Myerson J, Bibee K, Scott M, Allen J, Sicard G, Lanza G, Wickline S. Quantifying the evolution of vascular barrier disruption in advanced atherosclerosis with semipermeant nanoparticle contrast agents. *Plos One* 2011;6(10):e26385.
23. Winter P, Caruthers S, Fuhrhop R, Allen J, Williams T, Harris T, Wickline S, Lanza G. Serial Delivery and Assessment of Targeted Anti-Angiogenic Therapy against Atherosclerosis. *J Cardio Magn Reson* 2007;9(2):350.
24. Keupp J, Rahmer J, Grässlin I, Mazurkewitz PC, Schaeffter T, Lanza GM, Wickline SA, Caruthers SD. Simultaneous dual-nuclei imaging for motion corrected detection and quantification of ¹⁹F imaging agents. *Magn Reson Med* 2011;66(4):1116-1122.
25. Hockett FD, Wallace KD, Schmieder AH, Caruthers SD, Pham CTN, Wickline SA, Lanza GM. Simultaneous dual frequency ¹H and ¹⁹F open coil imaging of arthritic rabbit knee at 3T. *IEEE T Med Imaging* 2011;30(1):22-27.
26. Neubauer AM, Caruthers SD, Hockett FD, Cyrus T, Robertson JD, Allen JS, Williams TD, Fuhrhop RW, Lanza GM, Wickline SA. Fluorine cardiovascular magnetic resonance angiography in vivo at 1.5 T with perfluorocarbon nanoparticle contrast agents. *J Cardio Magn Reson* 2007;9(3):565-573.
27. Brix G, Bellemann ME, Zabel HJ, Bachert P, Lorenz WJ. Selective ¹⁹F MR imaging of 5-fluorouracil and alpha-fluoro-beta-alanine. *Magn Reson Imaging* 1993;11(8):1193-1201.
28. Hu L, Chen J, Yang X, Caruthers SD, Lanza GM, Wickline SA. Rapid quantification of oxygen tension in blood flow with a fluorine nanoparticle reporter and a novel blood flow-enhanced-saturation-recovery sequence. *Magn Reson Med* 2013;70(1):176-183.

29. Lillie RD, Ashburn LL. Supersaturated solutions of fat stains in dilute isopropanol for demonstration of acute fatty degeneration not shown by Herxheimer's technique. *Arch Pathol* 1943;36:432.
30. Ellis R. Oil Red O Staining Protocol. Volume 2014: IHC World; 2011.
31. Poredos P, Jezovnik MK. The role of inflammation in venous thromboembolism and the link between arterial and venous thrombosis. *Int Angiol* 2007;26(4):306-311.
32. Eriksson EE, Karlof E, Lundmark K, Rotzius P, Hedin U, Xie X. Powerful inflammatory properties of large vein endothelium in vivo. *Arterioscl Thromb Vas* 2005;25(4):723-728.
33. Mancini GB, Hartigan PM, Shaw LJ, Berman DS, Hayes SW, Bates ER, Maron DJ, Teo K, Sedlis SP, Chaitman BR, Weintraub WS, Spertus JA, Kostuk WJ, Dada M, Booth DC, Boden WE. Predicting outcome in the COURAGE trial (Clinical Outcomes Utilizing Revascularization and Aggressive Drug Evaluation): coronary anatomy versus ischemia. *JACC Cardiovasc Interv* 2014;7(2):195-201.
34. Winter PM, Morawski AM, Caruthers SD, Fuhrhop RW, Zhang H, Williams TA, Allen JS, Lacy EK, Robertson JD, Lanza GM, Wickline SA. Molecular imaging of angiogenesis in early-stage atherosclerosis with alpha(v)beta3-integrin-targeted nanoparticles. *Circulation* 2003;108(18):2270-2274.

Chapter 6. Imaging of Peripheral Arterial Disease in Amputated

Human Lower Extremity Specimens

As a step beyond preclinical imaging, but before a full clinical trial, human tissue specimens offer an opportunity to image in real-world applications, but without the need for extensive clinical trials. One such study was designed and approved, which involved the procurement of amputated human lower extremity specimens with peripheral arterial disease from the department of surgery. The work is presented here as a pilot project for human atherosclerosis imaging with nontargeted PFC NP at 3T, instead of in Chapter 5, because only one specimen was procured and imaged. The initial phantom and human specimen results, however, are promising and are a strong candidate for furthering the work of this thesis.

6.1 Introduction

Peripheral arterial disease (PAD) has a total disease prevalence of up to 10% in the general population and in up to 20% of the US population over the age of 70 (1). Symptoms may range from mild cramping while walking to debilitating pain at rest. Current medical and surgical therapies for patients with PAD are aimed at temporizing the disease process and providing symptom relief. Unfortunately, many patients become debilitated with intractable pain or have to undergo lower extremity amputation (2). Nanotechnology may be able to fill the significant clinical need to diagnose atherosclerotic disease earlier and to halt or reverse disease progression by imaging and potentially treating the disease with nanoparticles (3). Our laboratory has made significant progress in the creation and testing of PFC nanoparticles specific to cardiovascular disease, with extensive work with *in vitro* and *in vivo* animal models, as well as

human vascular tissue specimens (4-9). While we have characterized the behavior in sections of tissue or plaques (10), the behavior, ability to image and therapeutic potential in intact human vasculature is not known. This study entails the perfusion of nanoparticles into intact vasculature in lower extremity amputation specimens. The specific particles used will include those we have studied in the past for cardiovascular imaging and for local thrombin inhibition (5). We hypothesize that these particles will localize to areas of atherosclerotic disease, will be able to be detected by ^{19}F MRI, and therefore, may be useful in the diagnosis and targeted therapy of PAD.

6.2 Methods

A phantom was first designed and constructed to mimic blood flow and imaging properties of a human lower leg specimen by encasing tubing (~ 3 mm diameter) within 2% agar inside of a 2 L bottle (Fig. 6.2b). The tubing was connected to an anesthesia infusion pump, rigged as a continuous circuit, with a flow rate of 600 ml/hr (10 ml/min) resulting in a flow velocity of approximately 8 cm/s in the tubing. ^1H MR angiography (MRA) was performed by circulating 1% saline doped 5000:1 with Gd^{3+} , and ^{19}F MRI was performed with static PFCE NP emulsion in the tubing. This human specimen portion of the study was performed in accordance with protocols approved by the Departments of Surgery and Pathology at Washington University in St. Louis. Amputated human lower extremity specimens were obtained directly from the surgical operating room from patients who had undergone amputation for terminal peripheral vascular disease. The intact arterial vasculature of these limbs was cannulated and immediately perfused with a solution containing 1% saline, 4% sodium citrate, and 0.01% heparin, using the previously-mentioned portable pump system at 600 ml/hr.

MR data were acquired on a 3T clinical whole-body scanner (Achieva, Philips Healthcare, Best, The Netherlands) with a dual $^{19}\text{F}/^1\text{H}$ spectrometer system and a dual-tuned transmit/receive semi-cylindrical RF coil (7×12 cm) (Fig. 6.2a). MRA was first performed on the flowing saline solution, using a multiple-2D time-of-flight (M2D TOF) sequence with a REST slab to eliminate return flow distal to the imaging slice, using the following parameters: 120 mm FOV, matrix 112^3 , 69 2-mm slices, $\alpha = 60^\circ$, TR/TE = 12.83/3.94 ms, NSA = 11, 3.3 min scan time. Maximum-intensity-projections (MIP) were reconstructed by the scanner software from the stack of MRA images in all three orthogonal imaging planes. A similar sequence was tested on the phantom with and without REST slabs.

PFC NP emulsion with a perfluoro-15-crown-5-ether core and a PPACK antithrombotic agent was circulated at 2 ml/kg for 2 hours during ^{19}F imaging. A simultaneous $^{19}\text{F}/^1\text{H}$ 3D balanced UTE-SSFP imaging sequence with Wong-type (11) 3D radial readout trajectory (as presented in Chapter 3) was used with 140 mm FOV, matrix 64^3 , isotropic voxel $\Delta x = 2.3$ mm, exBW = 4 kHz centered on PFCE peak, pBW = 400 Hz, $\alpha = 30^\circ$, TR/TE = 2.32/0.13 ms, Nyquist radius = 0.23, NSA = 56, 35 min scan time. For the phantom experiment, a simultaneous $^{19}\text{F}/^1\text{H}$ 2D bFFE sequence was also used with 140 mm FOV, matrix 128×128 , 3 mm slice thickness, exBW = 4 kHz centered on the single PFCE peak, pBW = 500 Hz, $\alpha = 25^\circ$, TR/TE = 4.198/2.10 ms, NSA = 500, 5 min scan time. The B_1 field was mapped using an actual flip-angle imaging (AFI) sequence with: 140 mm FOV, 96^2 matrix, 15 4-mm slices, $1.4 \times 1.4 \times 0.6$ mm resolution, $\alpha = 70^\circ$, 2.8 min scan time.

6.3 Initial Results

Figure 6.1a shows T₁-weighted ¹H FFE coronal images of leg phantom. MR angiography (MRA) of phantom was performed with flowing (~ 8 cm/s) saline doped 5000:1 with Gd³⁺ using M2D TOF (multiple 2D, time-of-flight) ¹H imaging with REST slab position (Fig. 6.1b). A MRA maximum intensity projection (MIP) and MIP overlay onto the ¹H image without (Fig. 6.1c&d) and with a REST slab (Fig. 6.1e&f) demonstrate the ability to saturate the spins in the return flow.

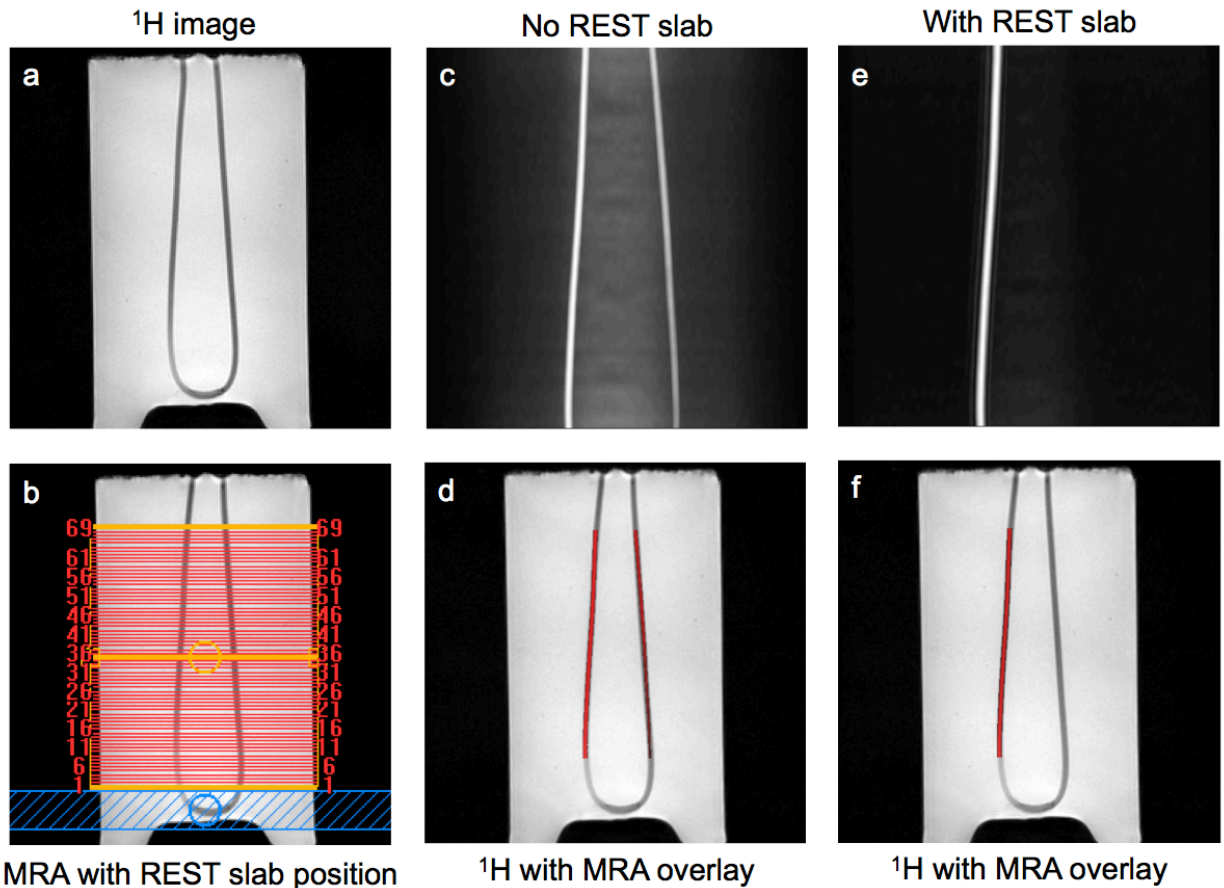


Figure 6.1 (a) T₁-weighted ¹H FFE coronal image of leg phantom. Setup of MR angiography of phantom with flowing (~ 8 cm/s) saline doped 5000:1 with Gd³⁺ using M2D TOF (multiple 2D, time-of-flight) ¹H imaging with REST slab position (b). MRA maximum intensity projection (MIP) and MIP overlay on ¹H image without (c&d) and with a REST slab (e&f) saturating the spins in the return flow.

Figure 6.2a displays the semi-cylindrical $^{19}\text{F}/^1\text{H}$ dual-tuned coil, as well as the leg phantom, consisting of tubing encased within 2% agar in 2 L bottle (Fig. 6.2b). Actual flip angle imaging (% actual/requested flip angle) maps in the transverse (Fig. 6.2c) and sagittal (Fig. 6.2e) views with corresponding profile plots (Fig. 6.2d&f) demonstrate signal drop-off with increasing in distance away from the coil (illustrated in red).

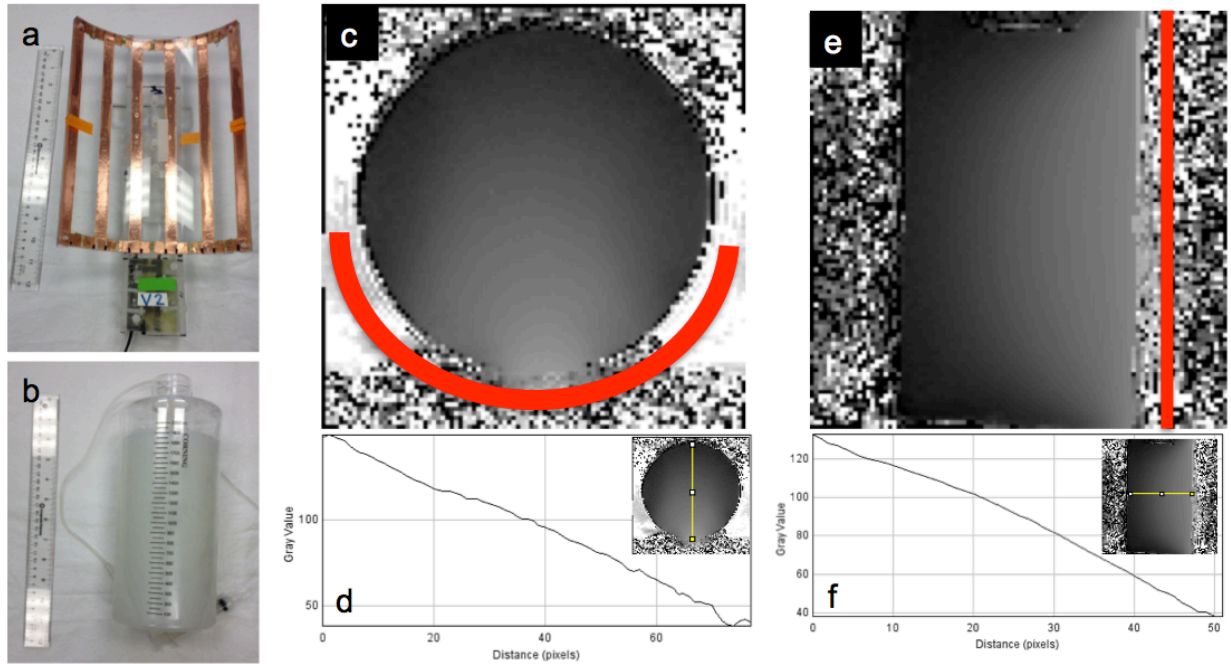


Figure 6.2 (a) Semi-cylindrical $^{19}\text{F}/^1\text{H}$ dual-tuned coil. (b) Leg phantom, consisting of tubing encased within 2% agar in 2 L bottle. Actual flip angle imaging (% actual/requested flip angle) maps in the transverse (c) and sagittal (e) views with corresponding profile plots (d & f) increasing in distance away from the coil (location illustrated in red).

Figure 6.3 exhibits T_1 -weighted ^1H FFE transverse (Fig. 6.3a) and coronal (Fig. 6.3b) images of the leg phantom. Simultaneous $^{19}\text{F}/^1\text{H}$ imaging of PFCE NP emulsion in leg phantom tubing is performed using a bFFE sequence in transverse (Fig. 6.3c) and coronal (Fig. 6.3d) planes. Note the banding artifacts from the coil and imaging protocol that are present in the coronal slice. Figure 6.3e show a ^{19}F image using balanced UTE-SSFP sequence in the transverse plane, along with a coronal MIP (Fig. 6.3f).

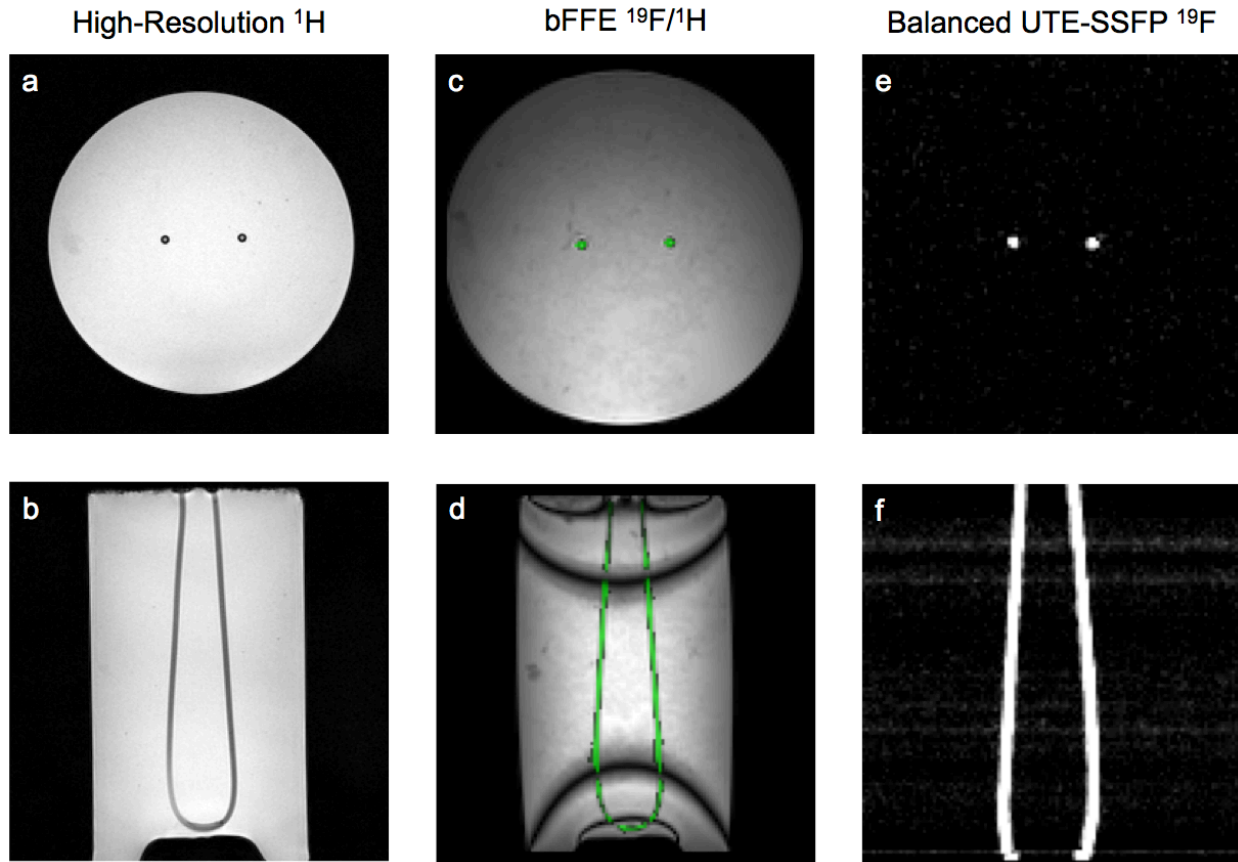


Figure 6.3 T_1 -weighted ^1H FFE transverse (a) and coronal (b) images of leg phantom. Simultaneous $^{19}\text{F}/^1\text{H}$ imaging of PFCE NP emulsion in leg phantom tubing (static) using bFFE sequence in transverse (c) and coronal (d) planes. Note: banding artifacts from coil are present in coronal slice. ^{19}F image using balanced UTE-SSFP sequence in transverse plane (e), with coronal MIP (f).

Imaging of the human lower leg specimen is displayed in Figure 6.4, demonstrating MR angiography of the leg with flowing (600 ml/hr) saline using M2D TOF (multiple 2D, time-of-flight) ^1H imaging. Maximum intensity projections (MIP) in coronal (Fig. 6.4a), sagittal (Fig. 6.4b), and transverse (Fig. 6.4c) planes are displayed. The MRA setup and slice orientation can be seen in Figure 6.4d.

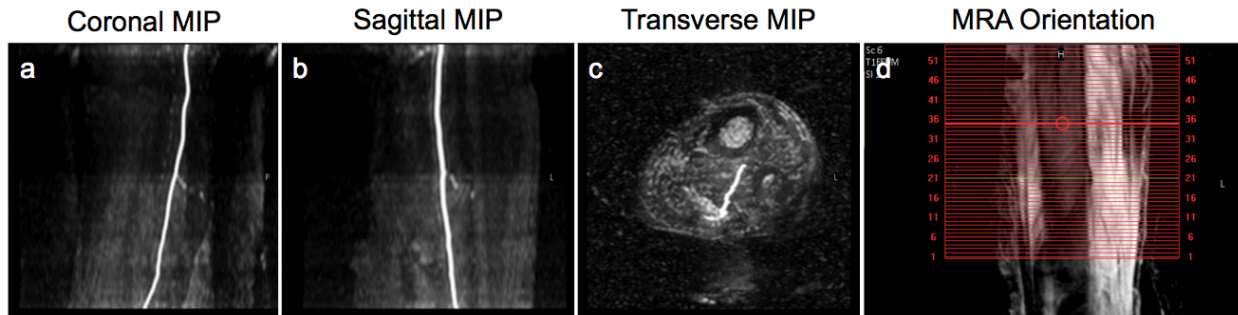


Figure 6.4 MR angiography of leg with flowing (600 ml/hr) saline using M2D TOF (multiple 2D, time-of-flight) ^1H imaging. Maximum intensity projections (MIP) in coronal (a), sagittal (b), and transverse (c) planes. MRA setup and slice orientation (d).

Figure 6.5a shows a high-resolution T_1 -weighted ^1H FFE transverse image of the leg anatomy (arrow: cannulated artery). Figure 6.5b demonstrates ^{19}F imaging of PFCE NP emulsion (~ 2 ml/kg) in the cannulated artery using a balanced UTE-SSFP sequence in the transverse plane.

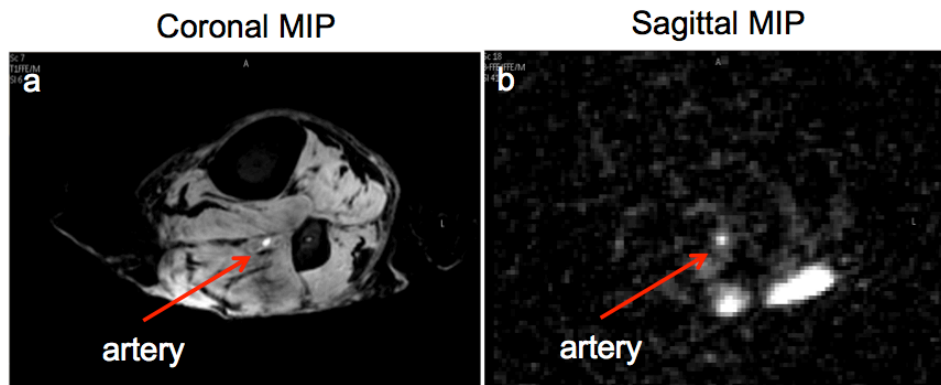


Figure 6.5 (a) High-resolution T_1 -weighted ^1H FFE transverse image of leg anatomy (arrow: cannulated artery). (b) ^{19}F imaging of PFCE NP emulsion (~ 2 ml/kg) in artery using balanced UTE-SSFP sequence in transverse plane. Other ^{19}F signal from PFC NP emulsion that pooled outside the specimen due to leaking from an absence of a return circuit.

6.4 Discussion

This proof-of-concept pilot study shows how a molecular imaging experiment goes from conception to phantom imaging to ultimate application in human tissue. Although more work is

required to optimize the protocol (i.e. a return circuit to circulate PFC NPs) and more specimens will be required to reach significance, this study offers a promising direction for future research.

6.5 Acknowledgements

I would like to thank Dr. Chandu Vemuri, a vascular surgeon in the Department of Medicine, who was vital to the approval of this protocol. My role in the work was to design the phantom experiment and perfusion setup, assist Dr. Vemuri in the operating room on the day of procurement, and perform all imaging and analysis.

6.6 References

1. Norgren L, Hiatt WR, Dormandy JA, Nehler MR, Harris KA, Fowkes FG, Group TIW. Inter-society consensus for the management of peripheral arterial disease (TASC II). *J Vasc Surg* 2007;45 Suppl S:S5-67.
2. Rooke TW, Hirsch AT, Misra S, Sidawy AN, Beckman JA, Findeiss LK, Golzarian J, Gornik HL, Halperin JL, Jaff MR, Moneta GL, Olin JW, Stanley JC, White CJ, White JV, Zierler RE. 2011 ACCF/AHA focused update of the guideline for the management of patients with peripheral artery disease (updating the 2005 guideline): a report of the American College of Cardiology Foundation/American Heart Association Task Force on Practice Guidelines. *J Am Coll Cardiol* 2011;58(19):2020-2045.
3. Wickline SA, Neubauer AM, Winter P, Caruthers S, Lanza G. Applications of nanotechnology to atherosclerosis, thrombosis, and vascular biology. *Arterioscl Thromb Vas* 2006;26(3):435-441.

4. Pan H, Myerson JW, Hu L, Marsh JN, Hou K, Scott MJ, Allen JS, Hu G, San Roman S, Lanza GM, Schreiber RD, Schlesinger PH, Wickline SA. Programmable nanoparticle functionalization for in vivo targeting. *FASEB J* 2013;27(1):255-264.
5. Myerson J, He L, Lanza G, Tollefsen D, Wickline SA. Thrombin-inhibiting perfluorocarbon nanoparticles provide a novel strategy for the treatment and magnetic resonance imaging of acute thrombosis. *J Thromb Haemost* 2011;9(7):1292-1300.
6. Morawski AM, Winter PM, Yu X, Fuhrhop RW, Scott MJ, Hockett F, Robertson JD, Gaffney PJ, Lanza GM, Wickline SA. Quantitative "magnetic resonance immunohistochemistry" with ligand-targeted ¹⁹F nanoparticles. *Magn Reson Med* 2004;52(6):1255-1262.
7. Kaneda MM, Caruthers S, Lanza GM, Wickline SA. Perfluorocarbon nanoemulsions for quantitative molecular imaging and targeted therapeutics. *Ann Biomed Eng* 2009;37(10):1922-1933.
8. Hu G, Lijowski M, Zhang H, Partlow KC, Caruthers SD, Kiefer G, Gulyas G, Athey P, Scott MJ, Wickline SA, Lanza GM. Imaging of Vx-2 rabbit tumors with $\alpha\beta 3$ - integrin-targeted ¹¹¹In nanoparticles. *Int J Cancer* 2007;120(9):1951-1957.
9. Winter PM, Morawski AM, Caruthers SD, Fuhrhop RW, Zhang H, Williams TA, Allen JS, Lacy EK, Robertson JD, Lanza GM, Wickline SA. Molecular imaging of angiogenesis in early-stage atherosclerosis with $\alpha\beta 3$ -integrin-targeted nanoparticles. *Circulation* 2003;108(18):2270-2274.
10. Flacke S, Fischer S, Scott MJ, Fuhrhop RJ, Allen JS, McLean M, Winter P, Sicard GA, Gaffney PJ, Wickline SA, Lanza GM. Novel MRI contrast agent for molecular imaging

of fibrin implications for detecting vulnerable plaques. *Circulation* 2001;104(11):1280-1285.

11. Wong STS, Roos MS. A strategy for sampling on a sphere applied to 3D selective RF pulse design. *Magn Reson Med* 1994;32(6):778-784.

Chapter 7. Conclusion

The objective of this thesis was to advance the state of the art for ^{19}F MR molecular imaging of perfluorocarbon nanoparticle emulsion contrast agents. It is the assertion of this dissertation that this objective was achieved in the following ways: (1) new tools and techniques for ^{19}F MR molecular imaging of PFC nanoparticles were created, (2) translatable procedures for absolute quantification of ^{19}F nuclei with MR molecular imaging were developed, (3) the potential for clinical translation with *ex vivo* and *in vivo* preclinical experiments was evaluated.

7.1 Summary of Major Findings

In Chapter 2, the underlying principles behind ^{19}F NMR physics and image acquisition were explored, as well as the unique properties of $^{19}\text{F}/^1\text{H}$ dual-tuned RF coils. The NMR physics governing all magnetically susceptible nuclear spins was reviewed, and distinctions were drawn between ^1H atoms and ^{19}F nuclei. Then, resultant magnetic resonance properties of ^{19}F spins, such as J-coupling, were examined, along with their effect on perfluorocarbon molecules like PFOB. The theory behind image acquisition with $^{19}\text{F}/^1\text{H}$ dual-tuned RF coils was then considered, which included a coupled resonator model with appropriate impedance matching. A new dual-tuned single-turn-solenoid RF coil was designed and constructed to open up new applications for simultaneous $^{19}\text{F}/^1\text{H}$ imaging. Experimental results with this new coil were then presented, including bench tests of electromagnetic performance, as well as phantom and *in vivo* imaging experiments.

Chapter 3 introduced a new pulse sequence, termed “balanced UTE-SSFP”, for highly sensitive ^{19}F MR imaging of agents with complex spectra. The NMR properties of molecules

with non-proton nuclei such as PFOB were discussed to understand their broad chemical shifts and complex relaxation characteristics. Then, the CF_2 spectral peak signatures of PFOB were modeled, which quickly dephases and decays due to T_2 relaxation, but can be utilized if acquired quickly. A new 3D $^{19}\text{F}/^1\text{H}$ pulse sequence was then designed and implemented to capture these CF_2 resonances, which consists of $^{19}\text{F}/^1\text{H}$ RF excitation using FID acquisition at an ultra-short echo time (UTE) and a balanced steady-state free precession (SSFP) gradient scheme with a Wong-type 3D radial readout trajectory. The sensitivity of this new balanced UTE-SSFP pulse sequence was compared to existing sequences, and shown to have a sensitivity twofold better than other sequences. Finally, *in vivo* imaging of angiogenesis-targeted PFOB nanoparticles was demonstrated in a rabbit model of cancer on a clinical 3T scanner, to validate the translational potential for the new pulse sequence.

In Chapter 4, a new approach to overcome challenges for accurate *in vivo* quantitative ^{19}F MR molecular imaging was presented, which includes flip angle calibration between the relevant ^1H and ^{19}F nuclei of interest, as well as B_1 -mapping compensation to offset expected RF inhomogeneities. A disparity in the required power settings of $^{19}\text{F}/^1\text{H}$ dual-tuned RF coils to achieve optimum flip angles for the ^{19}F and ^1H nuclei was reported and investigated. Then, an approach to remediate this difference in requisite power settings was proposed and tested, which involves a coil-specific, but spatially independent calibration ratio for each coil. This strategy permitted determination of the optimum power setting for the ^{19}F nuclei by utilizing the abundant ^1H signal as a reference. A solution to inhomogeneous RF fields was proposed that entailed mapping the B_1 field and performing an image-based correction using a signal model of the acquisition technique, which was tested in phantom and *in vivo* experiments in a rabbit model of cancer.

Chapter 5 examined two *in vivo* applications of ^{19}F MR molecular imaging at 3T. First, a new technique to image renal perfusion in acute kidney injury (AKI) at clinically relevant field strengths was presented. A model of AKI was implemented in rats by ligation and occlusion of the left renal artery, followed by reperfusion. Renal perfusion was then imaged at 3T with a $^{19}\text{F}/^1\text{H}$ dual-tuned coil after administration of PFC NPs via the tail vein. These *in vivo* results were confirmed with *ex vivo* imaging of excised kidneys. Next, the impact of diet-induced atherosclerotic plaque erosions was investigated with quantitative ^{19}F MRI of a hyperlipidemic rabbit model *in vivo*. A method was introduced and tested to visualize nontargeted PFC nanoparticles that accumulate passively in the intimal plaque regions of the rabbit aorta as a consequence of endothelial erosions and vascular barrier disruption with the use of ^{19}F MR molecular imaging combined with saturation bands to eliminate signal from the flowing blood pool, which allowed ^{19}F imaging of the vessel wall itself.

Chapter 6 investigated the potential use of ^{19}F MR molecular imaging at 3T in the clinic with a pilot study of atherosclerosis imaging using nontargeted PFC NP in human tissue specimens. Initial imaging results in a phantom and an amputated human lower limb were presented, which show promise for the use of ^{19}F imaging in human atherosclerosis imaging in the future.

7.2 Future Work

7.2.1 $^{19}\text{F}/^1\text{H}$ Dual-Tuned RF Coils

As new applications of ^{19}F MR molecular imaging of PFC NP emulsions arise, there are new opportunities to design and build specialized $^{19}\text{F}/^1\text{H}$ dual-tuned coils. One such opportunity arose during the renal imaging study (section 5.1), when a coil specific to the rat kidney anatomy

could have provided more ^{19}F sensitivity and better image quality. This coil was designed and simulated in SPICE (Figure 7.1), and consisted of a unique transmit/receive switch that would allow for simultaneous $^{19}\text{F}/^1\text{H}$ imaging with whole-(rat)-body transmission using an outer coil element and focused receiving using an inner coil element. However, this design was not built, so this could be a future direction stemming from this work.

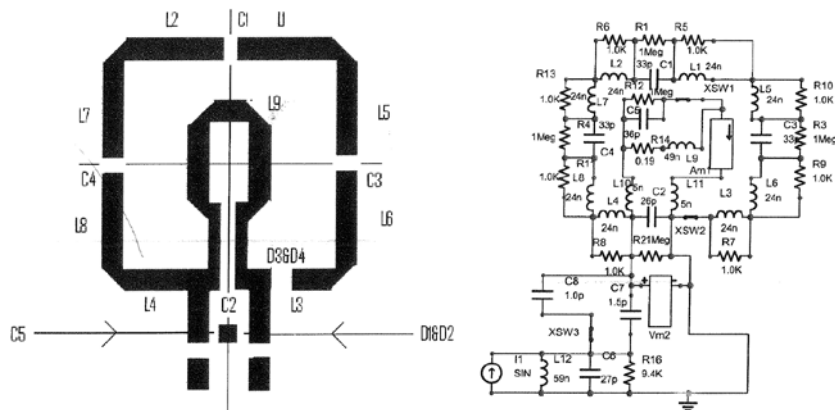


Figure 7.1 Unique $^{19}\text{F}/^1\text{H}$ dual-tuned coil design (**left**) and circuit diagram (**right**) with active switching, allowing for transmission using an outer coil element and reception using an inner coil element.

In addition to this design with different physics transmit/receive elements, the ability to perform the flip angle calibration and B_1 -mapping compensation presented in Chapter 4 could be evaluated with this type of coil, as well as other single-tuned coils. It was hypothesized that the flip angle calibration would require dual-tuned coils with the same physical element, and that the B_1 -mapping compensation could potentially work with single-tuned coils with the same physical coil elements. This hypothesis would be an interesting direction for future work.

7.2.2 Human *In Vivo* Applications

The ultimate goal of this work, in addition to the aspiration of most all molecular imaging scientists, is to translate the imaging techniques tested in phantom and preclinical experiments

into the clinic. The potential applications of this work are numerous, and include cancer and atherosclerosis imaging with $\alpha_v\beta_3$ -integrin targeted or nontargeted PFC NP emulsions (1). In addition, the renal imaging work offers a promising opportunity to image human kidneys in patients who have acute kidney disease, especially since no potentially harmful Gd-containing agents are necessary. Of course, however, all human applications require years of development and thorough testing of agents and protocols before they can be implemented in clinical trials.

7.3 References

1. Zhang H, Zhang L, Myerson J, Bibee K, Scott M, Allen J, Sicard G, Lanza G, Wickline S. Quantifying the evolution of vascular barrier disruption in advanced atherosclerosis with semipermeant nanoparticle contrast agents. *Plos One* 2011;6(10):e26385.